Modelling the long-term morphological evolution of tidal embayments

A thesis submitted in fulfilment

of the requirements for the degree of

Doctor of Philosophy

in

Earth Sciences

at

The University of Waikato

by

Barend van Maanen

THE UNIVERSITY OF
WAIKATO
Te Whare Wānanga o Waikato

2011

Abstract

A numerical model was developed to improve the understanding of the long-term morphological evolution of tidal embayments. Morphological change was simulated as a result of the interactions between hydrodynamics, sediment transport, and the evolving topography. Numerical simulations indicate that these morphodynamic interactions can lead to the initiation of tidal channels and potentially give rise to large scale channel pattern development.

The tidal range and the depth of the initially unchannelized tidal basin determined the time scale over which the channel network developed. Channels and intertidal areas rapidly formed when the basin was shallow and the tidal range large. For a large tidal range and a deep tidal basin, the tidal flow imported large volumes of sediment. The large water depths inhibited the formation of channels and the imported sediment formed a flood-tidal delta. The flood-tidal delta grew and became shallower over time until it became incised by channels. Ultimately, a complete channel network developed. Changes in the morphology of a deep basin were slowed down when the tidal range was small and the channel network then remained underdeveloped over long time scales. All the simulated morphologies, with different combinations of the tidal range and depth of the basin, evolved toward a state of less morphodynamic activity and obtained a hypsometry which resembles those of natural systems.

Basins with well-developed channel networks were used to explore the response of tidal embayments to sea level rise. During sea level rise, the intertidal geometry adjusted to the changing environmental forcing conditions. Tidal channels became larger and more widely-spaced and expanded landward because of headward erosion. This landward shift of the channel network can be accompanied by a change in the asymmetry between the flood and ebb tidal currents. Sea level rise can even lead to a transition from exporting to importing sediment. These findings indicate that morphodynamic interactions need to be included in the study of sea level rise impacts on tidal systems.

The morphodynamic model was extended to account for the interactions between mangroves and physical processes. Mangroves affected hydrodynamics and sediment dynamics in a variety of ways. In turn, hydrodynamic conditions controlled the colonization, growth, and dying of mangroves. Mangroves influenced channel network evolution by enhancing the branching of channels because the extra flow resistance in mangrove forests drove flow concentration and thus sediment erosion in between vegetated areas. On the other hand, mangroves hindered the landward expansion of channels. When the sea level was rising, mangroves increased the ability of areas to maintain an elevation above mid tide. Channel network expansion, induced by the rise in sea level, occurred differently when mangroves were present because they hindered both the branching and headward erosion of the expanding channels.

Acknowledgements

At the beginning of 2007, I travelled to New Zealand for a six month traineeship as part of my MSc study at Utrecht University, the Netherlands. At that time I never expected that I would end up spending a few years at the other side of the world to undertake PhD research. It has been a great adventure and it is my pleasure to acknowledge those who have been involved in the production of this thesis.

First and foremost I am grateful to my supervisors, Dr Giovanni Coco and Dr Karin Bryan, for guiding me with so much enthusiasm. I am indebted to them for providing sound advice and lots of good ideas throughout the entire period. Karin and Giovanni, it has been an absolute pleasure to work with you.

I thank all the members of the "Coastal and Estuarine Processes Group" at NIWA for creating such a pleasant atmosphere that made the work very enjoyable. Thanks also to my friends, both at NIWA and the University, for all the fun moments that we shared together.

I acknowledge the (New Zealand) Foundation for Research, Science and Technology and NIWA for funding this work. In particular, I thank Dr Bryce Cooper for supporting this research. Furthermore, I am thankful to the IT support team who helped me out in my continuous search for more computer power.

Thanks to the Centre for Water Research (University of Western Australia) for providing the hydrodynamic solver used throughout this research. The National Center for Earth-surface Dynamics is acknowledged for providing the software to extract channels networks from the simulated morphologies.

Last, but by no means least, I am grateful to my family and friends back home for the ongoing support, even from far away. It has been greatly appreciated. I especially thank my parents, Coby and Piet, and my brother Erik for supporting me. Unfortunately, my father could not witness the final result of my research. I remember him with love.

Barend van Maanen

Table of Contents

List of Figures vii

1. Introduction 1
   1.1 Research objective and relevance 1
   1.2 Approach and research questions 3
   1.3 Thesis outline 4

2. A numerical model to simulate the formation and subsequent evolution of tidal channel networks 6
   2.1 Introduction 6
   2.2 Model description and set-up 10
      2.2.1 Model description 10
      2.2.2 Model set-up 12
   2.3 Results 14
   2.4 Conclusions 22

3. Modelling the effects of tidal range and initial bathymetry on the morphological evolution of tidal embayments 23
   3.1 Introduction 23
   3.2 Numerical modelling 25
      3.2.1 Model description 25
      3.2.2 Model set-up 26
   3.3 Results 28
   3.4 Discussion and conclusions 36

4. It is not a bathtub: the response of tidal embayments to sea level rise 38
   4.1 Introduction 38
   4.2 Methods 39
   4.3 Results 42
   4.4 Discussion and conclusions 49

5. Modelling the effects of mangroves on the evolution of channel networks in tidal embayments 51
   5.1 Introduction 51

5.2 Methodology 53
5.2.1 Model set-up 54
5.2.2 Morphodynamic model 54
5.2.3 Mangrove colonization, growth, and mortality 55
5.2.4 Implementing the effects of mangroves on physical processes 59
5.2.5 Extracting the channel network 62
5.3 Results 63
5.3.1 Morphological evolution in the absence and presence of mangroves 63
5.3.2 Clarifying the role of each effect in changing channel density 70
5.3.3 Morphological evolution under a rising sea-level 74
5.4 Discussion 76
5.5 Conclusions 79

6. Conclusions and directions for future research 80
6.1 Conclusions 80
6.2 Directions for future research 82

References 84

Appendix A. The use of artificial neural networks to analyze and predict alongshore sediment transport 95
A.1 Introduction 96
A.2 Methods 98
A.2.1 Field Measurements 98
A.2.2 Artificial Neural Network Background and Architecture 99
A.2.3 Opening and Lightening the “black box” 103
A.3 Results 104
A.4 Discussion and Conclusions 110
Acknowledgements 112
References 112

List of Figures

1.1. Schematized diagram of the (a) morphodynamic and (b) biomorphodynamic feedback cycle. Biology affects morphology via feedbacks between biology and hydrodynamics and/or sediment dynamics. 3

2.1. (a) Plan view of the initial morphology used throughout this study. The morphology consists of an offshore area, inlet, and tidal basin. Grey areas represent land regions which form impermeable and non-erodible barriers. (b) Cross section of the initial morphology. Location of the cross section is indicated by the black line in (a). 13

2.2. Simulation of tidal channel network formation. Morphologies after (a) 5, (b) 30, (c) 80, and (d) 250 years. 14

2.3. Root-mean-square of the bed level changes between successive years computed over all grid cells in the basin as a function of time. 15

2.4. Flow field during rising tide over (a) the initial morphology and over (b) the simulated morphology after 250 years. Arrows on both panels indicate magnitude and direction of the flow. Scale of the arrows is indicated in the left-bottom corner. Velocity vectors are shown every fifth grid cell. 17

2.5. Time series of tidal elevation (black) and velocity perpendicular to the coastline (red) for (a) the initial morphology and (b) the simulated morphology after 250 years. Time series represent two tidal cycles and are obtained for a grid cell located in the tidal basin about 2.5 km in front of the centre of the inlet. 18

2.6. Simulated morphology after 5 years (allows for a comparison with Fig. 2.2a) when the time-step of the hydrodynamic model is set to 4 minutes. 19

2.7. Simulated morphologies after 80 years (allows for a comparison with Fig. 2.2c) when the hydrodynamic conditions are assumed to remain constant until bed level changes exceed (a) 5% or (b) 15% of the local water depth at high tide. 20

2.8. (a) Initial bathymetry onto which one bump is added and (b) its corresponding morphology after 30 years (allows for a comparison with Fig. 2.2b). (c) Initial bathymetry onto which two bumps are added and (d) its corresponding morphology after 30 years. 21
3.1. Aerial view of a (a) well developed (Bassin d'Arcachon, France) and (b) underdeveloped (Shinnecock Inlet, USA) tidal channel network. 24
3.2. Plan view of the initial morphologies used throughout this study. The initial depth of the tidal basin amounted to (a) 2, (b) 4, and (c) 6 m. Grey areas represent land regions which form impermeable and non-erodible barriers. (d) Cross sections of the initial morphologies. Locations of the cross sections are indicated by the black lines in (a), (b), and (c). 27
3.3. Simulated morphologies after 1000 years for different combinations of the basin's initial depth and tidal range. 29
3.4. Tidally-averaged residual flow patterns over the initial morphologies for the area around the inlet when (a) the tidal range (TR) is 2 m and the basin's initial depth (ID) is 2 m, (c) TR=2 m and ID=6 m, (e) TR=3 m and ID=6 m, and (g) TR=1 m and ID=6 m. Subplots (b), (d), (f), and (h) show the corresponding flow patterns over the simulated morphologies after 1000 years. 30
3.5. Tidally-averaged residual sediment transport patterns over the initial morphologies for the area around the inlet when (a) the tidal range (TR) is 2 m and the basin's initial depth (ID) is 2 m, (c) TR=2 m and ID=6 m, (e) TR=3 m and ID=6 m, and (g) TR=1 m and ID=6 m. Subplots (b), (d), (f), and (h) show the corresponding sediment transport patterns over the simulated morphologies after 1000 years. 31
3.6. Simulation of morphological evolution for a tidal range of 2 m and an initial depth of the basin of 2 m. Morphologies after (a) 5, (b) 30, (c) 80, and (d) 250 years. 32
3.7. Changes in sediment volume within the basin. Import (positive numbers) of sediment to and export from (negative numbers) the tidal basin vary for different combinations of the basin's initial depth and tidal range. 33
3.8. Hypsometric curves for some of the simulated morphologies. 34
3.9. Simulation of morphological evolution for a tidal range of 2 m and an initial depth of the basin of 6 m. Morphologies after (a) 60, (b) 1000,

(c) 3000, and (d) 10000 years. 35

3.10. Relation between (A_{int}/A_{tot}) and (a/h) for the morphologies after (a) 0, (b) 100, and (c) 1000 years. Numbers correspond to the numbering in Fig. 3.3. 36

4.1. Initial morphology used throughout this study. (a) Plan view of the morphology consisting of an offshore area, inlet, and tidal basin. Grey areas represent land regions which form impermeable and non-erodible barriers. (b) Cross section of the initial morphology. Location of the cross section is indicated by the black line in (a). 41

4.2. Predicting the morphology of a tidal embayment facing sea level rise at a rate of 5.6 mm/year for 200 years. (a) Steady-state (here defined when the root-mean-square of the bed level changes between successive years computed over all grid cells in the basin is below 2 cm) morphology generated after 400 years of bathymetric change starting from an unchannelized basin (Fig. 4.2). Tidal range is 1.5 m. (b) Expected bed elevations applying the bathtub approach. (c) Simulated bathymetry when morphology evolves during sea level rise. (d) Expected bed elevations when historical rates of morphological change (evaluated over the last 100 years) are extrapolated into the future. White, black, and grey lines represent -0.75 (low tide), 0 (mid tide), and 0.75 (high tide) m contour lines, respectively. Grey areas are land regions. 43

4.3. Simulation of tidal channel network formation for a tidal range of 1.5 m. Morphologies after (a) 5, (b) 30, (c) 100, and (d) 400 years. 44

4.4. Simulated morphology 200 years after sea level rise has stopped. The morphology is not in a steady-state at the end of sea level rise. Tidal channels keep on expanding landward and intertidal areas continue to reorganize themselves. White, black, and grey lines represent -0.75 (low tide), 0 (mid tide), and 0.75 (high tide) m contour lines, respectively. 45

4.5. Quantification of morphological change during sea level rise. The subplots show the root-mean-square of the deviation in bed elevation between non-evolving and evolving morphologies versus time. The rms-deviation was calculated for (a) the entire basin and for different segments of the basin by splitting the bathymetry prior to sea level rise into (b)

subtidal, (c) intertidal, and (d) supratidal areas. Blue, green, and red represent a tidal range of 1, 1.5, and 2 m, respectively. For all the simulations, morphologies were in a steady-state when sea level started to rise. Sea level rise rates amount to 2.8 (solid line), 5.6 (dashed-dotted line), and 11.2 (dotted line) mm/year. Black lines represent situations without sea level rise. 46

4.6. Change in channel network configuration as a result of sea level rise. (a) Number of channels and (b) channel drainage width versus distance from the coastal inlet prior to (blue circles) and immediately after (red triangles) sea level rise for a simulation carried out with a tidal range of 1.5 m and a sea level rise rate of 5.6 mm/year (the simulation presented in Figure 4.3). Channel network configuration has further adjusted 200 years after (green stars) sea level rise has stopped (channel network of the morphology presented in Fig. 4.5). Vertical dotted and solid lines approximate the position of the water level at mid tide before and after sea level rise, respectively. The solid arrows in (a) point out the decrease in the number of channels due to increasing water depths. The dashed arrow points out the increase in the number of channels due to the landward expansion of channels. The horizontal grey line in (b) shows that the channel network configuration has adjusted such that the channel drainage width at mid tide both before and after sea level rise is similar. 48

4.7. Cumulative volume of sediment transported through the tidal inlet for a tidal range of 1 m. Import (positive numbers) of sediment to and export from (negative numbers) the tidal basin vary when sea level rise rate amounts to 2.8 (solid line), 5.6 (dashed-dotted line), or 11.2 (dotted line) mm/year. Black line represent situation without sea level rise. 49

5.1. Simulation of tidal channel network formation when mangroves are not present. Morphologies after (a) 5, (b) 20, (c) 50, and (d) 140 years. Grey areas represent land regions which form impermeable and non-erodible barriers. Colorbars represent the bed elevation (m). 63

5.2. Simulated morphology after 140 years (a) without mangroves and (b) with mangroves. In the vegetated scenario mangroves started to grow

after 50 years. White, black, and grey lines represent -1 (low tide), 0 (mid tide), and 1 (high tide) m contour lines, respectively. 64

5.3. Hypsometric curves for the unvegetated and vegetated morphology after 140 years. 66

5.4. Flow field during rising tide over a part of the (a) unvegetated and (b) vegetated morphology after 140 years. Arrows on both panels represent magnitude and direction of the flow. Scale of the arrows is indicated in between the two panels. The white circles on panel (b) indicate the grid cells where mangroves are present. The axis correspond to the axis of Fig. 5.2. 68

5.5. Flow field during falling tide over a part of the (a) unvegetated and (b) vegetated morphology after 140 years. Arrows on both panels represent magnitude and direction of the flow. Scale of the arrows is indicated in between the two panels. The white circles on panel (b) indicate the grid cells where mangroves are present. The axis correspond to the axis of Fig. 5.2. 69

5.6. Number of channels versus distance from the coastal inlet for the unvegetated and vegetated morphology after 140 years. The number of channels is shown as a moving average over 500 m. The vertical dashed line represents the distance from the coastal inlet (similar for the unvegetated and vegetated scenario) for which the bed elevation averages 0 m (mid tide). 70

5.7. Part of the simulated morphology after 140 years (a) without mangroves (similar to Fig. 5.2a), (b) with mangroves (similar to Fig. 5.2b), and when only the effect of mangroves on (c) C_D, (d) θ_{cr}, (e) S_{slope}, and (f) ΔZ_{org} was included. White, black, and grey lines represent -1 (low tide), 0 (mid tide), and 1 (high tide) m contour lines, respectively. The axis correspond to the axis of Fig. 5.2. 72

5.8. Number of channels versus distance from the coastal inlet for the unvegetated (blue) and vegetated (red) morphologies after 140 years. For the vegetated scenarios only the effect of mangroves on (a) C_D, (b) θ_{cr}, (c) S_{slope}, and (d) ΔZ_{org} was included. The number of channels is shown as a moving average over 500 m. 73

5.9. Simulated morphology after 160 years of sea level rise at a rate of 5.6 mm/year (a) without mangroves and (b) with mangroves. Sea level started to rise after 140 years of morphological evolution under a stable mean water level (the morphologies shown in Fig. 5.2). White, black, and grey lines represent -1 (low tide), 0 (mid tide), and 1 (high tide) m contour lines, respectively. 74
5.10. Hypsometric curves for the unvegetated and vegetated morphology before (Fig. 5.2) and after (Fig. 5.9) sea level rise. 75
5.11. Number of channels versus distance from the coastal inlet for the unvegetated and vegetated morphology before (Fig. 5.2) and after (Fig. 5.9) sea level rise. The number of channels is shown as a moving average over 500 m. The vertical dashed blue and red lines represent the distance from the coastal inlet for which the bed elevation averages 0 m (mid tide) in respectively the unvegetated and vegetated scenario. 76

Chapter 1

Introduction

1.1 Research objective and relevance

Tidal embayments are complex environments at the boundary between land and sea. These tidal systems can be found along many parts of the world's coastline (see for example Dronkers (2005)) and are of great social, economical, and ecological importance. Human populations are increasingly concentrated near coasts (Cohen et al., 1997) and tidal embayments are of key importance to coastal communities since they offer ideal settings for harbours and because they are used as transport routes. From an ecological perspective, tidal embayments provide essential ecological functions, including nutrient production, nutrient cycling, decomposition, and habitats for many vegetation types and benthic organisms (Levin et al., 2001). Moreover, tidal embayments serve as nursery grounds for recreationally and commercially important fish (Levin et al., 2001). Fringing ecosystems such as salt marshes and mangrove forests provide a further benefit by buffering inland development from the full force of incoming storm surges (Mazda et al., 2006; Koch et al., 2009).

Unfortunately, tidal embayments are also very sensitive to environmental changes, both anthropogenic and natural. Human pressures on earth's environmental systems are increasing (Vitousek et al., 1997) and sea level rise, for example, is one of the major outcomes of an anthropogenically-driven shifting climate which will have a strong impact on tidal systems. This change in sea level will impact the tidal environment by changing the inundation regime, but also by modifying the tidal prism, which feeds back into changes of the sea bed topography. Modification of this morphology in turn not only changes the tidal currents, but also changes the structure of the physical controls on ecosystems, and thus will have serious economical and ecological implications. Our ability to manage tidal embayments successfully and maintain their value hinges on our knowledge of the system. The morphological behaviour of tidal embayments, however, is very complex because of the variety of controlling and not fully

understood processes that shape the feedbacks which lead to morphological change. Therefore the main objective of this research is to improve the understanding of tidal embayment evolution driven by both physical and biological processes.

Many previous studies have elucidated the importance of the interactions between hydrodynamics, sediment transport, and the evolving topography in driving the morphological evolution of tidal embayments (e.g. Schuttelaars and de Swart, 1999; Hibma et al., 2003; D'Alpaos et al., 2005; Marciano et al., 2005; van der Wegen and Roelvink, 2008; van der Wegen et al., 2008; Stefanon et al., 2010). These morphodynamic interactions (Fig. 1.1a) give rise to the emergence of various landform patterns and fascinating morphological behaviour (Coco and Murray, 2007) and thus need to be incorporated in the study of the evolution of tidal environments. In recent years, the biology has become recognized as an additional fundamental factor in shaping environmental systems (Murray et al., 2008; Reinhardt et al., 2010) and the effects of physical-biological interactions on the morphological evolution of tidal landscapes have also been explored over a range of spatial and temporal scales (e.g. Morris et al., 2002; van de Koppel, 2005; D'Alpaos et al., 2006; D'Alpaos et al., 2007a; Kirwan and Murray, 2007; Temmerman et al., 2007; Mariotti and Fagherazzi, 2010; Marani et al., 2010). When biology is present, the complexity of the system increases because of the extra interactions and feedback mechanisms (Fig. 1.1b).

In tropical and subtropical regions, a dominant role in controlling tidal embayment dynamics is played by mangroves. Mangroves are halophytic (salt-tolerant) plants comprising many different species (Tomlinson, 1986). They occur in sheltered tidal environments and can grow on a variety of substrates. The habitat of mangroves is restricted to a specific range of bed elevations with characteristic hydrodynamic conditions (Krauss et al., 2008). In turn, mangroves affect both hydrodynamic and sediment transport processes (e.g. Mazda et al., 2005; Quartel et al., 2007; van Santen et al., 2007) and thus play a role in determining the bed elevation so that a coupled physical-biological system arises. In this research the effects of the *Avicennia marina* on morphological evolution are explored. The *Avicennia marina* is a mangrove species which occurs in both

hemispheres (Duke, 1990) and also extends its range into cooler warm-temperate climates.

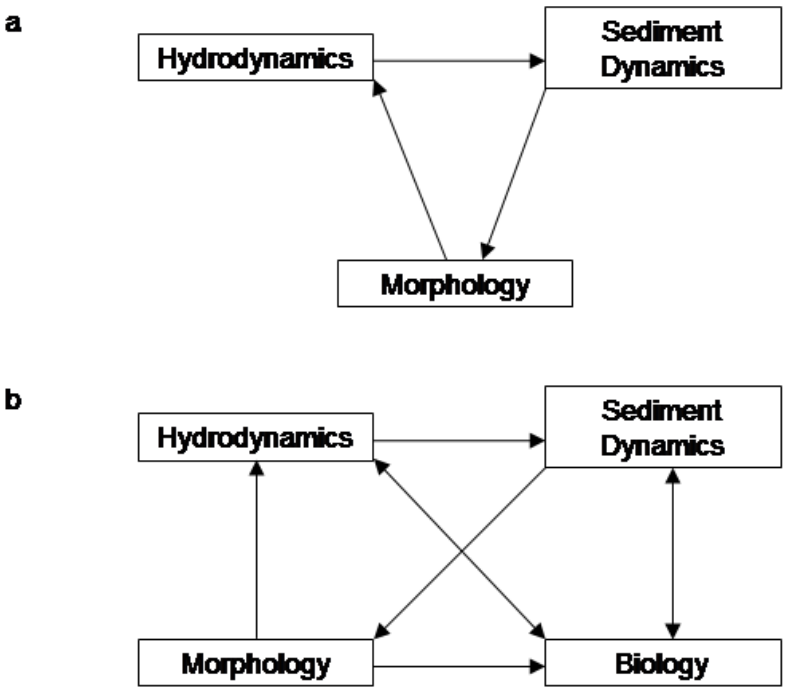

Figure 1.1. Schematized diagram of the (a) morphodynamic and (b) biomorphodynamic feedback cycle. Biology affects morphology via feedbacks between biology and hydrodynamics and/or sediment dynamics.

1.2 Approach and research questions

Tidal embayments evolve over timescales ranging from decades to millennia. Process-based measurement or mapping studies are therefore not ideal for investigating the evolution of these environments. Conversely, mathematical modelling provides an approach to study tidal embayments which can, with the appropriate assumptions, operate over long timescales. Here a numerical model is developed which accounts for the complex interactions between physical and biological processes and is capable of simulating the long-term morphological evolution of tidal embayments. The model is used to explore this evolution under a range of forcing and environmental conditions with the purpose of obtaining answers to the following research questions:

1. How do tidal range and initial bathymetry affect the morphological evolution of tidal embayments?
2. How do tidal embayments respond to sea level rise?
3. How do mangroves affect the morphological evolution of tidal embayments?

Answering these research questions contributes directly to the overall aim of this research to improve our understanding of tidal embayment evolution.

1.3 Thesis outline

This thesis describes the development and application of a numerical model capable of simulating tidal embayment evolution. The thesis is presented as four working chapters, each including its own introduction which gives an overview of relevant literature and sets the context for the results presented. Each chapter represents a separate aspect to the modelling study, with its own methodology, analysis of model simulations, and results. As such, the four working chapters are intended to stand alone as separate studies on a related theme.

In Chapter 2, the development of the numerical model is described which is capable of simulating morphological change as a result of the interactions between hydrodynamics, sediment transport, and the evolving topography. Long-term morphological evolution of a tidal embayment and associated changes in hydrodynamic conditions are discussed. Furthermore, a sensitivity analysis is presented to show how model outcome is dependant on changes to the initial set up. Chapter 2 has been accepted for publication in the “Australian Journal of Civil Engineering”.

In Chapter 3, model simulations that show how tidal range and initial bathymetry influence the evolution of tidal basins and control the type of channel network that develops are discussed.

In Chapter 4, the model is used to explore the response of tidal embayments to sea level rise.

In Chapter 5, it is explained how the interactions between mangroves and physical processes are incorporated into the numerical model. Model results are analyzed with regard to the influence of mangroves on tidal channel network evolution.

In Chapter 6, the findings of previous chapters are summarized and potential directions of future research are discussed.

In addition, a paper on the use of neural networks to model sediment transport, that I completed and was accepted for publication in “Nonlinear Processes in Geophysics” during the development of the thesis, is presented in Appendix A. Although this work does not contribute directly to the theme of the thesis, it indicates that neural networks can be used to improve predictions of sediment dynamics, which is one of the key ingredients in both the morphodynamic and the biomorphodynamic feedback loop (Fig. 1.1).

Chapter 2

A numerical model to simulate the formation and subsequent evolution of tidal channel networks

2.1 Introduction

Estuaries show a variety of distinctive geomorphic shapes and features that reflect differences in environmental conditions, such as geological constraints, hydrodynamic forcing (e.g. tidal range, wave climate), sediment loads from the catchment, and the presence and types of both vegetation and benthic organisms. These differences yield varying patterns of sediment erosion/deposition and consequently determine the current shape of the estuary and its future evolution. Understanding how estuarine morphologies evolve under the influence of both natural and anthropogenic drivers is of key importance to coastal communities. Not only are estuaries used as transport routes, when vegetation such as mangrove trees or salt marsh plants is present they also provide one of the most biologically-productive ecosystems of the planet (Mitsch and Gosselink, 2007). These dynamic ecosystems provide habitats for a variety of benthic organisms and nursery grounds for fish (Levin et al., 2001). Therefore, long term changes to the morphology and ecology of estuaries can have serious economic and social implications. Moreover, salt marshes and mangrove forests provide a further benefit by protecting coastal cities against severe weather because they absorb the force of incoming storm surges so that waves and currents are weaker when they reach inland areas (Mazda et al., 2006; Koch et al., 2009).

So far, it has not been possible to accurately predict the evolution of estuaries because of the variety of governing processes in such systems which are not yet fully-understood. A numerical model, aimed at producing quantitative predictions of estuarine evolution, should account for the complex feedback relationships between hydrodynamics, sediment transport, biology, and morphological change. These so-called biomorphodynamic interactions have already proved to be of crucial importance in explaining the behaviour of various environmental systems, including aeolian dune landscapes (Baas, 2002), braided patterns in river systems

(Murray and Paola, 2003), arctic landscapes (Daanen et al., 2008), and salt marshes (D'Alpaos et al., 2007a; Kirwan and Murray, 2007). A biomorphodynamic estuarine model, which incorporates physical-biological interactions over long timescales, could be used to simulate the response of estuaries to different scenarios of sediment supply, vegetation type and density, and sea level rise. Consequently, this type of model would improve our knowledge of estuarine evolution and provide the foundation for sound coastal management decisions. However, before such a fully-coupled estuarine numerical model can be used to make reliable predictions, the model's capability of reproducing well-known morphological behaviour of estuarine systems must be tested. An estuarine model should be capable of simulating the formation and subsequent evolution of tidal channel networks. These networks often exhibit complex morphological patterns and affect both the short- and the long-term evolution of the overall estuarine environment.

Despite their importance, observations of the formation and evolution of channel networks in tidal systems usually involve large spatial and temporal scales so that detailed studies are limited. Hughes et al. (2009) discussed the rapid expansion of tidal creeks onto an established marsh platform. The development of the creeks is reported to be the result of biological feedbacks involving the dieback of vegetation coupled with intense burrowing by crabs producing a bare and topographically depressed region beyond the channel head toward which the channel extends. Observations of channel formation on a tidal flat were described by Temmerman et al. (2007) and it was shown that vegetation played a crucial role in the morphological evolution. Ginsberg and Perillo (2004) used detailed bathymetric data of an estuary along the Argentina coast to describe changes in the cross-sectional shape of channels and to determine lateral migration rates of the channels.

The use of laboratory experiments has also provided insight into the initiation of tidal channel networks. Stefanon et al. (2010) started their experiments with a plane horizontal tidal flat and showed how the headward growth of initiated channels and tributary addition drove expansion of the network and shaped the intertidal morphology. Furthermore, a wide variety of numerical models have

been applied to the study of tidal channel network formation. Schuttelaars and de Swart (1999) demonstrate that channels and shoals in short tidal embayments develop as a result of the positive feedback between tidal flow and the bottom. They modelled the water motion by using the depth-averaged shallow water equations and assumed that sediment transport only occurs because of diffusive processes and bed slope effects. Their analysis indicates that friction plays a key role in the growth of bottom perturbations which were added onto a stable equilibrium profile. Bottom friction caused the velocity to become slightly smaller above shoals and larger in the channels, causing a net sediment flux from the channels towards the shoals which resulted in the growth of bedforms. A numerical model developed by D'Alpaos et al. (2006) was used to show how the evolution of a cross section of an initiated tidal channel was driven by changes in the tidal prism after the emergence of a marsh platform. D'Alpaos et al. (2005) simulated tidal network initiation and its progressive headward extension within tidal flats by using a simplified hydrodynamic model and relationships describing tidal channel characteristics. This model has been tested against observations made from an expanding tidal network within a salt marsh in the Venice Lagoon (D'Alpaos et al., 2007b) and it has been shown that the model is capable of reproducing key statistical properties of the observed network. Di Silvio et al. (2010) used a different technique and calculated tidally time-averaged sediment concentrations to determine the long-term net transport of sediments. Deposition and erosion depended on the difference between the local time-averaged and local equilibrium concentration. This two-dimensional model was capable of simulating the formation of a channel network in a tidal lagoon.

A different modelling approach to study channel network formation is provided by the coupling of comprehensive hydrodynamic models and commonly used sediment transport formulations. Hibma et al. (2003) simulated morphological evolution by coupling the solution of the unsteady depth-averaged shallow water equations with the sediment transport models developed by Engelund and Hansen (1967) and van Rijn (1984). In their study, the flow module provided the flow fields throughout one tidal cycle. Sediment transport computations were performed for each phase of this tidal period. The tidally-averaged sediment transport field was used to compute bed level changes. To facilitate the execution

of long-term simulations, these bathymetric changes were then increased linearly over the morphological time step, which was determined automatically on the basis of the Courant number for bed level perturbations. The model simulated the formation of channel and shoal patterns in an elongated tide-dominated schematic estuary. Marciano et al. (2005) used a similar model to simulate the formation of branching channel patterns in a short idealized basin. The model was capable of reproducing geomorphic characteristics that favourably compared to field observations. Van der Wegen et al. (2008) also conducted long-term morphodynamic simulations and showed that initially non-patterned basins evolve toward a state of less morphodynamic activity in which morphologic developed patterns are relatively stable. They, however, used a different technique to overcome the problem related to the difference in time scales over which hydrodynamic and morphodynamic processes occur. Bed level changes, computed every hydrodynamic time step, were multiplied with a morphological factor and the updated bathymetry was used in the next hydrodynamic time step. Dissanayake et al. (2009) applied the same technique and used a schematized model domain, with dimensions similar to the Ameland inlet in the Dutch Wadden Sea, to test the sensitivity of morphological behaviour to the initial inlet width, direction and asymmetry of the tidal forcing, and the relative position of the tidal basin with respect to the inlet. Cayocca (2001) developed a model which is also capable of simulating long-term morphological evolution. Different modules for hydrodynamics, waves, sediment transport, and bathymetry updates were combined to determine the governing processes in the evolution of a tidal inlet along the French Atlantic coast.

Here we follow the approach of coupling a comprehensive hydrodynamic model with the Engelund and Hansen (1967) sediment transport formula and applying a technique to increase the rate of bed level changes. The numerical model is used to simulate the formation of complex tidal channel networks. This type of morphodynamic model, which is capable of simulating the long-term evolution of tidal systems, has become increasingly popular in recent years. These models are developed by coupling different modules describing hydrodynamics, sediment dynamics, and bed elevation change and all these processes interact with each other in a complex way. Because of the complexity of such a fully-coupled model

our work will demonstrate the necessity of performing a detailed sensitivity analysis with the purpose of gaining insight into the model response to changes in the initial set up. We will describe the effect of the numerical scheme adopted, hydrodynamic and morphological time steps, and initial bathymetry on model outcome. The long-term goal of the model we are developing is to examine the response of estuaries to different scenarios of environmental conditions (e.g. sea level rise) and the role of biological and physical interactions.

2.2 Model description and set-up

2.2.1 Model description

The numerical model developed and used throughout this study simulates morphological change as a result of the interactions between hydrodynamics, sediment transport, and bed elevation change. The model thus accounts for the interactions related to the morphodynamic feedback loop. Fluid flow is simulated using ELCOM (Estuary and Lake Computer Model; Hodges et al., 2000) which is a 3D hydrodynamic model based on the unsteady Reynolds-averaged Navier-Stokes equations for incompressible flow using the hydrostatic assumption and closed by a turbulent closure scheme. We use a 3D-model so that eventually the model can be adjusted to account for a river input and associated density differences. At this stage we include only a minimum number of processes so that model results are as transparent as possible. Influences of Coriolis force, density differences, wind, and waves are therefore neglected. The continuity and the momentum equations in this case read:

$$\frac{\partial u}{\partial x}+\frac{\partial v}{\partial y}+\frac{\partial w}{\partial z}=0\,, \qquad (2.1)$$

$$\frac{\partial u}{\partial t}+u\frac{\partial u}{\partial x}+v\frac{\partial u}{\partial y}+w\frac{\partial u}{\partial z}=-g\frac{\partial \eta}{\partial x}+\nu_x\frac{\partial^2 u}{\partial x^2}+\nu_y\frac{\partial^2 u}{\partial y^2}+\nu_z\frac{\partial^2 u}{\partial z^2}\,, \qquad (2.2)$$

$$\frac{\partial v}{\partial t}+u\frac{\partial v}{\partial x}+v\frac{\partial v}{\partial y}+w\frac{\partial v}{\partial z}=-g\frac{\partial \eta}{\partial y}+\nu_x\frac{\partial^2 v}{\partial x^2}+\nu_y\frac{\partial^2 v}{\partial y^2}+\nu_z\frac{\partial^2 v}{\partial z^2}\,, \qquad (2.3)$$

where u, v, and w are the velocity components in the horizontal x-, y- and in the vertical z-direction, respectively; t = time; g = gravitational acceleration; υ_x, υ_y,

and υ_z are eddy viscosity coefficients; η is the water level and its evolution can be described as:

$$\frac{\partial \eta}{\partial t} + \frac{\partial}{\partial x}\left(\int_{-h}^{\eta} u dz\right) + \frac{\partial}{\partial y}\left(\int_{-h}^{\eta} v dz\right) = 0, \quad (2.4)$$

where h is the water depth. The solution grid uses rectangular Cartesian cells, enabling the application of a simple, efficient finite-difference/finite-volume scheme on a staggered grid. In the vertical dimension, ELCOM applies a z-coordinate system. The numerical scheme for computing the temporal evolution of velocity is a semi-implicit solution of the governing equations using a hybrid discretization of advective terms. ELCOM includes a proper description of the flooding and drying of grid cells. A grid cell is considered to be dry only if the total water depth at the cell center and at all the four sides surrounding the cell does not exceed zero. No mass flux is permitted to cross the side of a grid cell when this side is dry.

An analysis was performed which indicated that a period of one tidal cycle is sufficient to spin up the hydrodynamic model over the simplified domains we are using. The flow velocities computed every hydrodynamic time-step during the second tidal cycle were used to obtain instantaneous sediment transport rates which were calculated according to the formula developed by Engelund and Hansen (1967):

$$S_{flow} = \frac{0.05U^5}{\sqrt{g}C^3\Delta^2 D_{50}}, \quad (2.5)$$

where S_{flow} = sediment transport flux; U = magnitude of flow velocity; C = Chézy coefficient; Δ = relative density $(\rho_s-\rho_w)/\rho_w$; ρ_s = sediment density; ρ_w = water density; D_{50} = median grain size. Slope-driven sediment transport S_{slope} is incorporated in the model by following the approach of Kirwan and Murray (2007):

$$S_{slope} = \alpha b, \quad (2.6)$$

where α is a dimensional constant and b is the slope towards the neighboring grid cell. Here slope-driven sediment transport only occurs when b exceeds 0.01. Gradients in sediment transport rate yield bed level changes due to conservation of sediment mass:

$$\left(1-\varepsilon_{por}\right)\left(\frac{\partial z_b}{\partial t}\right)+\left(\frac{\partial S_x}{\partial x}+\frac{\partial S_y}{\partial y}\right)=0\,, \qquad (2.7)$$

where ε_{por} = bed porosity (kept fixed and equal to 0.4); S_x and S_y are the total sediment transport fluxes in the x- and y-direction, respectively. Equation (2.7) is solved using the upwind scheme so that the type of discretization is dependent on the flow direction. Because of the evolving morphology and the reversing flow conditions associated to tides, the scheme is adjusted to account for diverging and converging flows. Different numerical schemes were assessed and will be discussed in the results section. All the models which have been developed to simulate long-term morphological evolution of tidal systems (e.g. Cayocca, 2001; Hibma et al., 2003; Marciano et al., 2005; van der Wegen et al., 2008; Dissanayake et al., 2009) apply a technique to accelerate bed level changes. In this study we first integrated bed level changes over one tidal cycle and then multiplied these changes by a number of tidal cycles before morphological change feeds back into the hydrodynamic model. We adopted a varying morphodynamic time-step and assumed that hydrodynamic conditions remained constant until bed level changes exceeded 10% (sensitivity of model outcome to this number will be described in the results section) of the local water depth at high tide.

2.2.2 Model set-up

The initial topography covered an area of 17×17 km and was composed of an offshore area, inlet, and basin (Fig. 2.1a). Bed elevations in the offshore area, which extended 7 km seaward, increased from -8 m at the seaward boundary to -2 m at the entrance of the basin (Fig. 2.1b). The offshore area was separated from the tidal basin by the presence of land regions which form impermeable and non-erodible barriers. Within the basin, bed elevation further increased towards +2 m at the landward boundary and random perturbations of -1.5 to +1.5 cm were added to the bed level in this area. The model was forced with a semidiurnal sinusoidal

tide and the tidal range was 2 m. Therefore, during high tide a large part of the tidal basin remains dry (in contrast for example with Marciano et al. (2005) and Dissanayake et al. (2009)) so that tidal channels can expand towards the shallow areas in the upper part of the basin. A grid size of 100 m in both x- and y-direction was used. The thickness of the horizontal layers was kept at a uniform value of 40 cm. The hydrodynamic time-step was set to 2 minutes, unless stated otherwise. The sediments had a mean grain size diameter of 0.12 mm and a value of 65 $m^{0.5}/s$ has been used for the Chézy coefficient. Slope-driven sediment transport was calculated using $\alpha = 1.16 \times 10^{-5}$ m^2/s.

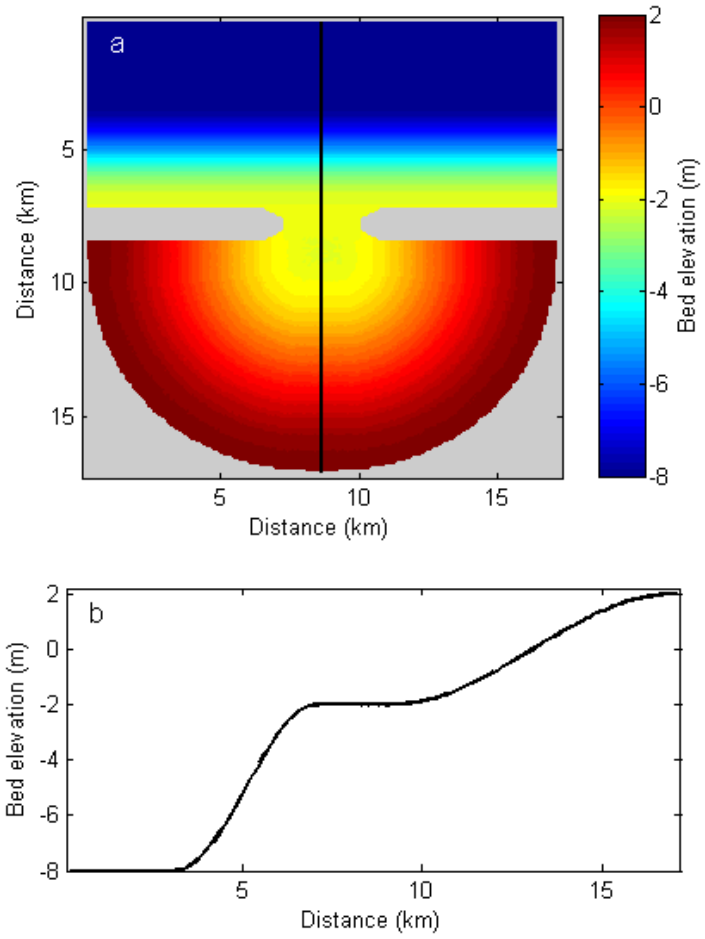

Figure 2.1. (a) Plan view of the initial morphology used throughout this study. The morphology consists of an offshore area, inlet, and tidal basin. Grey areas represent land regions which form impermeable and non-erodible barriers. (b) Cross section of the initial morphology. Location of the cross section is indicated by the black line in (a).

2.3 Results

The solution of the equation for conservation of sediment mass (Eq. 2.7) is highly dependent on the numerical scheme being used (Long et al., 2008). Earlier versions of the numerical solver applied central difference techniques (both first-order and higher-order) to solve the continuity equation. A weakness of central difference techniques is that these techniques are likely to produce spurious oscillations (Long et al., 2008). In our simulations, the use of central difference schemes resulted in localized numerical instabilities which led to unrealistic morphological evolution with the formation of closely-spaced ridges in the area close to the inlet where the flow velocities are high. Conversely, the upwind scheme was capable of producing oscillation-free, and therefore physically plausible, solutions. The model results which will be presented in the remainder of this paper are all generated by applying the upwind scheme.

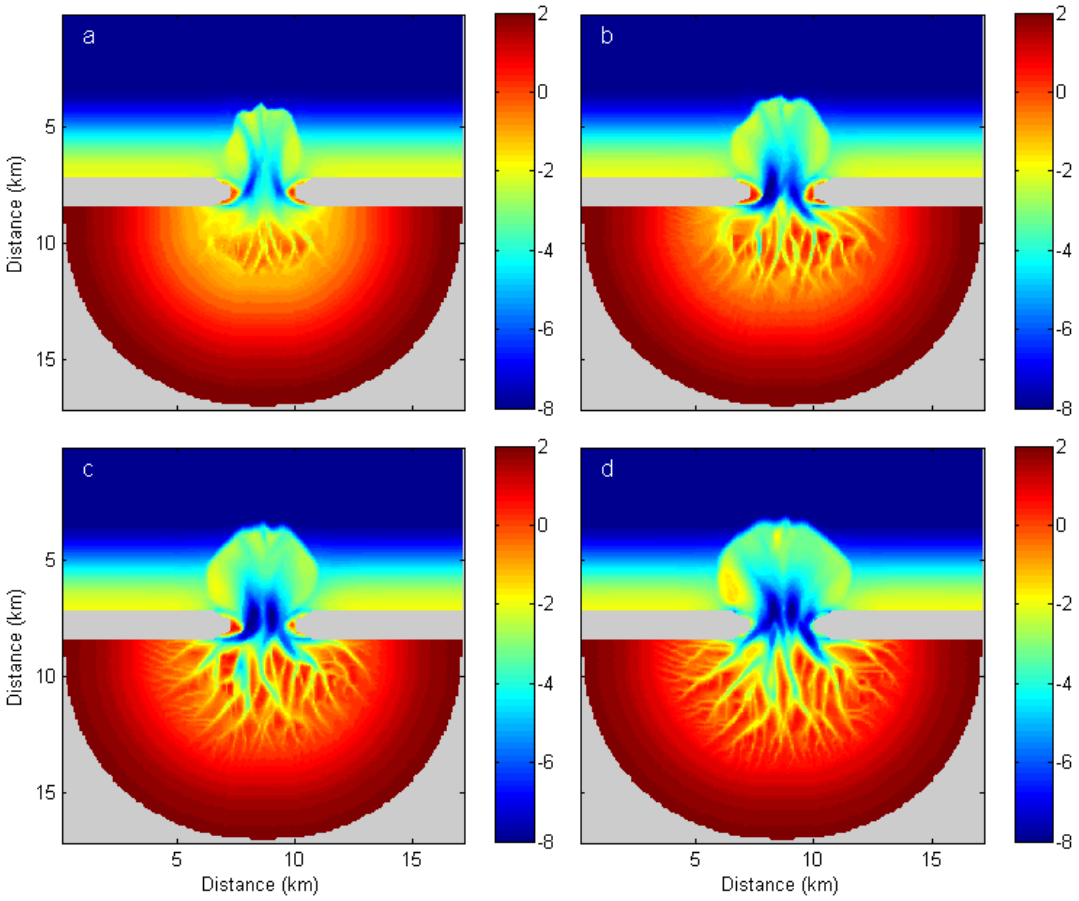

Figure 2.2. Simulation of tidal channel network formation. Morphologies after (a) 5, (b) 30, (c) 80, and (d) 250 years.

The numerical model was capable of simulating realistic bathymetric evolution (Fig. 2.2). Because of the shallow character of the tidal basin, large (of the order of meters in the vertical direction) morphological changes occurred within the first 5 years (Fig. 2.2a). Two deep channels rapidly developed in the inlet of the tidal system. During ebb-tide, large volumes of sediment were transported towards the offshore area where decelerating flows caused sediment deposition. Consequently, a large ebb-tidal delta formed which extended more than 3 km offshore after just ten years of evolution. In the basin, small-scale channels developed and intertidal areas emerged. In the following decades (Fig. 2.2b-d) the channels through the inlet continued to deepen and reach a maximum depth of about 9 m after 250 years (Fig. 2.2d). The ebb-tidal delta increased in size and the tidal channels in the basin kept on branching. This process of branching of the channels ultimately resulted in the formation of a complex tidal channel network (Fig. 2.2d).

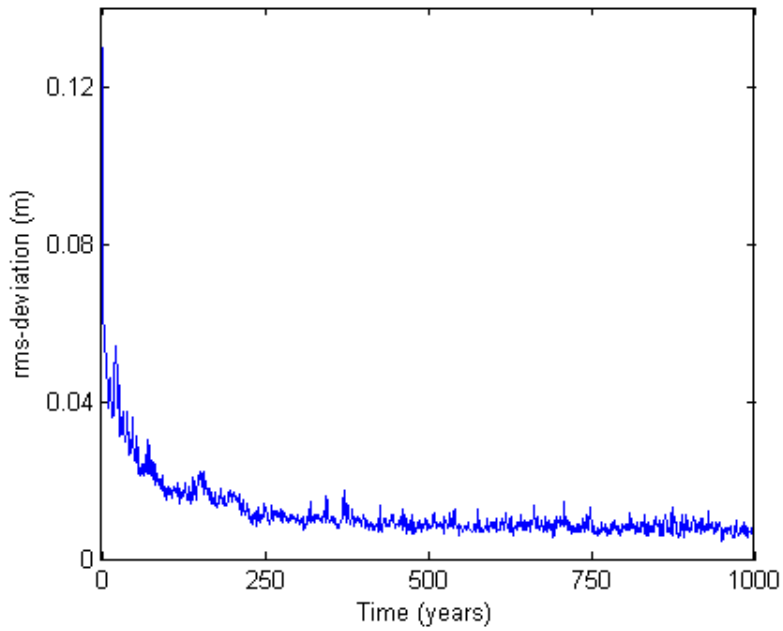

Figure 2.3. Root-mean-square of the bed level changes between successive years computed over all grid cells in the basin as a function of time.

The long-term simulations of bathymetric change in a tidal embayment as reported by van der Wegen et al. (2008) indicate that energy dissipation decreases over time and relatively stable morphologic patterns evolve. To explore this idea

of a decrease in morphodynamic activity over time we computed the root-mean-square of the bed level changes between successive years over all the grid cells in the basin (Fig. 2.3). As mentioned before, the initiation of tidal channels within the first few years caused large changes in the bathymetry, resulting in relatively large rms-deviation values. The root-mean-square of the bathymetric changes during the first year is 13 cm. Subsequently, new channels form and existing channels migrate, become wider and deeper, and branch, but the overall morphological evolution occurs at a slower pace (Fig. 2.3). The rate, at which the reduction in morphodynamic activity occurs, decreases over time. For the present simulation, the tidal basin reaches a state in which the morphodynamic activity is relatively constant (Fig. 2.3).

The channel network forms as a result of feedback-interactions between hydrodynamics, sediment transport, and bed level, suggesting that the hydrodynamic conditions change during morphological evolution. With the purpose of showing how the magnitude and the direction of the flow change we extracted flow fields during rising tide as computed by the hydrodynamic model. Figure 2.4a shows the velocity vectors over the initial morphology. The flow pattern in the basin consists of two more or less symmetrical circulation cells and the flow reaches a maximum value of about 1 m/s. Due to the small cross-sectional area of the inlet at the beginning of the simulation, the flow accelerates strongly in this part of the domain (Fig. 2.4a). Flow acceleration leads to positive gradients in sediment transport and thus sediment erosion. Erosion of the bed causes an increase in the cross-sectional area which, in turn, reduces the flow accelerations as can be observed in Figure 2.4b. The formation of the channel network affects the behaviour of the flow further with large velocities occurring in the channels and small velocities in the shallow areas. The channel network has a strong control on the overall flow pattern and the two large-scale circulation cells, which formed over the initial morphology (Fig. 2.4a), have disappeared.

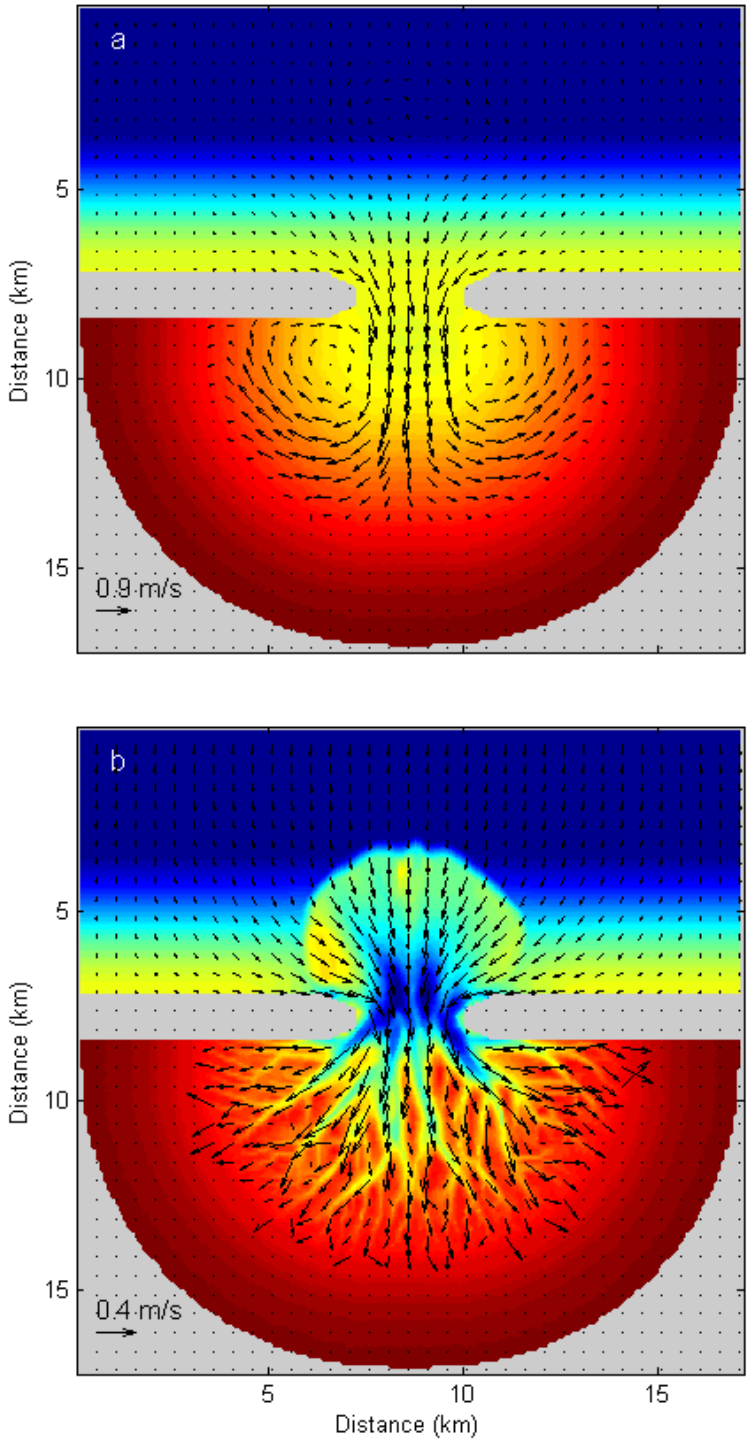

Figure 2.4. Flow field during rising tide over (a) the initial morphology and over (b) the simulated morphology after 250 years. Arrows on both panels indicate magnitude and direction of the flow. Scale of the arrows is indicated in the left-bottom corner. Velocity vectors are shown every fifth grid cell.

Changes in the hydrodynamics during morphological evolution have been further analyzed in terms of tidal asymmetry. Asymmetry between the flood and ebb tidal currents is an important physical mechanism that affects the long-term morphological evolution by driving tidally-averaged sediment transport (de Swart and Zimmerman, 2009). Figure 2.5a shows time-series of tidal elevation and velocity for the initial bathymetry obtained for a grid cell located in the tidal basin about 2.5 km in front of the centre of the coastal inlet. Because of the large-scale flow pattern (Fig. 2.4a), the flow is highly asymmetrical with flood currents reaching a peak velocity of more than 0.80 m/s while the peak current during ebb is about -0.25 m/s. The peak flood velocity occurs 2 hours after maximum gradients in rising water levels are reached. The formation of channels and intertidal areas alters the flow pattern (Fig. 2.4b) and counteracts the dominance of the flood current (Dronkers, 2005) such that much of the tidal asymmetry has disappeared after 250 years (Fig 2.5b). The ebb current has even become slightly stronger (-0.34 m/s) than the flood current (0.28 m/s). Peak flood velocity now coincides with the greatest steepness of rising tide.

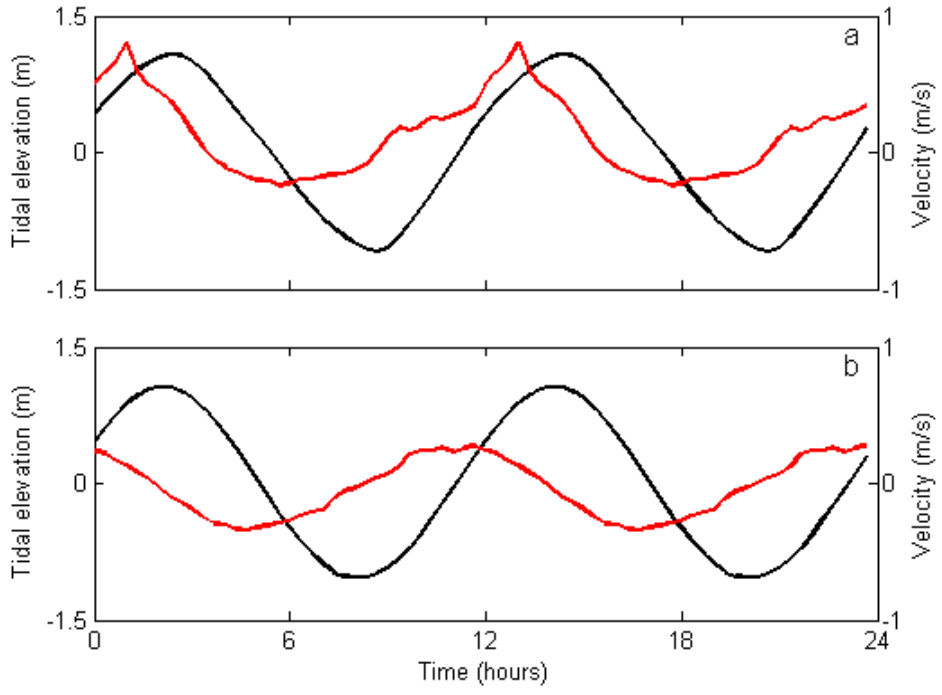

Figure 2.5. Time series of tidal elevation (black) and velocity perpendicular to the coastline (red) for (a) the initial morphology and (b) the simulated morphology after 250 years. Time series represent two tidal cycles and are obtained for a grid cell located in the tidal basin about 2.5 km in front of the centre of the inlet.

Hydrodynamic models are sensitive to the time-step at which the computations are being performed. ELCOM is unconditionally stable for purely barotropic flows (Hodges, 2000). However, the use of large hydrodynamic time-steps becomes problematic when the solution of ELCOM is coupled to sediment transport and morphology modules, as in the present study. Figure 2.6 shows the simulated morphology when a hydrodynamic time-step of 4 minutes is used. It is clear that, when this morphology is compared with the outcome of the simulation performed with a hydrodynamic time-step of 2 minutes (Fig. 2.2a), the use of a large hydrodynamic time-step results in numerical instabilities. This stresses the importance of carefully analyzing the outcome of this type of model which couples hydrodynamics, sediment dynamics and morphological evolution. When the flow field is not computed properly, which is the case when the hydrodynamic time-step is too large, unreliable small-scale bed level changes feed back into the hydrodynamic computations which ultimately result in false predictions of morphological evolution.

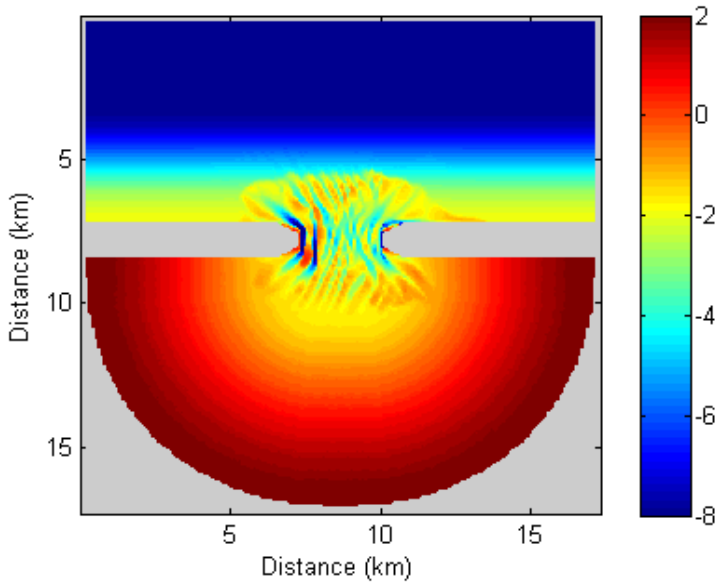

Figure 2.6. Simulated morphology after 5 years (allows for a comparison with Fig. 2.2a) when the time-step of the hydrodynamic model is set to 4 minutes.

The long-term simulations carried out here were made by assuming that the hydrodynamic conditions remain constant until bed level changes exceed a certain specified percentage of the local water depth at high tide. Results presented so far were produced by simulations for which this percentage was set to 10, following

the work by van der Wegen et al. (2008). In essence, this percentage defines the morphological time-step (in contrast to the hydrodynamic time step discussed in the preceding paragraph) and to test the sensitivity of model outcome to the value of this parameter, we performed two extra simulations by decreasing and increasing the percentage to respectively 5 and 15. Model results were analyzed after 80 years (Fig. 2.7). Although differences in the detail of model outcome can be detected, the general behaviour of the tidal system and the characteristics of the channel network are comparable. Small morphological time-steps force the hydrodynamic conditions to be updated more frequently, but this also results in additional computational effort. A good balance is required between capturing the physical interactions leading to morphological change and the computation time needed to allow large-scale pattern development.

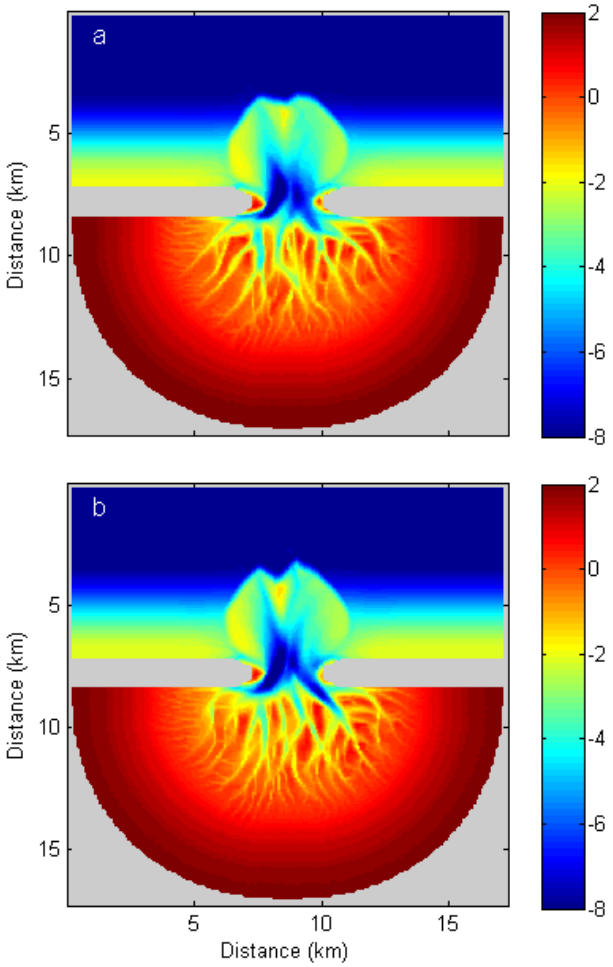

Figure 2.7. Simulated morphologies after 80 years (allows for a comparison with Fig. 2.2c) when the hydrodynamic conditions are assumed to remain constant until bed level changes exceed (a) 5% or (b) 15% of the local water depth at high tide.

To explore the effect of the initial bathymetry on morphological change we adjusted the initial bathymetry by adding one (Fig. 2.8a) or two (Fig. 2.8c) Gaussian-shaped humps with a height of 1.0 m onto the surface bottom. The top of the Gaussian humps lies between a bed elevation of -0.30 and -0.25 m. The humps affect the flow field which then affects the sediment transport and bathymetric evolution. Channels and intertidal areas which develop occur therefore at different locations (Figs. 2.8b and d). The humps migrate, the shapes of the humps change, and the height decreases. Over time, the humps disappear and ultimately the humps do not control the formation of the channel network pattern.

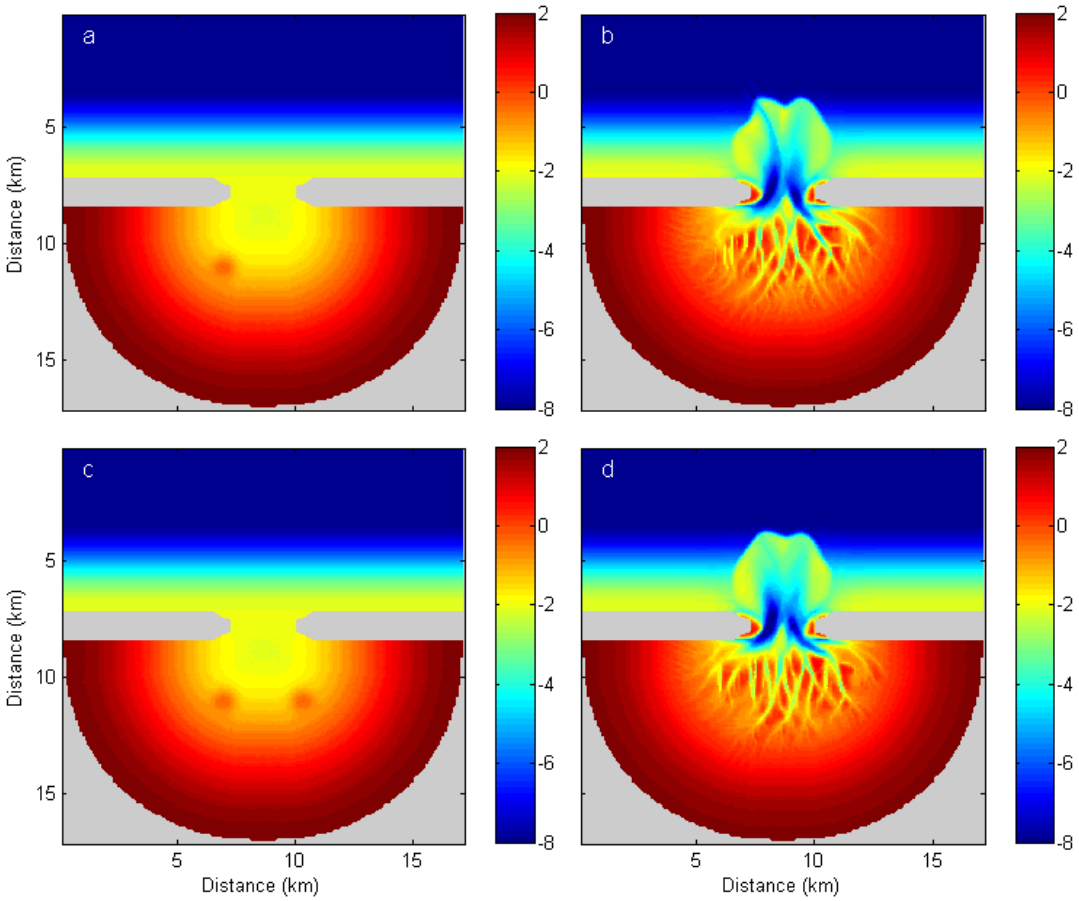

Figure 2.8. (a) Initial bathymetry onto which one bump is added and (b) its corresponding morphology after 30 years (allows for a comparison with Fig. 2.2b). (c) Initial bathymetry onto which two bumps are added and (d) its corresponding morphology after 30 years.

2.4 Conclusions

A model is presented which simulates morphological evolution by coupling hydrodynamics, sediment transport, and bed level change. Long-term simulations are performed by assuming that the hydrodynamic conditions remain constant unless significant changes in the bathymetry have occurred. The model simulates the formation of complex tidal channel networks. Over time, morphodynamic activity reduces and changes in hydrodynamic conditions occur as a result of morphological evolution. The formation of tidal channels and intertidal areas affects both the large scale flow patterns as well as the asymmetry between flood- and ebb-tidal currents. Additional model simulations revealed that model performance is highly dependent on the numerical scheme used to solve the sediment continuity equation and the time-step adopted in the hydrodynamic model. Conversely, changes to the morphological time-step or initial bathymetry influence only the details of the model outcome (e.g. the location of channels and intertidal areas), but do not affect the overall characteristics of the channel network that develops.

Chapter 3

Modelling the effects of tidal range and initial bathymetry on the morphological evolution of tidal embayments

3.1 Introduction

Tidal embayments host a wide variety of landscape features and morphological patterns with tidal channel networks arguably being the most striking example (Fig. 3.1a). These channel networks have a strong control on the hydrodynamics and sediment transport and affect therefore both the short- and long-term morphological evolution of tidal environments (Dronkers, 2005). Tidal environments are amongst the most productive ecosystems in the world (Mitsch and Gosselink, 2007) and understanding their behaviour has become increasingly important, especially in the context of climate change. Because of the influential character of channel networks, numerous studies (e.g. Schuttelaars and de Swart, 1999; Hibma et al., 2003; Marciano et al., 2005; van der Wegen and Roelvink, 2008; Stefanon et al., 2010) have been performed which focus on their initial formation and subsequent evolution. Obtaining observations of channel network formation is a daunting task because of the large spatial and temporal scales involved. Alternative approaches to study the dynamics related to channel networks have then also been found in the use of laboratory studies and numerical models.

Laboratory experiments have been conducted to explore the dynamics of single tidal channels (Tambroni et al., 2005) as well as the initiation of complete tidal networks and their progressive morphodynamic evolution starting from a plane horizontal tidal flat (Stefanon et al., 2010). In the latter experiment it was shown that headward growth of the initiated channels and tributary addition drove expansion of the network and shaped the intertidal morphology. Many examples exist of numerical modelling studies, such as the use of stability analysis to focus on the initial formation of channels and shoals (Schuttelaars and de Swart, 1999), the application of simplified hydrodynamic models and relationships describing tidal channel characteristics to simulate the formation of tidal networks within

tidal flats (D'Alpaos et al., 2005; D'Alpaos et al., 2007b), and the development of models in which deposition and erosion rates depend on the difference between the local time-averaged and local equilibrium sediment concentration to reproduce the formation of a channel network in a tidal lagoon (Di Silvio et al., 2010). A different modelling approach to study channel network formation was adopted by Marciano et al. (2005) who simulated morphological evolution by coupling the solution of the unsteady depth-averaged shallow water equations with a sediment transport module based on the formulation of Engelund and Hansen (1967). The model simulated the evolution of branching channel patterns in a short idealised basin. Similar type of models have also been used to simulate channel and shoal patterns in elongated tide-dominated schematic basins (Hibma et al., 2003; van der Wegen and Roelvink, 2008; van der Wegen et al., 2008).

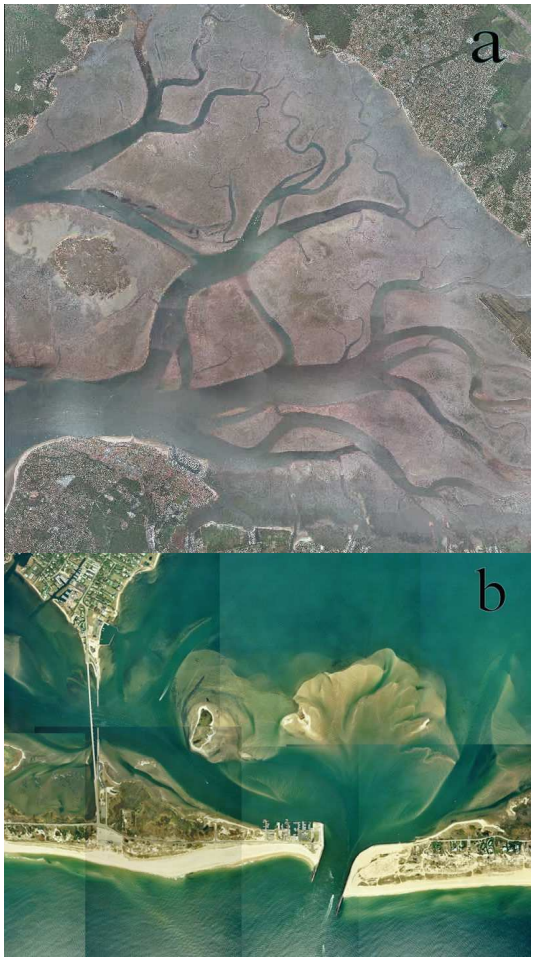

Figure 3.1. Aerial view of a (a) well developed (Bassin d'Arcachon, France) and (b) underdeveloped (Shinnecock Inlet, USA) tidal channel network.

Laboratory experiments and the wide variety of modelling studies have provided useful insight into the processes governing channel network formation and have highlighted the importance of the interactions between hydrodynamics, sediment transport, and the evolving morphology. Tidal basins in natural systems, however, do not always exhibit extensive tidal channel networks. In some tidal basins a channel network is even absent and a flood-tidal delta is present (Fig. 3.1b). Large intertidal areas, often providing important ecological habitats, are also missing in such basins. Moreover, the presence of a flood-tidal delta affects the dynamics of currents and the location of deep channels by controlling large scale flow patterns and, as such, has implications for navigation activities and man-made structures. It is thus of both practical and theoretical interest to understand what environmental conditions lead to the formation of either extensive channel networks or flood-tidal deltas. Here we use the numerical model presented in Chapter 2 to show how tidal range and initial bathymetry influence the long-term evolution of tidal basins and ultimately control the type of observed channel network that eventuates.

3.2 Numerical modelling

3.2.1 Model description

The numerical model used throughout this study simulates morphological change as a result of the interactions between hydrodynamics, sediment transport, and the evolving morphology. To summarise Chapter 2, we here follow the approach of coupling a comprehensive hydrodynamic model with the Engelund and Hansen (1967) formula. Hydrodynamic computations were performed using ELCOM (Estuary and Lake Computer Model; Hodges et al., 2000). This is a 3D-model based on the unsteady Reynolds-averaged Navier-Stokes equations. The equations are solved on a rectangular grid and ELCOM applies a z-coordinate system in the vertical dimension. We neglected influences of Coriolis force, density differences, wind, and waves.

Flow velocities, computed every hydrodynamic time-step, were used to obtain instantaneous sediment transport rates (Engelund and Hansen, 1967):

$$S_{flow} = \frac{0.05U^5}{\sqrt{g}C^3\Delta^2 D_{50}}, \quad (3.1)$$

where S_{flow} is the sediment transport flux, U is the magnitude of flow velocity, g is the gravitational acceleration, C is the Chézy coefficient, Δ is the relative density $(\rho_s-\rho_w)/\rho_w$, ρ_s is the sediment density, ρ_w is the water density, and D_{50} is the median grain size. Following the approach of Kirwan and Murray (2007), slope-driven sediment transport S_{slope} is incorporated in the model as:

$$S_{slope} = \alpha b, \quad (3.2)$$

where α is a dimensional constant (m^2/s) and b is the slope towards the neighboring grid cell. Here slope-driven sediment transport does not occur when b is below 0.01. Gradients in sediment transport rate drive bed level changes according to:

$$(1-\varepsilon_{por})\left(\frac{\partial z_b}{\partial t}\right)+\left(\frac{\partial S_x}{\partial x}+\frac{\partial S_y}{\partial y}\right)=0, \quad (3.3)$$

where ε_{por} is the bed porosity (kept fixed and equal to 0.4), S_x and S_y are the total sediment transport fluxes in the x- and y-direction, respectively. Bed level changes were integrated over one tidal cycle and then multiplied by a number of tidal cycles before morphological change feeds back into the hydrodynamic model. In this study we assumed that hydrodynamic conditions remained constant until bed level changes exceeded 10% of the local water depth at high tide. We adopted thus a varying morphodynamic time-step which allowed us to reduce numerical effort and facilitates the execution of long-term simulations.

3.2.2 Model set-up

Numerical simulations were undertaken using idealised initial bathymetries (Fig. 3.2). The initial topographies were composed of an offshore area, inlet, and basin and covered a total area of 17 × 17 km. Land regions, which form impermeable and non-erodible barriers, separated the offshore area from the tidal basin. The bed level in the tidal basin was disturbed by random perturbations of -1.5 to +1.5

cm. Initial bathymetric conditions were varied in terms of the initial depth of the tidal basin which amounted to 2, 4, and 6 m (Fig. 3.2). The model was forced with a semidiurnal tide. Simulations were performed with different combinations of initial depth and tidal range. The grid size amounted to 100 m in both x- and y-direction. The thickness of the horizontal layers was set to a uniform value of 40 cm. The hydrodynamic time-step was set to 2 minutes. The mean grain size diameter of the sediments was 0.12 mm and a value of 65 $m^{0.5}/s$ was used for the Chézy coefficient. Slope-driven sediment transport was calculated using $\alpha = 1.16 \times 10^{-5}$ m^2/s.

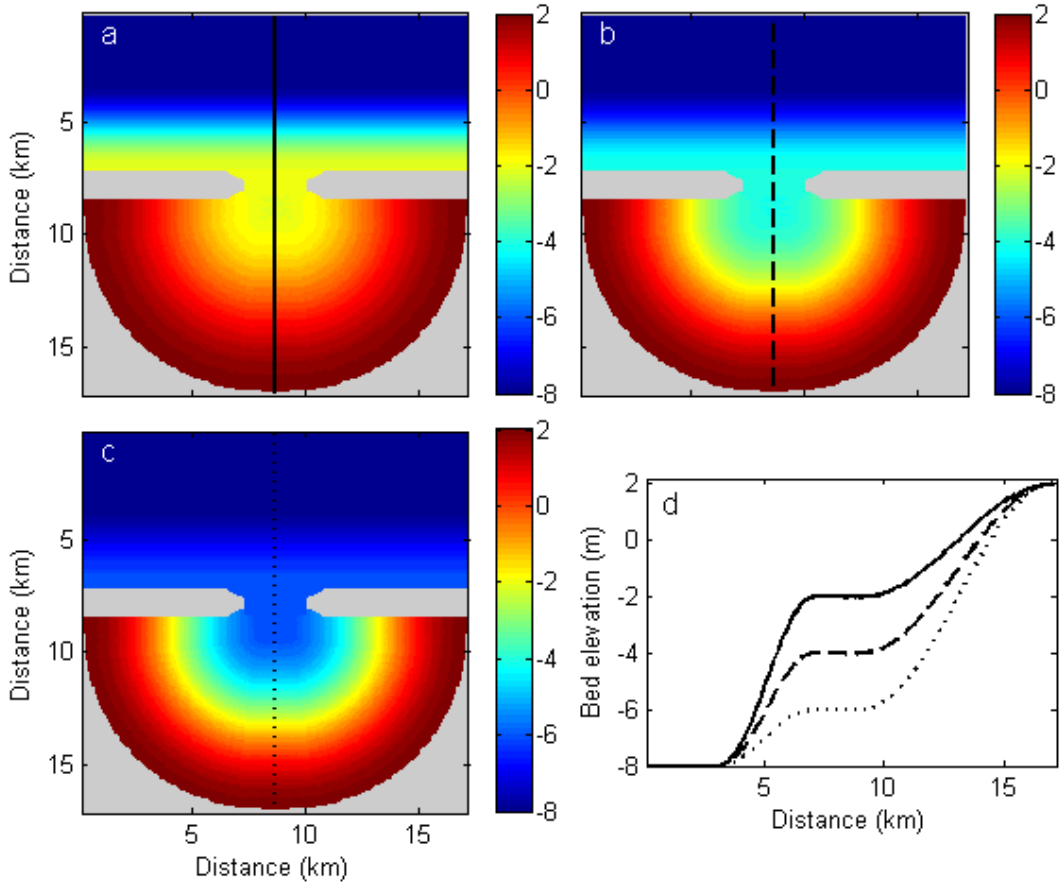

Figure 3.2. Plan view of the initial morphologies used throughout this study. The initial depth of the tidal basin amounted to (a) 2, (b) 4, and (c) 6 m. Grey areas represent land regions which form impermeable and non-erodible barriers. (d) Cross sections of the initial morphologies. Locations of the cross sections are indicated by the black lines in (a), (b), and (c).

3.3 Results

Model results indicate that morphodynamic interactions can cause channel initiation and give rise to pattern development. Figure 3.3 shows simulated morphologies after 1000 years for different combinations of the basin's initial depth and tidal range. A large variability in morphology can be observed, indicative of the crucial role that initial bathymetry and tidal conditions play in the large scale evolution of tidal embayments. The tidally-averaged residual flow pattern over the initial bathymetry with a depth of 2 m and for tidal range of 2 m is shown by Figure 3.4a. The flow in the basin consisted of two more or less symmetrical circulation cells with a strong landward directed flow in the centre of the basin and a strong seaward directed flow close to the barrier islands. The corresponding tidally-averaged residual sediment transport pattern (Fig. 3.5a) suggests a morphodynamically-active situation with large gradients in sediment transport rates. Large (of the order of meters in the vertical direction) bathymetric changes then also occurred within the first few years of morphological evolution (Fig. 3.6a). Two deep channels rapidly developed in the inlet (area between the barrier islands) of the tidal system. During ebb-tide, large volumes of sediment were transported towards the offshore area where decelerating flows caused sediment deposition. Consequently, a large ebb-tidal delta formed which, after 5 years, extended already about 3 km offshore. During the first 5 years of morphological evolution, the tidal basin experienced a net sediment import (solid red line in Fig. 3.7). The sediment transported into the basin originated from the inlet where accelerating flows caused scouring of the sediment (Fig. 3.5a). In the basin, small scale channels developed and intertidal areas emerged. During subsequent morphological evolution (Fig. 3.6b-d) the channels through the inlet continued to deepen and reached a maximum depth of about 10 m after 1000 years. The ebb-tidal delta increased in size and became highly asymmetrical. The tidal channels in the basin continued to branch; a process that ultimately resulted in the formation of a complex tidal channel network. The formation of channels and intertidal areas affects tidal asymmetry which drives tidally-averaged sediment transport (de Swart and Zimmerman, 2009). Large intertidal areas favour ebb-dominant sediment transport (Friedrichs and Aubrey, 1988; Dronkers, 2005). The development of the channel network was then also accompanied by a transition from sediment import to sediment export (Fig. 3.7). Large scale

bathymetric changes adapted the hypsometry of the tidal basin and the hypsometric curve after 1000 years (black stars in Fig. 3.8) resembles those of natural systems (see for example Fig. 4 in Marciano et al. (2005)). Furthermore, the overall flow pattern has changed after 1000 years and a strong reduction in both the tidally-averaged residual flow and sediment transport has occurred (Figs. 3.4b and 3.5b).

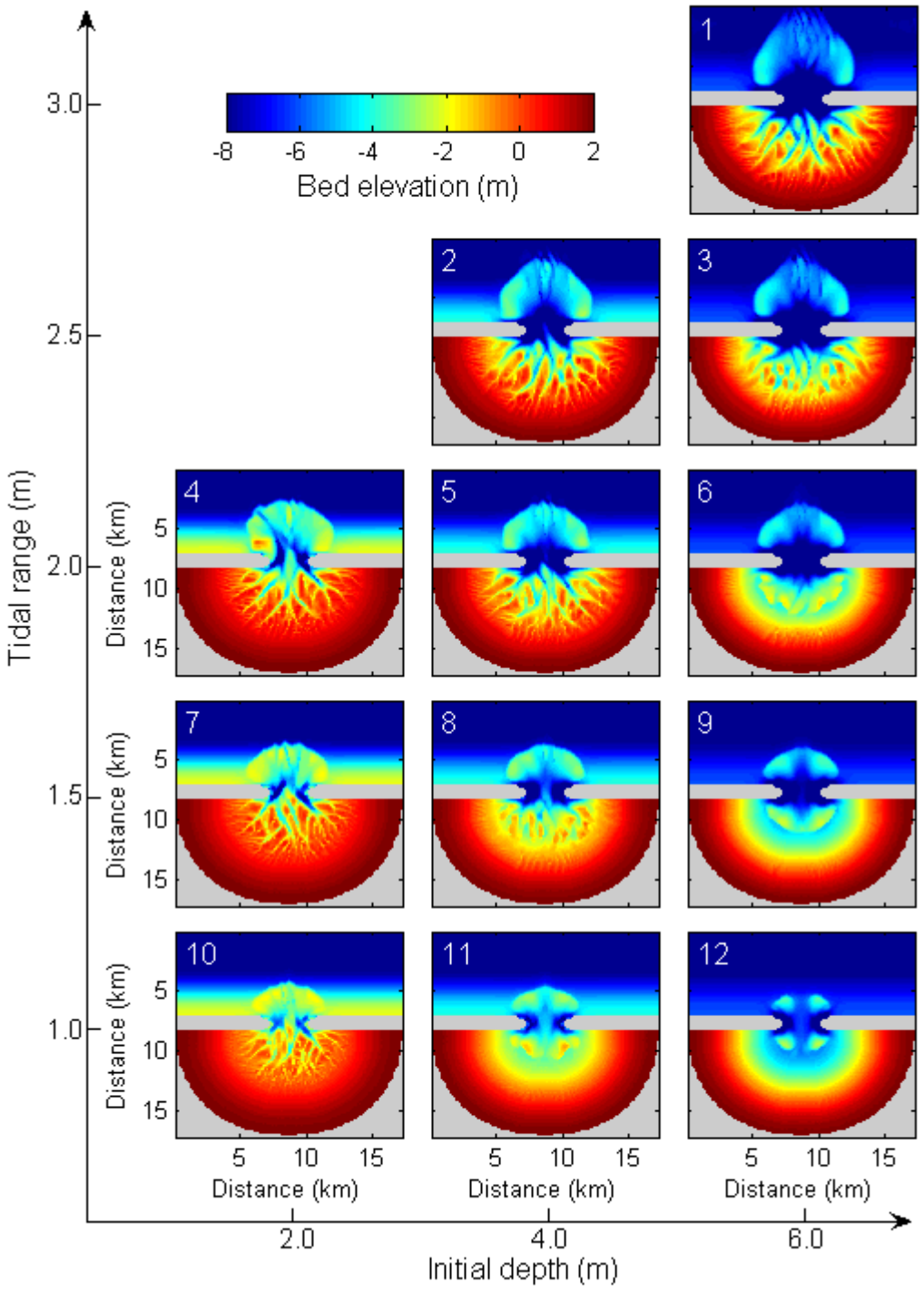

Figure 3.3. Simulated morphologies after 1000 years for different combinations of the basin's initial depth and tidal range.

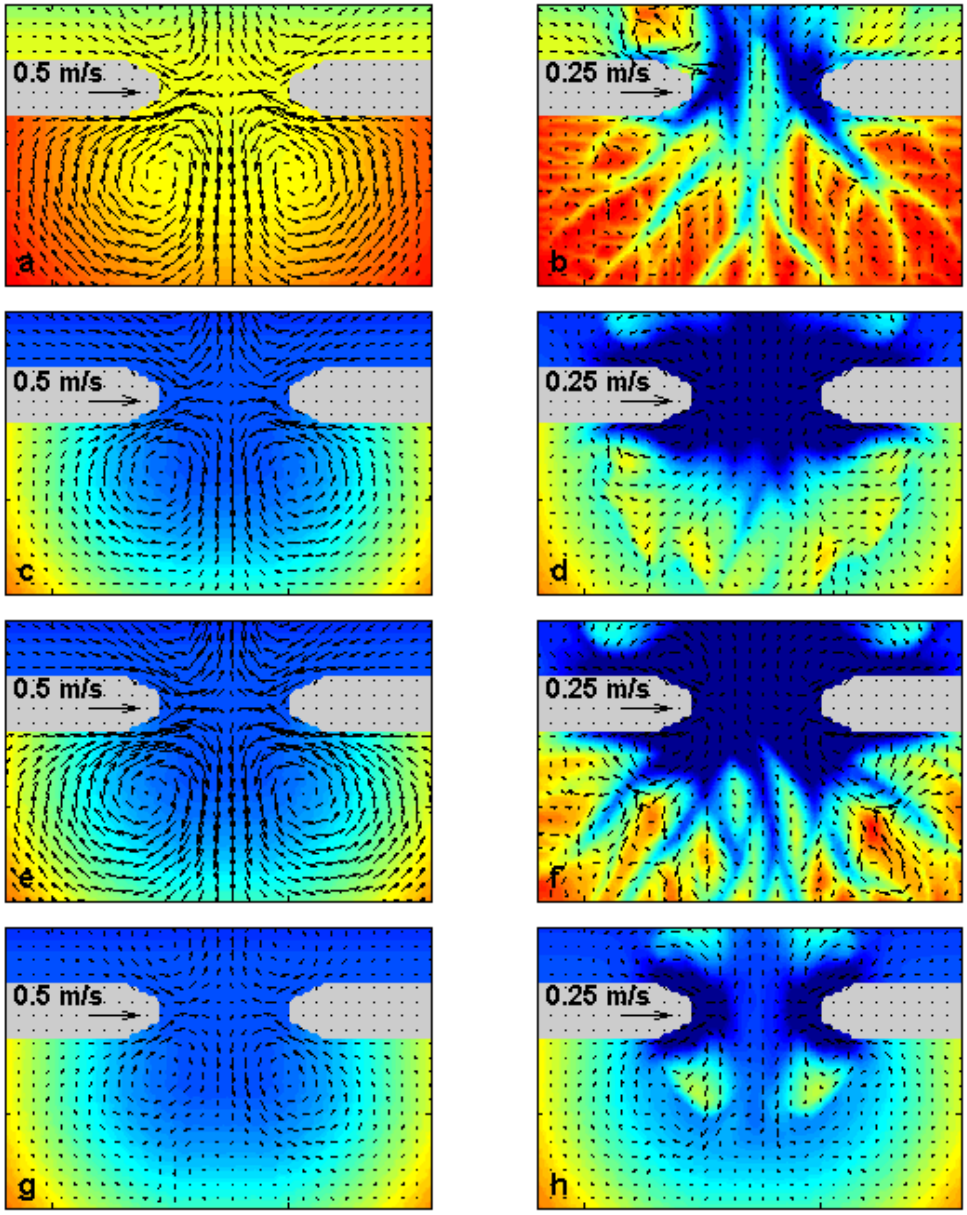

Figure 3.4. Tidally-averaged residual flow patterns over the initial morphologies for the area around the inlet when (a) the tidal range (TR) is 2 m and the basin's initial depth (ID) is 2 m, (c) TR=2 m and ID=6 m, (e) TR=3 m and ID=6 m, and (g) TR=1 m and ID=6 m. Subplots (b), (d), (f), and (h) show the corresponding flow patterns over the simulated morphologies after 1000 years.

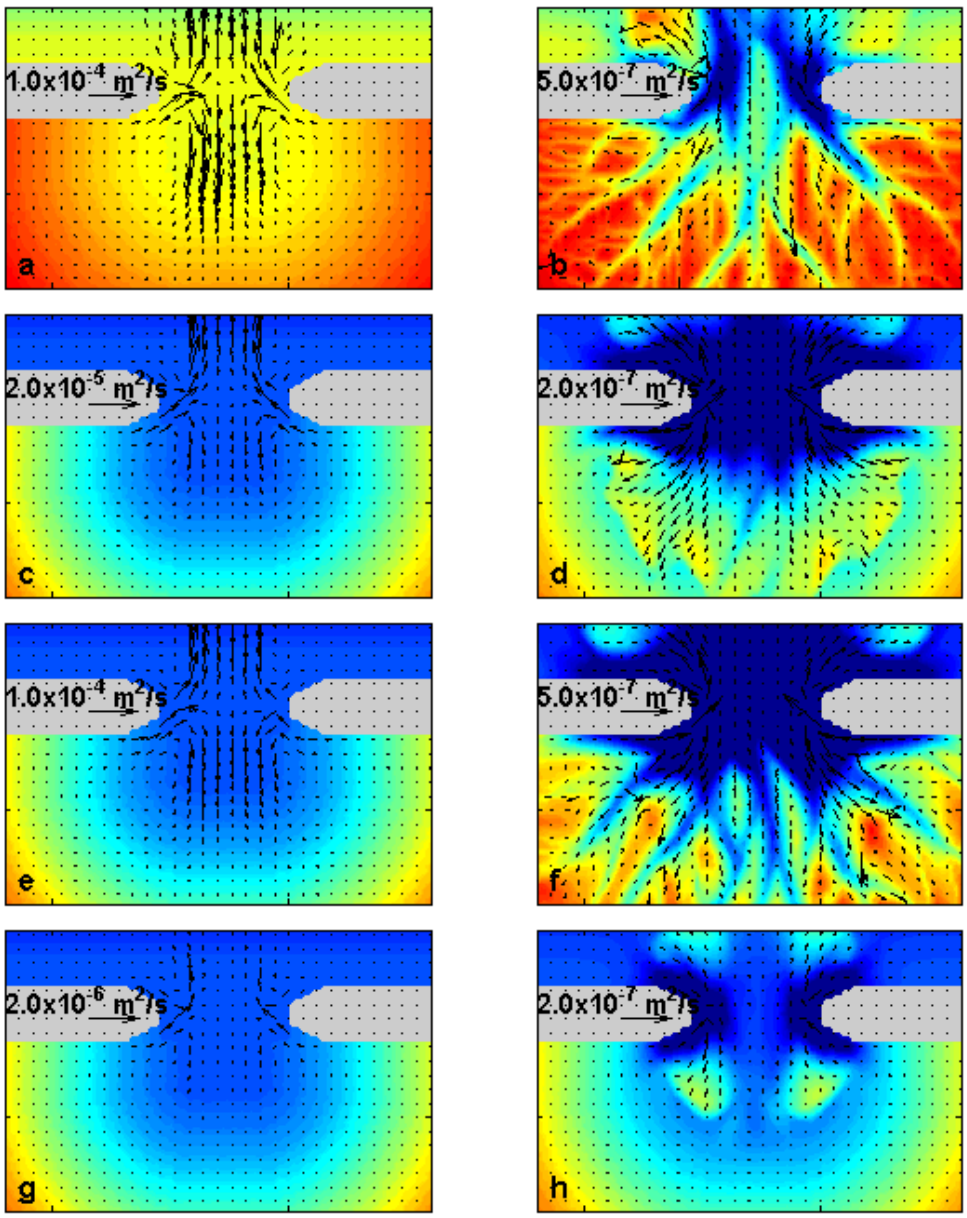

Figure 3.5. Tidally-averaged residual sediment transport patterns over the initial morphologies for the area around the inlet when (a) the tidal range (TR) is 2 m and the basin's initial depth (ID) is 2 m, (c) TR=2 m and ID=6 m, (e) TR=3 m and ID=6 m, and (g) TR=1 m and ID=6 m. Subplots (b), (d), (f), and (h) show the corresponding sediment transport patterns over the simulated morphologies after 1000 years.

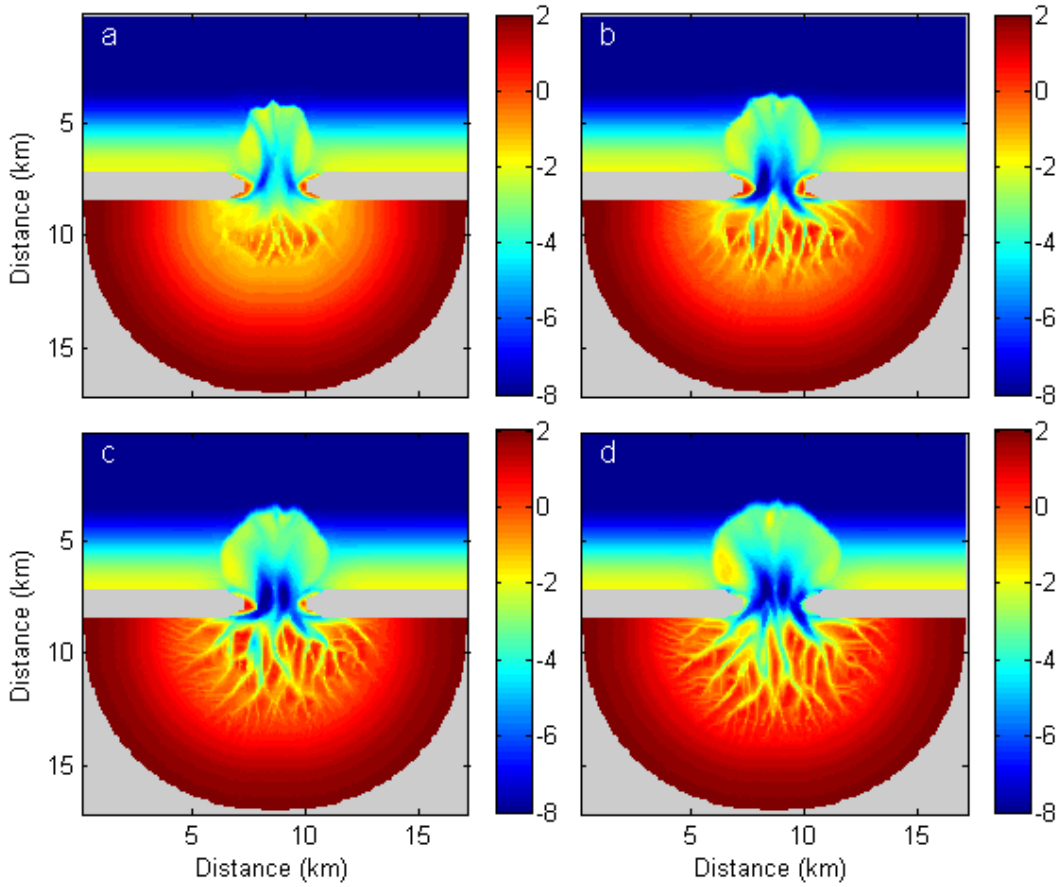

Figure 3.6. Simulation of morphological evolution for a tidal range of 2 m and an initial depth of the basin of 2 m. Morphologies after (a) 5, (b) 30, (c) 80, and (d) 250 years.

When the initial depth of the basin was increased to 6 m (while the tidal range was kept at 2 m; similar to the case previously discussed), the morphology of the tidal system evolves differently (Fig. 3.9). The scouring of the inlet and the import of sediment occurred at a slower pace (Fig. 3.5c and dotted red line in Fig. 3.7). Also, because of the large water depths, the imported sediment formed an unchannelized flood-tidal delta. Over time, the flood-tidal delta expanded landward and built up vertically and eventually became incised by channels. Simultaneously, small scale channels initiated in the shallow area in the upper part of the basin. After 1000 years the initial formation of channels can be detected. A net sediment import occurred continuously throughout this period of morphological evolution (Fig. 3.7) and the bed level in the inlet reached a maximum depth of more than 16 m. However, intertidal areas dissected by channels still had not formed after 1000 years. The hypsometric curve for the

basin after 1000 years (blue stars in Fig. 3.8) also indicates that the channel network and intertidal areas were still underdeveloped. The tidal basin continued to gain sediment and currents redistributed sediment from the deep areas to the shallow areas, ultimately resulting in the formation of intertidal areas and a complete tidal channel network (see Fig. 3.9d and the hypsometric curve represented by the grey triangles in Fig. 3.8).

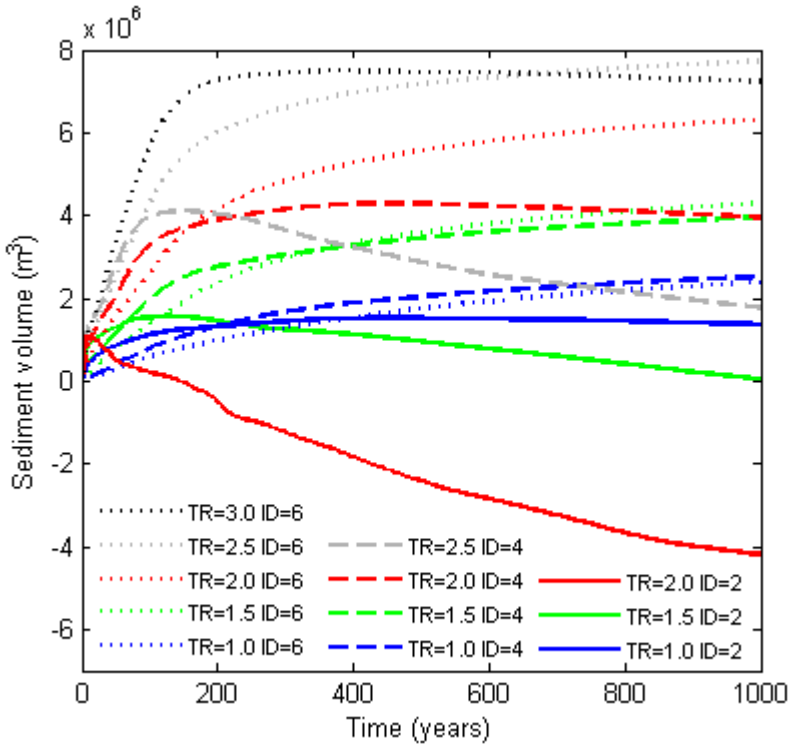

Figure 3.7. Changes in sediment volume within the basin. Import (positive numbers) of sediment to and export from (negative numbers) the tidal basin vary for different combinations of the basin's initial depth and tidal range.

In the case of a tidal basin with an initial depth of 6 m, an increase in tidal range to 3 m resulted in enhanced tidal flow (Fig. 3.4e) and flow acceleration through the inlet associated to the increase in tidal prism. The import of large volumes of sediment (more than 7 million m^3 after just 200 years; dotted black line in Fig. 3.7) occurred therefore at the beginning of morphological evolution. The flood-tidal delta, which formed in the basin, started to become channelized after 30 years. After 200 years, the volume of sediment present in the tidal basin remained relatively constant and the sediment was mainly redistributed within the basin such that a complete channel network had developed after 1000 years (Fig. 3.3).

The hypsometric curve (green stars in Fig. 3.8) is comparable to the curve obtained for the simulated morphology generated after 10000 years with an initial depth of 6 m and a tidal range of 2 m (grey triangles). Decreasing the tidal range to 1 m had the opposite effect. The ability of the currents to scour the sediment from the inlet and transport it into the basin was reduced (Fig. 3.5g and dotted blue line in Fig. 3.7) and there is no sign of channel initiation after 1000 years (Fig. 3.3). Large scale bathymetric changes and adaptation in the hypsometry were slowed down and the hypsometric curve associated to the simulated bathymetry after 10000 years (red triangles in Fig. 3.8) indicates that the channel network is still underdeveloped.

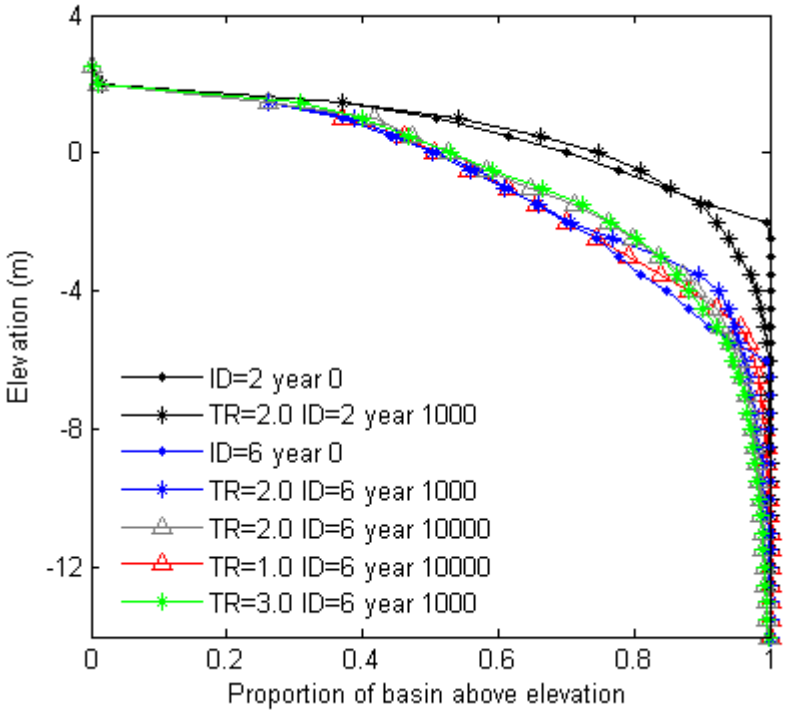

Figure 3.8. Hypsometric curves for some of the simulated morphologies.

For the simulations considered here, the mean residual flow reduced during morphological evolution (Fig. 3.4) and the magnitude of the mean residual sediment transport decreased by several orders of magnitude (Fig. 3.5). The rate at which sediment was transported to or from the basin also decreased over time (Fig. 3.7). The tidal basins thus reached a configuration for which morphological changes occurred at a slower pace. Dronkers (2005) defined equilibrium conditions in terms of the relative intertidal area and the amplitude-to-depth ratio

(a/h) and found that the two were positively related. We here calculated the relative intertidal area as the ratio of the intertidal surface area A_{int} and the total area inundated at high tide A_{tot}. The tidal amplitude a was taken at the offshore boundary and h was defined as the average water depth in the tidal basin relative to mean water level. Figure 3.10 shows how the relationship between A_{int}/A_{tot} and a/h changed over time and indicates that the morphology tends to evolve such that A_{int}/A_{tot} and a/h become equal. A_{int}/A_{tot} increases thus linearly with a/h and the ratio of the two approximates a value of 1 for relatively stable morphologies. For the simulations with a large amplitude-to-depth ratio, $(A_{int}/A_{tot})/(a/h)$ is initially smaller than 1 (Fig. 3.10a). $(A_{int}/A_{tot})/(a/h)$ increases during morphological evolution because of the deepening of channels and the development of intertidal areas. Basins with a large relative intertidal area have a tendency towards ebb dominance (Dronkers, 2005) and it is therefore interesting to note that the simulated basins which are exporting sediment after 1000 years are all associated with a ratio $(A_{int}/A_{tot})/(a/h)$ above 1 (the numbers 1, 2, 4, 5, 7 in Figure 3.10c).

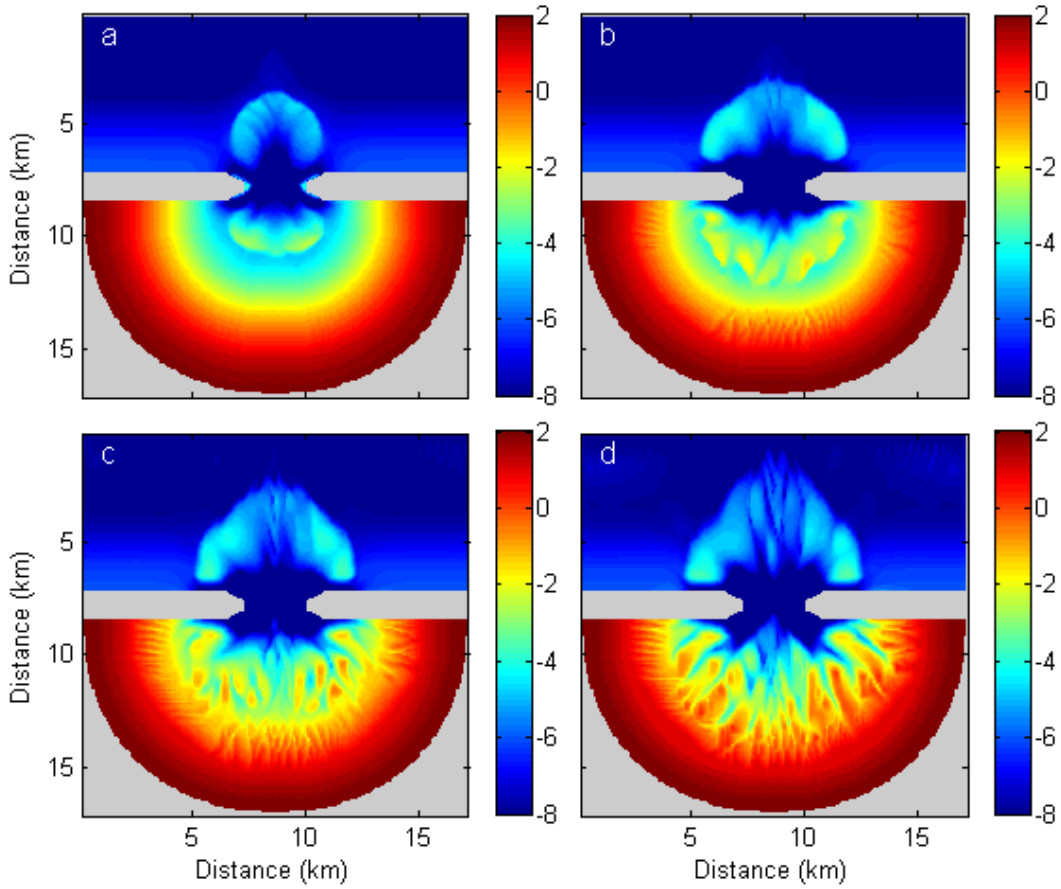

Figure 3.9. Simulation of morphological evolution for a tidal range of 2 m and an initial depth of the basin of 6 m. Morphologies after (a) 60, (b) 1000, (c) 3000, and (d) 10000 years.

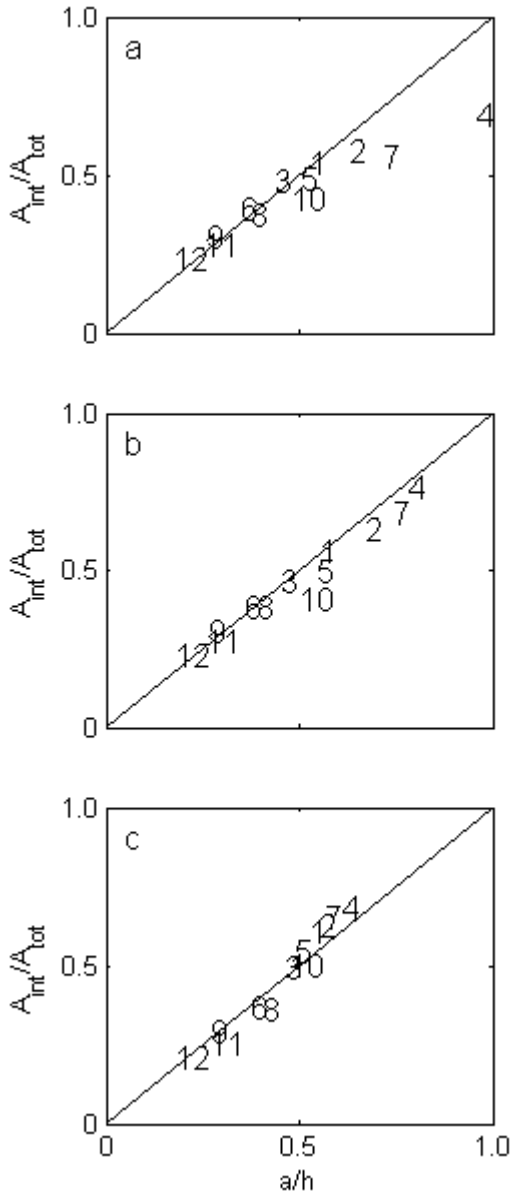

Figure 3.10. Relation between (A_{int}/A_{tot}) and (a/h) for the morphologies after (a) 0, (b) 100, and (c) 1000 years. Numbers correspond to the numbering in Fig. 3.3.

3.4 Discussion and conclusions

A number of simplifications concerning the description of hydrodynamic and sediment transport processes have been made throughout the development of the model applied in the present study. The flow is solely tidally-driven (no waves, wind, or density-driven effects) and spring-neap effects have been ignored. Furthermore, a simple sediment transport formulation (although commonly applied) which includes a single grain size diameter and only allows modeling of non-cohesive sediment has been used. We included only a minimum number of

processes so that model results are as transparent as possible and with the purpose of gaining maximum insight into the role of initial bathymetry and tidal range on the long-term evolution of tidal embayments. A shallow initial basin and a large tidal range allow the rapid formation of channels and intertidal areas. When the basin is deeper, large tidal range conditions facilitate the transport of large volumes of sediment into the basin. A flood-tidal delta forms which becomes channelized and a complete channel network eventually develops. However, when the tidal basin is deep and the tidal range small, large scale bathymetric changes are slowed down and an underdeveloped channel network remains present over long time scales.

Both modelling (Schuttelaars and de Swart, 1999) and experimental (Stefanon et al., 2010) studies have shown that flow concentration and acceleration are key factors in the formation and expansion of tidal channels. Schuttelaars and de Swart (1999) demonstrated that bottom friction causes the velocity to become smaller above shoals and larger in the channels, causing sediment to be transported from the channels towards the shoals giving rise to a positive feedback mechanism. Our simulations indicate that when bottom friction is not affecting the flow in deep tidal basins, the positive feedback mechanism is not effective and channels do not develop. Alternatively, a flood-tidal delta forms which grows and becomes shallower over time until the effects of bottom friction start to influence flow velocities and determine preferential flow paths, ultimately causing channel initiation.

Finally, changes in the basin's initial depth and tidal range affect the morphological evolution in their own specific way. For the simulations performed here, an increase in the initial depth of the basin does not only slow down the morphological evolution, but also affects the hypsometry of the evolving tidal basin. A decrease in tidal range also delays the formation of channels and intertidal areas, but has got a smaller effect on the final hypsometry of the basin. Despite different hypsometric characteristics the basins all reach a state of less morphodynamic activity. A further decrease in tidal range would ultimately cease the formation of a well-developed channel network and extensive intertidal areas.

Chapter 4

It is not a bathtub: the response of tidal embayments to sea level rise

4.1 Introduction

Global sea level rise is one of the major negative outcomes of a shifting climate, which impacts on both natural and human-modified ecosystems by causing sandy shoreline retreat (Pilkey and Cooper, 2004), the loss of wetland areas in deltaic systems (Blum and Roberts, 2009) and, most importantly, changes to fragile systems such as estuaries and tidal embayments. Although tidal environments are amongst the most productive ecosystems in the world (Mitsch and Gosselink, 2007), they also represent one of the most vulnerable environments where valuable habitats can become threatened because of sea level rise (IPCC, 2002). A major focus of climate adaptation studies is to predict the future morphology of tidal systems and to evaluate potential losses in habitat area.

The impacts of sea level rise on estuaries and tidal embayments are commonly explored applying the so-called “bathtub” approach: the sea level rises instantaneously and the bottom surface (the “seabed”) is not allowed to change (Jelgersma, 1994). The bathtub approach neglects the temporal morphological evolution of the system and uses present-day topographic data and projected water levels to provide insight into the effects of sea level rise. This approach has been widely-used and leads to predictions of dramatic losses in habitable land, ecosystem services, and endangered species (Milliman et al., 1989; Daniels et al., 1993; Najjar et al., 2000; Titus and Richman, 2001; Gesch, 2009). Slightly more sophisticated models have also been developed and include local accretion and/or subsidence rates to predict changes in habitat types as a result of changes in inundation or salinity. Specific case studies suggest that sea level rise will have severe consequences, ranging from population declines (e.g. shorebirds foraging on intertidal areas (Galbraith et al., 2002)) to large scale habitat destruction (e.g. salt marshes (Craft et al., 2009)).

Although accounting for accretion rates (often using historical data (e.g. French, 2008)) is an improvement compared to the original bathtub approach, flow-sediment-morphology interactions (the so-called morphodynamic feedback loop, Fig. 1.1a) remain essentially neglected. Our study indicates that a full understanding of the response of tidal embayments to sea level rise can only be achieved by focussing on such feedbacks. Morphodynamic models simulate bathymetric change as the result of the continuous interaction between hydrodynamics, sediment dynamics, and bed level change. These models, therefore, have the ability to account for dynamic sedimentary processes and give rise to the positive and negative feedback mechanisms which occur in natural systems. Numerical models based on morphodynamic principles have already proven to be capable of explaining the formation of various landform patterns (Coco and Murray, 2007). Over recent years, modelling techniques have been developed that allow also for long-term morphodynamic simulations of coastal systems (Roelvink, 2006) and have been used to model the formation of tidal channel networks (Marciano et al., 2005). Here we use this type of model, introduced in Chapter 2, to quantify morphological change in tidal embayments during sea level rise.

4.2 Methods

The numerical model used throughout this study simulates morphological change as a result of the interactions between hydrodynamics, sediment transport, and bed elevation change. A detailed overview of model development can be found in Chapter 2. To summarise, fluid flow is simulated using ELCOM (Estuary and Lake Computer Model; Hodges et al., 2000). This model applies a rectangular grid and a z-coordinate system in the vertical dimension. Influences of Coriolis force, density differences, wind, and waves are not included in the model.

Every hydrodynamic time-step, the flow velocities were used to obtain instantaneous sediment transport rates. These were calculated using the Engelund and Hansen (1967) formula:

$$S_{flow} = \frac{0.05U^5}{\sqrt{g}C^3\Delta^2 D_{50}}, \quad (4.1)$$

where S_{flow} is the sediment transport flux, U is the magnitude of flow velocity, g is the gravitational acceleration, C is the Chézy coefficient, Δ is the relative density $(\rho_s-\rho_w)/\rho_w$, ρ_s is the sediment density, ρ_w is the water density, and D_{50} is the median grain size. The approach given in Kirwan and Murray (2007) was used to provide a slope-driven sediment transport S_{slope}:

$$S_{slope} = \alpha b, \quad (4.2)$$

where α is a dimensional constant and b is the slope towards the neighboring grid cell. Here slope-driven sediment transport only occurs when b exceeds 0.01. The bed level changes due to gradients in the sediment transport rate. Bed level evolution was computed following:

$$(1-\varepsilon_{por})\left(\frac{\partial z_b}{\partial t}\right)+\left(\frac{\partial S_x}{\partial x}+\frac{\partial S_y}{\partial y}\right)=0, \quad (4.3)$$

where ε_{por} is the bed porosity (kept fixed and equal to 0.4), S_x and S_y are the total sediment transport fluxes in the x- and y-direction, respectively. Bed level changes were integrated over one tidal cycle and then extrapolated over a number of tidal cycles before hydrodynamic conditions were updated. In this study we adopted a varying morphodynamic time-step and assumed that hydrodynamic conditions remained constant until significant changes in the morphology (larger than 10% of the local water depth at high tide) had occurred.

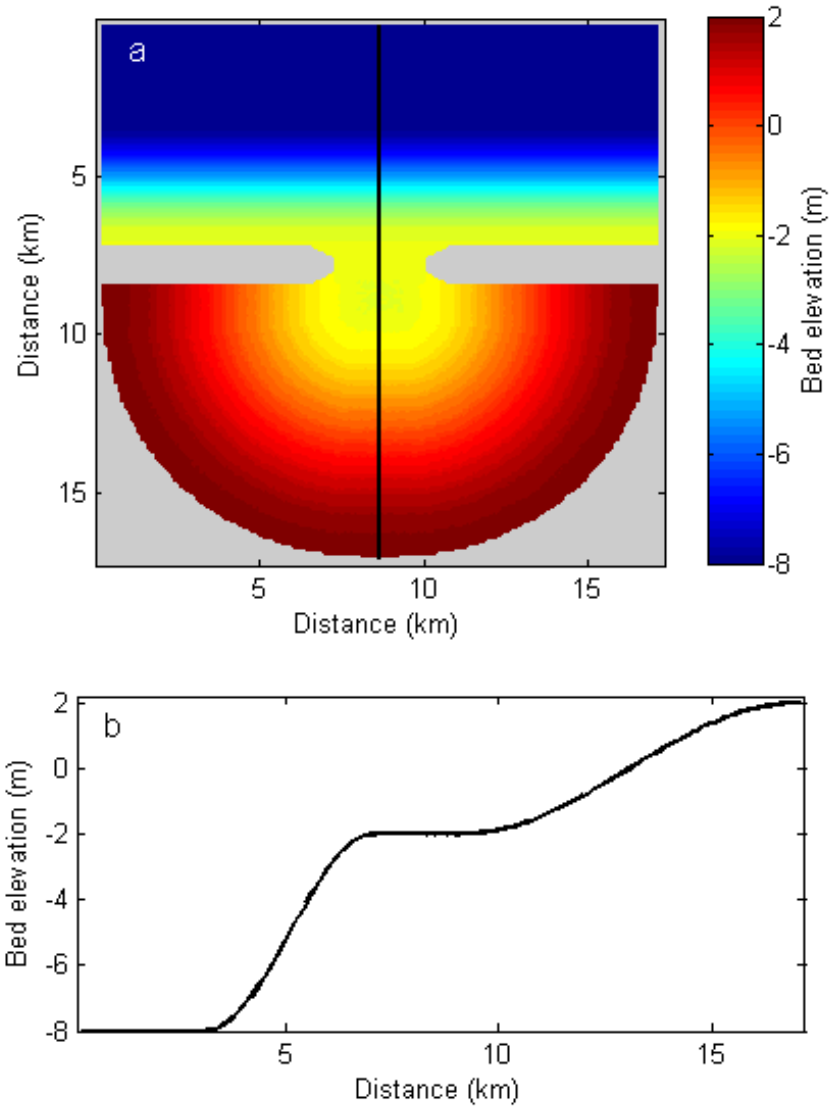

Figure 4.1. Initial morphology used throughout this study. (a) Plan view of the morphology consisting of an offshore area, inlet, and tidal basin. Grey areas represent land regions which form impermeable and non-erodible barriers. (b) Cross section of the initial morphology. Location of the cross section is indicated by the black line in (a).

Numerical simulations were undertaken using an idealised initial bathymetry. The model domain covered an area of 17 × 17 km and was composed of an offshore area, inlet, and basin (Fig. 4.1). This initial morphology was also used as a starting case in Chapter 2 (Fig. 2.1) and 3 (Fig. 3.2a). The offshore area was separated from the tidal basin by the presence of land regions. These regions formed impermeable and non-erodible barriers. Random perturbations of -1.5 to +1.5 cm were added to the bed level in the tidal basin. A semidiurnal tide was used to force

the model. A grid size of 100 m in both x- and y-direction was applied. The thickness of the horizontal layers was kept at a uniform value of 40 cm. The hydrodynamic time-step was set to 2 minutes. The sediments had a mean grain size diameter of 0.12 mm and a value of 65 $m^{0.5}/s$ has been used for the Chézy coefficient. Slope-driven sediment transport was calculated using $\alpha = 1.16 \times 10^{-5}$ m^2/s.

4.3 Results

Over long time scales, morphodynamic interactions result in the emergence of fully developed tidal channel networks. Figure 4.2a shows a simulated morphology after 400 years with a tidal range of 1.5 m. More "snapshots" of the morphological evolution can be found in Figure 4.3. This bathymetry has then been used to study the impact of an increase in sea level at a rate of 5.6 mm/year (within the range of sea level rise estimates (IPCC, 2007)) for 200 years. Applying the bathtub approach, which corresponds to raising the mean water level, provides a straightforward prediction of future bed elevations. Figure 4.2b shows the expected bathymetry when this approach is being followed. Intertidal areas which were present before sea level rise are expected to become inundated more regularly or will drown completely. As mentioned earlier, the bathtub approach ignores morphological change driven by currents redistributing the sediment and modifying the landscape while the sea level is rising.

To explore the relevance of morphological change we performed numerical simulations under a gradual rise in sea level (Fig. 4.2c). Drastic differences can be observed when model results are compared with the bathymetry predicted using the bathtub approach (Fig. 4.2b), indicative of the importance of erosion and deposition processes occurring while the sea level rises. The ebb-tidal delta has built up vertically and expanded a few hundred meters seaward. The increase in tidal prism results in enhanced deepening of the channels through the inlet. Tidal channels in the basin migrate and expand landward, alternating the topography of the area which was previously dry (compare black lines in Figs. 4.2b and c). While the sea level is rising, intertidal areas adjust toward sustaining their relative elevation. Nonetheless, the size, shape, and location of the intertidal areas have changed. Even when sea level rise stops, the response of the morphology to the

change in hydrodynamic regime continues and intertidal areas reorganize themselves further (Fig. 4.4). The approach of adjusting the present-day bathymetry by taking into account historical rates of morphological change (Fig. 4.2d) is also not capable of capturing the dynamics related to the expansion of the channel network and the reorganization of intertidal areas. In essence, it is the morphodynamic loop that shapes the evolution of tidal systems.

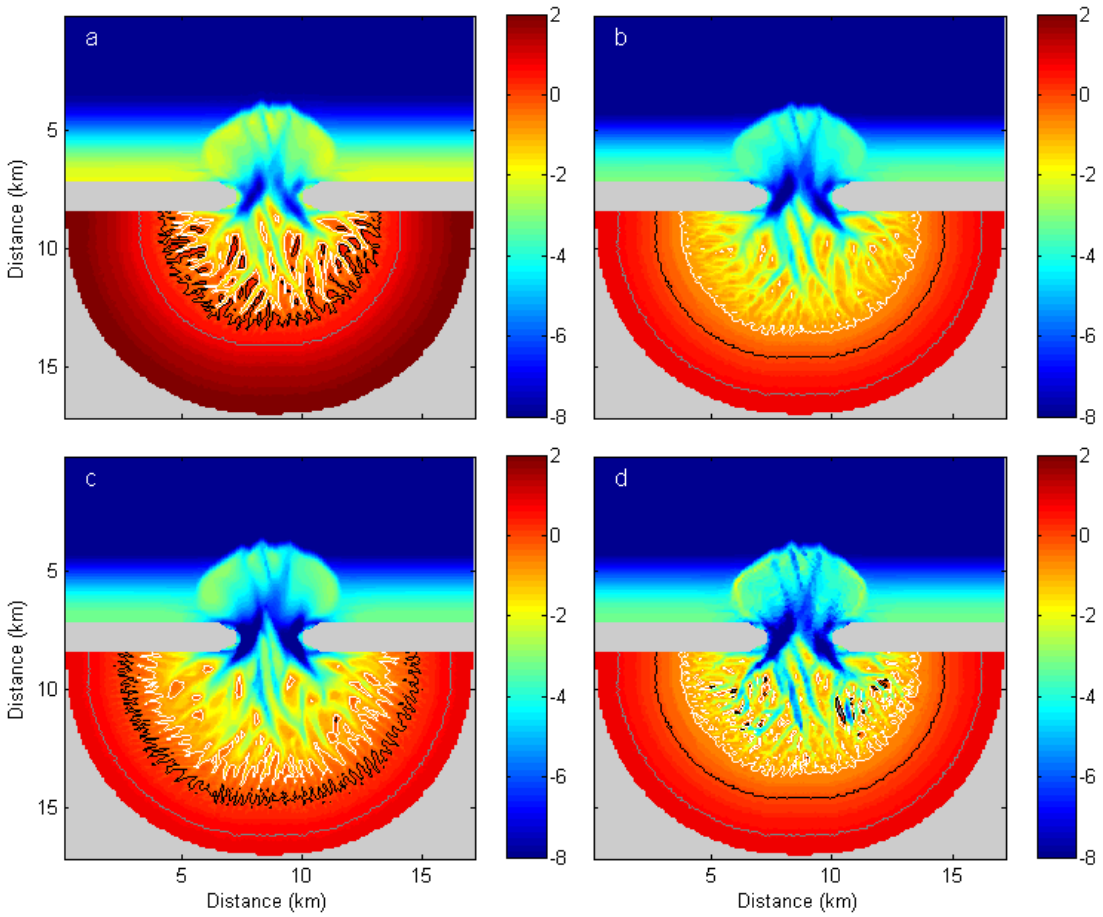

Figure 4.2. Predicting the morphology of a tidal embayment facing sea level rise at a rate of 5.6 mm/year for 200 years. (a) Steady-state (here defined when the root-mean-square of the bed level changes between successive years computed over all grid cells in the basin is below 2 cm) morphology generated after 400 years of bathymetric change starting from an unchannelized basin (Fig. 4.1). Tidal range is 1.5 m. (b) Expected bed elevations applying the bathtub approach. (c) Simulated bathymetry when morphology evolves during sea level rise. (d) Expected bed elevations when historical rates of morphological change (evaluated over the last 100 years) are extrapolated into the future. White, black, and grey lines represent -0.75 (low tide), 0 (mid tide), and 0.75 (high tide) m contour lines, respectively. Grey areas are land regions.

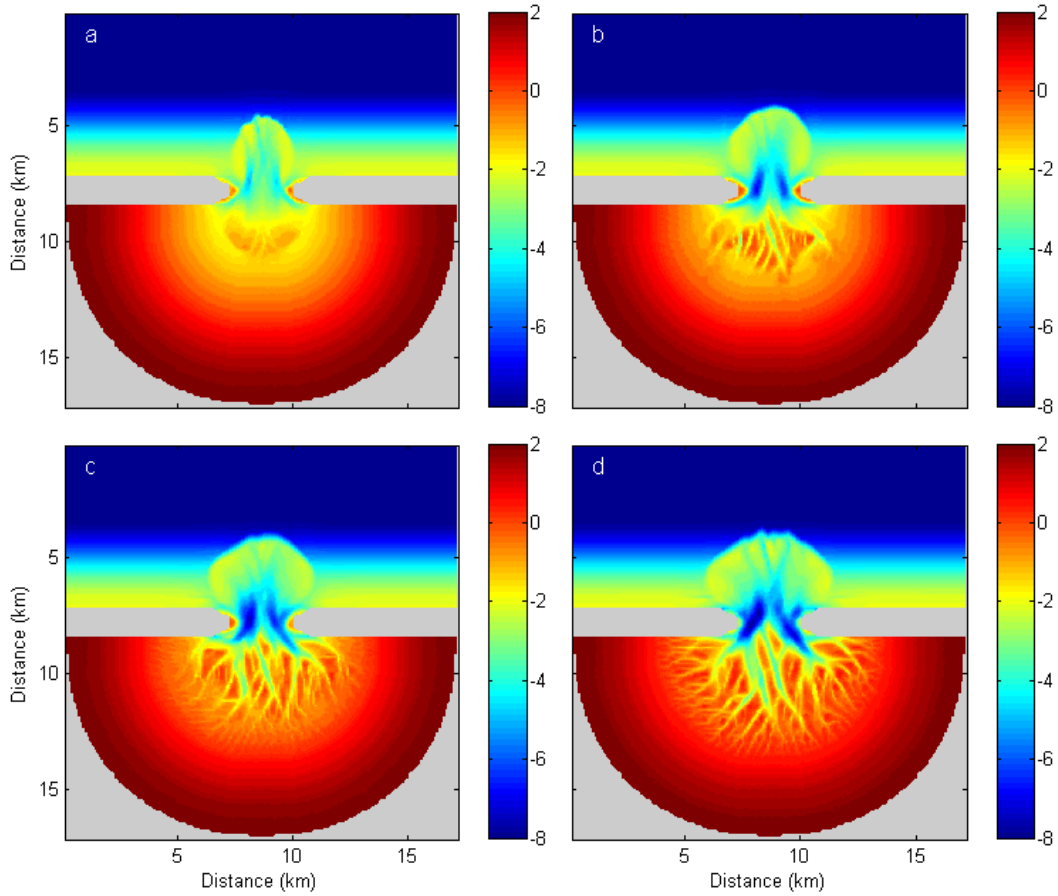

Figure 4.3. Simulation of tidal channel network formation for a tidal range of 1.5 m. Morphologies after (a) 5, (b) 30, (c) 100, and (d) 400 years.

The complex mechanisms controlling sea level changes are not well understood and a wide range of sea level rise scenarios are possible (IPCC, 2007; Rahmstorf, 2007; Pfeffer et al., 2008). To test the sensitivity of morphological change to the rate at which sea level rise occurs, simulations have been performed for which the rate has been changed by a factor of 2. Conditions used to force the model at the seaward boundary were also varied to explore the effect of tidal range. Morphological change was quantified by computing the root-mean-square of the deviation in bed elevation between the non-evolving (Fig. 4.2b) and evolving (Fig. 4.2c) morphologies. Figure 4.5a shows, as a function of time, the rms-deviation computed over all the grid cells in the basin for different rates of sea level rise and tidal ranges. Changes in the topography of the basin increase over time. An increase in morphological change is observed for larger tidal ranges which are associated, for the present geometry of the basin, with larger velocity fields and so with larger gradients in sediment transport. The morphological

change associated with a constant mean water level (see the black lines in Fig. 4.5a) indicates that these simulated tidal environments have not reached a steady-state characterized by no gradients in sediment transport throughout the entire domain. The rms-deviation was also calculated for different segments of the basin by splitting the bathymetry prior to sea level rise (Fig. 4.2a) into subtidal, intertidal, and supratidal areas (Fig. 4.5b-d). Largest bathymetric changes occur in the subtidal and intertidal regions while the supratidal region displays smaller changes (by an order of magnitude).

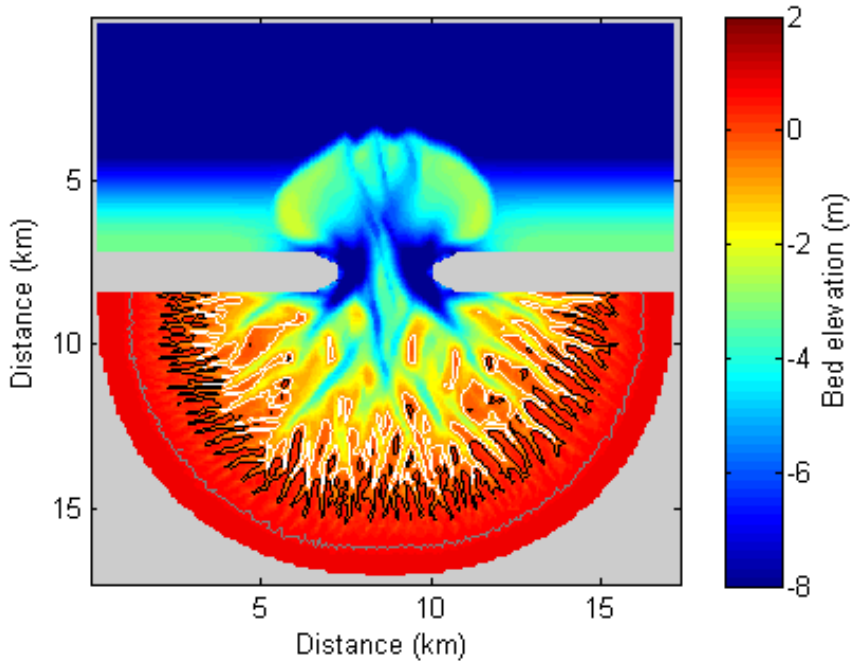

Figure 4.4. Simulated morphology 200 years after sea level rise has stopped. The morphology is not in a steady-state at the end of sea level rise. Tidal channels keep on expanding landward and intertidal areas continue to reorganize themselves. White, black, and grey lines represent -0.75 (low tide), 0 (mid tide), and 0.75 (high tide) m contour lines, respectively.

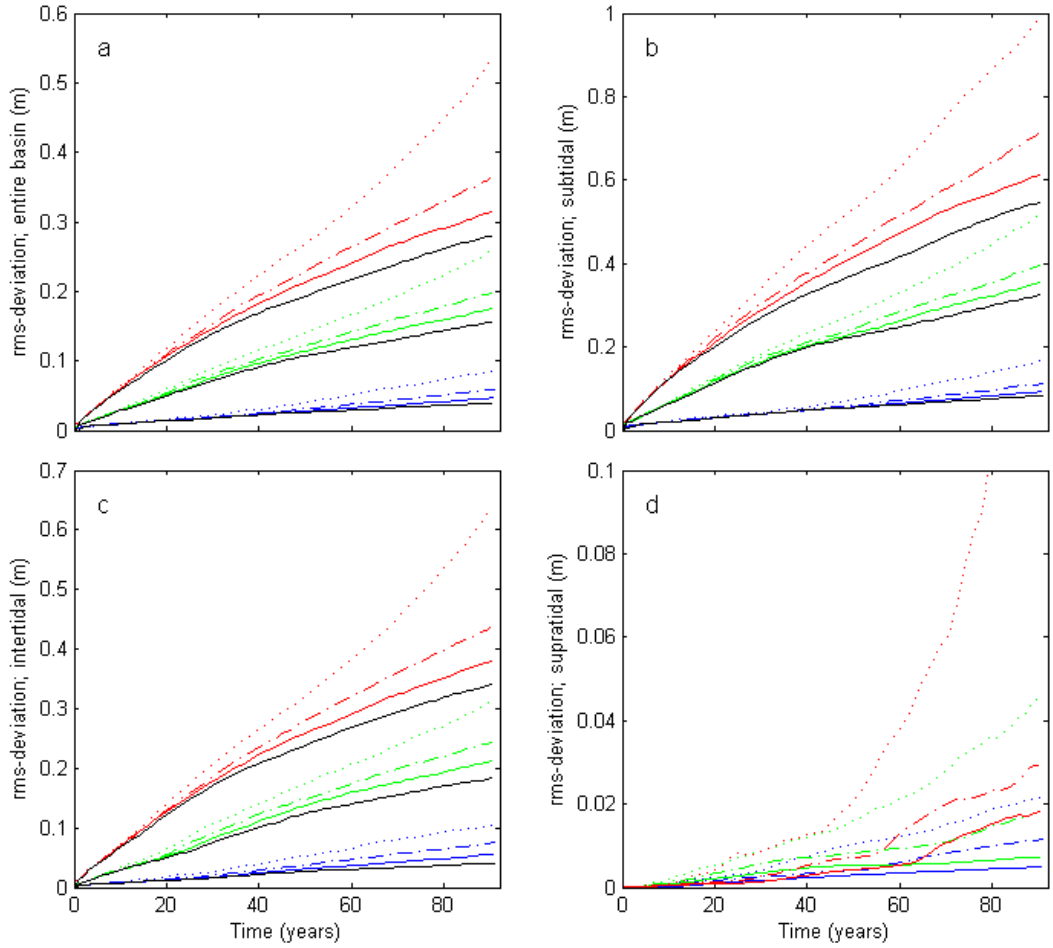

Figure 4.5. Quantification of morphological change during sea level rise. The subplots show the root-mean-square of the deviation in bed elevation between non-evolving and evolving morphologies versus time. The rms-deviation was calculated for (a) the entire basin and for different segments of the basin by splitting the bathymetry prior to sea level rise into (b) subtidal, (c) intertidal, and (d) supratidal areas. Blue, green, and red represent a tidal range of 1, 1.5, and 2 m, respectively. For all the simulations, morphologies were in a steady-state when sea level started to rise. Sea level rise rates amount to 2.8 (solid line), 5.6 (dashed-dotted line), and 11.2 (dotted line) mm/year. Black lines represent situations without sea level rise.

To quantify responses in the channel network configuration, we used a technique based on the work by Passalacqua et al. (2010) to extract the number and drainage width of channels at specific distances from the coastal inlet. Because of the branching character of the network, the number of channels at a specific distance from the coastal inlet initially increases in the landward direction (Fig. 4.6a). The

abrupt decline in channel occurrence above mid-tide is the results of tidal channels expanding landward at different rates. As mentioned before, sea level rise causes expansion of the channel network because of headward erosion of channels. Simultaneously, sea level rise also affects the existing channels because larger water depths correspond to larger and more widely-spaced channels (Marciano et al., 2005). When the channel network has adjusted to the change in water depths after sea level rise has stopped (green stars in Fig. 4.6), a decrease in the number of channels (Fig. 4.6a) and an associated increase in channel drainage width (Fig. 4.6b) can be observed in the area up to ~5 km from the inlet. Remarkably, the channel network has adjusted to the changing hydrodynamic conditions and reorganized itself such that the channel drainage width at mid tide both before and after sea level rise is similar (Fig. 4.6b).

Asymmetry between the flood and ebb tidal currents is an important physical mechanism that affects long-term morphological evolution by driving tidally-averaged sediment transport (de Swart and Zimmerman, 2009). The tidal asymmetry is directly related to the geometric characteristics of the tidal basin and basins with large intertidal areas favour ebb-dominant sediment transport (Dronkers, 2005). A rise in sea level and the corresponding change in mean water depth could therefore alter the tidal asymmetry. The simulated tidal basins are in a state of ebb-dominance once a well-developed channel network has formed. For a tidal range of 1 m, drowning of intertidal areas due to sea level rise initially decreases the volume of sediment which is transported from the basin into the inlet and offshore area (Fig. 4.7). Intertidal areas quickly become subtidal at high rates of sea level rise and a transition from exporting sediment to importing sediment occurs (Fig. 4.7), partially offsetting sea level rise. For the simulations herein presented, intertidal areas dissected by channels remain present when the tidal range is 1.5 (Fig. 4.2c) or 2 m. Consequently, these basins with a larger tidal range continue to export sediment.

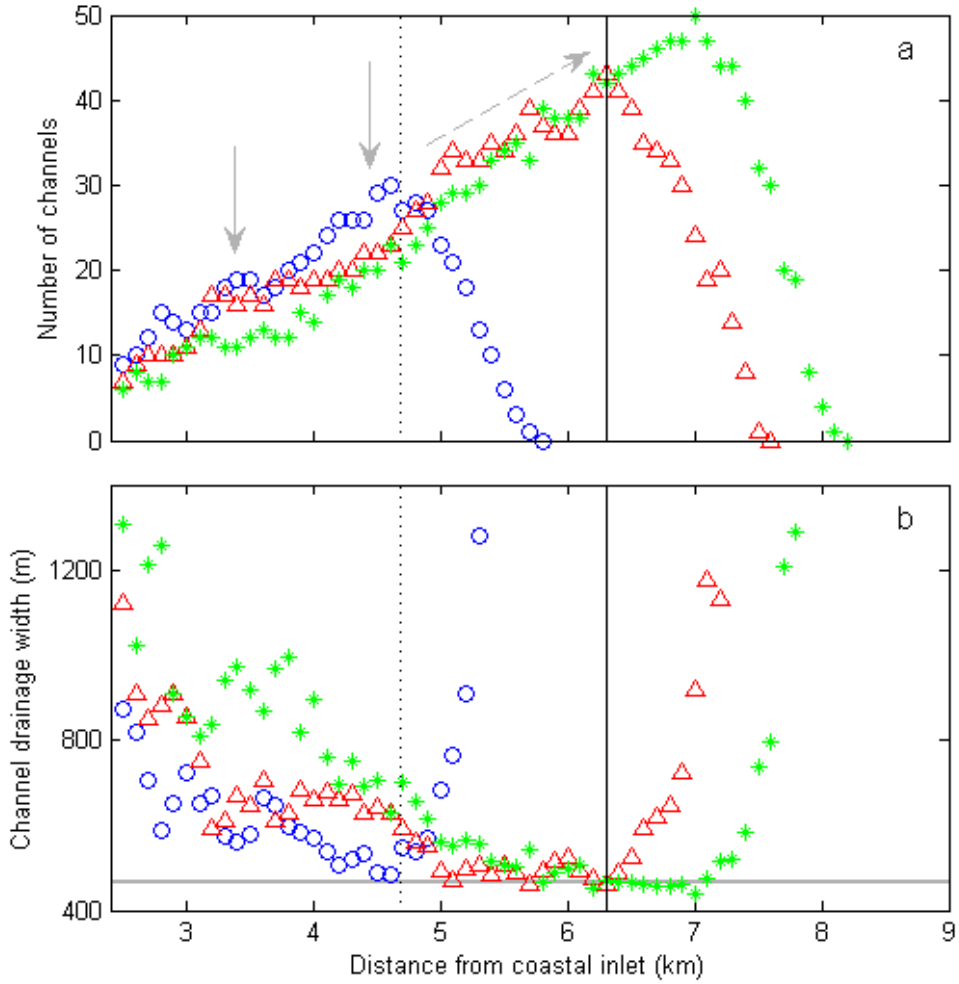

Figure 4.6. Change in channel network configuration as a result of sea level rise. (a) Number of channels and (b) channel drainage width versus distance from the coastal inlet prior to (blue circles) and immediately after (red triangles) sea level rise for a simulation carried out with a tidal range of 1.5 m and a sea level rise rate of 5.6 mm/year (the simulation presented in Figure 4.2). Channel network configuration has further adjusted 200 years after (green stars) sea level rise has stopped (channel network of the morphology presented in Fig. 4.4). Vertical dotted and solid lines approximate the position of the water level at mid tide before and after sea level rise, respectively. The solid arrows in (a) point out the decrease in the number of channels due to increasing water depths. The dashed arrow points out the increase in the number of channels due to the landward expansion of channels. The horizontal grey line in (b) shows that the channel network configuration has adjusted such that the channel drainage width at mid tide both before and after sea level rise is similar.

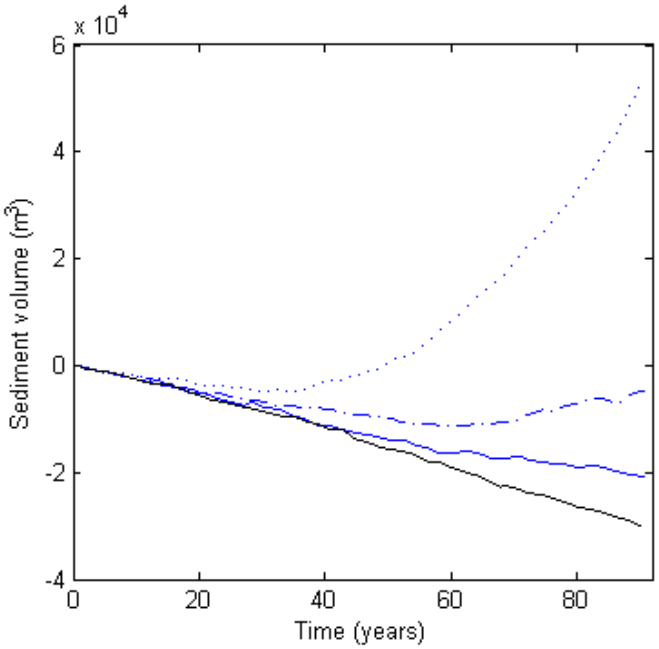

Figure 4.7. Cumulative volume of sediment transported through the tidal inlet for a tidal range of 1 m. Import (positive numbers) of sediment to and export from (negative numbers) the tidal basin vary when sea level rise rate amounts to 2.8 (solid line), 5.6 (dashed-dotted line), or 11.2 (dotted line) mm/year. Black line represent situation without sea level rise.

4.4 Discussion and conclusions

A number of simplifications have been made throughout the development of the model. The flow is solely tidally-driven (no waves, wind, or density-driven effects) and spring-neap effects have been ignored. Furthermore, a simple, although common sediment transport formulation (the formula includes a single grain size diameter and only allows modelling of non-cohesive sediment) has been used. Because of these simplifications the numerical model is not intended to be used here to make accurate quantitative predictions of the future evolution of a specific natural system, but it can be used to explore possible responses of tidal basins to an increase in sea level. Model results indicate that intertidal areas reorganize themselves while channel networks shift landward during sea level rise and even a transition from exporting to importing sediment can potentially occur, drastically changing the characteristics of the tidal basin. Different algorithms for sediment transport and hydrodynamics might result in different results from a quantitative perspective but the qualitative outcome of these simulations will not

change: it is the morphodynamic feedback loop that shapes the morphology of tidal environments.

With 37% of the world's population living within 100 km distance of the coast (Cohen et al., 1997), predicting the future state of tidal environments is one of the main challenges in climate impact research. Modelling of the dynamic and complex morphodynamic interactions shows that rising seas do not simply flood tidal landscapes so that tidal basins cannot be considered as a bathtub. Morphological change in tidal basins during sea level rise is a first-order effect, radically changing the prediction of the future state of tidal embayments and losses in habitat area. These morphological changes are likely to vary from site to site depending on environmental conditions such as sediment type, influx of sediment from further offshore or from the surrounding catchment, and vegetation coverage. For example, studies have recently started to address the feedback mechanisms arising from the presence of vegetation and the ability of vegetated marsh platforms to maintain their elevation relative to a rising sea level (Morris et al., 2002; Kirwan and Murray, 2007).

Human pressures on earth's environmental systems are increasing (Vitousek et al., 1997). Growing awareness of the consequences related to modifying tidal embayments and its ecosystems has resulted in the development of adaptation, mitigation, and restoration strategies (e.g. Deltacommissie, 2008). The success of these comprehensive and often highly-expensive strategies hinges on our knowledge of the system. Continuous development of strategies to address the morphodynamic feedback loop is essential to advance our understanding of tidal embayments which provides the foundation for sound management of these valuable and vulnerable environments.

Chapter 5

Modelling the effects of mangroves on the evolution of channel networks in tidal embayments

5.1 Introduction

Studies on biomorphodynamics address the feedback between organisms and physical processes. Such a feedback involves studying not only how biology affects morphological evolution but also how organisms can in turn be dependent on morphology and physical forcing (Murray et al., 2008). This type of study has already proven that many complex environmental systems cannot be fully understood without the consideration of these two-way interactions that link physical and biological processes (e.g. Baas, 2002; Murray and Paola, 2003; Daanen et al., 2008). In recent years the role of physical-biological interactions in driving morphological evolution of tidal landscapes such as estuaries and tidal embayments has also been explored over a range of spatial and temporal scales (e.g. Morris et al., 2002; van de Koppel, 2005; D'Alpaos et al., 2006; Temmerman et al., 2007; Mariotti and Fagherazzi, 2010; Marani et al., 2010).

Salt marsh plants enhance accretion due to organic and inorganic sedimentation (e.g. Morris et al., 2002), change sediment composition and therefore entrainment characteristics, and are capable of increasing the flow resistance experienced by the tidal flow (e.g. Nepf, 1999). Consequently, vegetation influences the evolution of both the marsh surface and the cross-sectional geometry of the channels dissecting the marsh platform (D'Alpaos et al., 2006). The increase in sediment accumulation due to salt marsh plants has also been held responsible for creating the characteristic steep salt marsh edges, making salt marshes vulnerable to wave attack (van de Koppel, 2005). How the interactions between vegetation, tidal flow, waves, sediment erosion, and deposition drive the evolution of the marsh boundary has been further investigated by Mariotti and Fagherazzi (2010). Implementation of the effects of salt marsh plants on drag and turbulence into a three-dimensional hydrodynamic model indicated that vegetation has a strong control on flow routing and sedimentation patterns (Temmerman et al., 2005). The

application of a morphodynamic model, accounting for these effects of vegetation on flow characteristics, to simulate plant colonization and channel formation on a tidal flat showed that flow concentration between vegetated patches leads to enhanced channel erosion (Temmerman et al., 2007). In the simulations presented by Temmerman et al. (2007), a higher vegetation density resulted in stronger flow concentration so that a denser pattern of channels was eroded.

One of the challenges in studying the development of morphological equilibria is that the environmental forcing conditions are constantly evolving. Recent concern on rising sea levels has focused research into determining the fate of vegetated intertidal areas. Tidal wetlands are amongst the most productive ecosystems in the world (Mitsch and Gosselink, 2007), providing nursery grounds for fish and habitats for a variety of vegetation types and benthic organisms (Levin et al., 2001). A decrease in coastal wetland area will therefore have serious economic and ecological implications (Nicholls et al., 1999). Although there are many facets to the way in which the salt marsh ecosystem might change, recent work has focused on the ability of intertidal areas covered with salt marsh plants to maintain their elevation relative to a rising sea level (Morris et al., 2002). Increases in primary productivity occur with increasing water depth (up to an optimal depth), enhancing sediment trapping and organic matter accretion such that the salt marsh remains stable against variations in sea level. These intriguing feedback mechanisms have also been incorporated in spatially-explicit numerical models. Kirwan and Murray (2007) built a model that incorporated the feedback interactions found by Morris et al. (2002) and that also included the additional effect that plants have on stabilizing channel banks. Their simulations indicate that the presence of vegetation promotes the maintenance of intertidal surface areas. D'Alpaos et al. (2007a) also discuss the existence of equilibrium water depths using numerical simulations. In addition, they show that in the case of a positive feedback between bed elevation and accretion, which arises from vegetation species for which biomass increases with bed elevation, intertidal areas may make the transition to upland.

Previous studies have highlighted the importance of plants in affecting the feedback processes which drive morphological evolution, yet only a limited range

of vegetation species have been examined. Mangrove forests are the tropical and subtropical equivalent of salt marshes and are likely to initiate similar type of physical-biological interactions. Mangroves are a taxonomically diverse group of halophytic (salt-tolerant) plants comprising many different species (Tomlinson, 1986). They occur in sheltered tidal environments, growing on a variety of substrates. Although mangrove forests are in decline on a global scale (Duke et al., 2007), mangroves are rapidly spreading in areas where land-use change associated with agricultural development and urbanization has caused increases in sediment and nutrient loads from the catchment (Swales et al., 2007). The habitat of mangroves is restricted to areas with specific salinity and inundation regimes (Krauss et al., 2008) and hence inherently related to bed elevation. In turn, mangroves play a role in determining the bed elevation by affecting both hydrodynamic and sediment transport processes (e.g. Mazda et al., 2005; Quartel et al., 2007; van Santen et al., 2007), thus coupling again physics and biology. Although it is to be expected that this two-way biophysical coupling is one of the governing factors in the morphological evolution of mangrove environments, studies addressing its importance are scarce.

We developed a numerical model to explore the role of mangroves in the large-scale morphological evolution of tidal embayments. Here we consider the *Avicennia marina*, a species which occurs in both hemispheres (Duke, 1990) and also extends its range into cooler warm-temperate climates. The effects of mangroves on physical processes that have been included in the model are: 1) increasing flow resistance; 2) increasing sediment's resistance to erosion by tidal flow; 3) increasing sediment's resistance to slope-driven sediment transport; and 4) increasing accretion by producing organic matter. Model results are analyzed with regard to the influence of mangroves on tidal channel network evolution with a focus on the effect on channel density. In addition we perform simulations to examine how the channel network evolves under a rising sea level in both the presence and absence of mangrove vegetation.

5.2 Methodology

We extend the morphodynamic model presented in Chapter 2, which is capable of simulating the long-term morphological evolution of tidal embayments, to account

for the interactions between mangroves and physical processes. A description of model set-up is given in the following section. The development of the morphodynamic model has been discussed in detail in Chapter 2 and will only be briefly described here. Then we explain in detail how we treated the colonization of new areas by mangroves, and the growth and mortality of mangrove trees. We also give a detailed description of how we implemented the effects of mangroves on hydrodynamics and sediment transport processes. Finally, we describe the technique used here to extract the channel network from the simulated morphologies.

5.2.1 Model set-up

An idealised initial bathymetry (similar to the one used in previous chapters) was used for the numerical simulations performed in this study. This initial topography was composed of an offshore area, inlet, and basin and represented a domain of 17 $\times$ 17 km. Bed elevations in the offshore area, which extended 7 km seaward, increased from -8 m at the seaward boundary to -2 m at the entrance of the basin. Land regions separated the offshore area from the tidal basin. Within the basin, bed elevation further increased towards +2 m at the landward boundary and random perturbations of -1.5 to +1.5 cm were added to the bed level in this area. The model was forced with a semidiurnal sinusoidal tide and the tidal range was 2 m. The sediments had a mean grain size diameter of 0.12 mm. A grid size of 100 m in both x- and y-direction was used.

5.2.2 Morphodynamic model

To summarise Chapter 2, the numerical model which formed the basis of the model used throughout this study simulates morphological change as a result of the interactions between hydrodynamics, sediment transport, and the evolving morphology. Hydrodynamic computations are performed using ELCOM (Estuary and Lake Computer Model; Hodges et al., 2000). This is a 3D hydrodynamic model based on the unsteady Reynolds-averaged Navier-Stokes equations for incompressible flow using the hydrostatic assumption and closed by a turbulent closure scheme. The equations are solved on the same rectangular grid described in the previous section. Influences of Coriolis force, density differences, wind, and waves are neglected.

Flow velocities, computed every hydrodynamic time-step, are used to obtain instantaneous sediment transport rates which are calculated according to the sediment transport formula developed by Engelund and Hansen (1967). Slope-driven sediment transport is incorporated in the model by following the approach of Kirwan and Murray (2007). Gradients in sediment transport rate yield bed level changes due to conservation of sediment mass. Bed level changes are integrated over one tidal cycle and then multiplied by a morphodynamic time-step before morphological change feeds back into the hydrodynamic model. The morphodynamic time-step in the model varies under the assumption that hydrodynamic conditions remain constant until bed level changes exceed 10% of the local water depth at high tide. This facilitates the execution of long-term simulations.

5.2.3 Mangrove colonization, growth, and mortality

Avicennia marina colonizes new areas through a supply of propagules and the subsequent establishment of seedlings. The initial development of the young plants, the propagules, takes place while they are still attached to the parent plant. When the propagules are fully developed, they are released and drop directly on the substrate or into the water after which they are dispersed by the tidal currents. The dispersal distance of propagules is generally limited, however, observations of propagules further than 10 km have also been reported (Clarke, 1993), which allows for recruitment to neighbouring estuaries. The distribution of *Avicennia marina* has been found to lie in between mean sea level and mean high water (Clarke and Myerscough, 1993). In the numerical model, therefore, mangroves can only establish themselves in grid cells which are inundated less than half of the time. There is a 1 percent chance each year that initial mangrove establishment occurs in a bare grid cell. Furthermore, mangroves are allowed to expand laterally to the four neighbouring grid cells. The initial mangrove density is set to 3000 individuals per ha (which is also the size of the grid cells). This initial density was also used by Berger and Hildenbrandt (2000). The trees have an initial height of 15 cm.

Growth of the mangrove trees is described by (Chen and Twilley, 1998; Berger and Hildenbrandt, 2000):

$$\frac{dD}{dt} = \frac{GD(1-(DH)/(D_{\max}H_{\max}))}{(274+3b_2D-4b_3D^2)}, \quad (5.1)$$

where D is the stem diameter (cm), H is the tree height (cm), t is time (years), $D_{\max}$ and $H_{\max}$ are the maximum stem diameter and tree height and are set to 40 cm and 1000 cm, respectively. G, b_2, and b_3 are species-specific growth parameters which are set here to respectively 168.36, 50, and 0.625 such that the maximum increase in stem diameter is 1 cm/year and the tree height and stem diameter are related as (based on the work by Berger and Hildenbrandt, 2000):

$$H = b_2D - b_3D^2. \quad (5.2)$$

Equation (5.1) defines the increase in stem diameter over time under optimal growth conditions. In reality, however, the growth of mangroves is limited by stresses. Flooding and competition control mangrove growth and the effects of these stresses on growth are, similar to Chen and Twilley (1998) and Berger and Hildenbrandt (2000), incorporated by adding correction factors to Equation (5.1):

$$\frac{dD}{dt} = \frac{GD(1-(DH)/(D_{\max}H_{\max}))}{(274+3b_2D-4b_3D^2)} \cdot I \cdot C. \quad (5.3)$$

These extra multipliers should range between 0 and 1.The correction factor for inundation I is dependent on the hydroperiod and we relate the two by using a sigmoid function:

$$I = \frac{1}{1+\exp[c_1(P_{0.5}-P)]}, \quad (5.4)$$

where P represents the relative hydroperiod and $P_{0.5}$ is the value of P for which the multiplier is 0.5. c_1 is a constant and is set to –40. A value of 0.5 is chosen for $P_{0.5}$ so that the mangrove growth is 50% of the growth under optimal conditions when the mangroves are half of the time inundated. We here thus assume that

mangrove trees stop growing when they are permanently inundated and that the growth of the trees is not hindered when they are inundated for only short periods of time. Neighbouring trees compete with each other for resources and the correction factor for competition *C* is thus determined by the total biomass *B*:

$$C = \frac{1}{1 + \exp\left[c_2 \left(B_{0.5} - B\right)\right]}, \quad (5.5)$$

where c_2 is another constant and is set to -0.0002. In order to compute *B*, we multiplied the number of trees per grid cell with the weight of a single mangrove tree W_{tree} which is given by the summation of the above-ground $W_{tree,a}$ and below-ground $W_{tree,b}$ tree weight:

$$W_{tree} = W_{tree,a} + W_{tree,b}. \quad (5.6)$$

The above-ground and below-ground tree weight of the *Avicennia marina* is given by the following allometric relationships (Comley and McGuinness, 2005):

$$W_{tree,a} = 0.308 D^{2.11} \text{ and} \quad (5.7)$$
$$W_{tree,b} = 1.28 D^{1.17}. \quad (5.8)$$

Berger and Hildenbrandt (2000) modelled the competition among mangrove trees by considering a circular zone around each tree in which the tree exploits resources. They proposed a simple relationship to evaluate the radius *R* of this particular zone:

$$R = 10\sqrt{0.5\frac{D}{100}}. \quad (5.9)$$

Application of Equation (5.9) leads to the outcome that 125 mature (D=$D_{\max}$=40 cm) mangrove trees can be present per ha (size of a grid cell) without mangroves having to compete for resources (circular zones around trees used for resources are not overlapping). $B_{0.5}$ in Equation (5.5) is set to $1.04 \cdot 10^5$ kg/ha which is the total biomass associated with 125 mature trees.

Mangrove trees have adapted to temporal flooding and the low oxygen supply by growing pneumatophores (aerial roots). These grow to a few tens of centimetres high (Küchler, 1972) and a single *Avicennia marina* tree can have more than 10000 pneumatophores (Hogarth, 2007). As described in the following section, pneumatophores affect physical processes by increasing the flow resistance. We developed a sigmoid function which relates the number of pneumatopores per tree N_{pneu} and the stem diameter such that the number of pneumatophores is 10000 for a tree with a stem diameter equal to $D_{\max}$:

$$N_{pneu} = 10050\left(\frac{1}{1+\exp[c_3(D_{0.5}-D)]} - 0.00247\right), \quad (5.10)$$

where c_3 and $D_{0.5}$ are set to 0.3 and 20, respectively.

The growth of mangroves is limited by inundation and competition stress according to Equation (5.3). Following Berger and Hildenbrandt (2000), tree mortality occurs after continuous periods of growth depression. Therefore, mangrove growth is evaluated in the model every year and trees die when the growth is less than 50% of the growth under optimal conditions for 5 consecutive years. The death of mangroves reduces the competition among the remaining trees and therefore improves growth conditions. Practically, when the product $I \cdot C$ in Equation (5.3) is below 0.5 for 5 consecutive years, mangrove density decreases until the growth depression is halted and the product $I \cdot C$ thus equals or exceeds again a value of 0.5. When conditions become more favourable for mangrove growth because of a decrease in inundation stress, the number of trees increases until the product $I \cdot C$ reaches a value of 0.5. The mangrove trees which are added enter with a stem diameter and height similar to the dimensions of the trees already present in the grid cell under consideration. In the case of no inundation stress (I=1), the self-thinning process (decrease in number of individuals) in the mangrove forest induced by competition among individuals eventually results in a mangrove density of 125 mangrove trees per ha. When inundation stress hinders the growth of mangroves (I<1), the final mangrove density is lower.

5.2.4 Implementing the effects of mangroves on physical processes

Aquatic plants are well-known for offering additional resistance to the flow (e.g. Nepf, 1999). For example, Mazda et al. (1997a) showed that the drag force by the mangroves is strongly dependent on the total projected area of obstacles A in the control volume V and the total volume of obstacles V_M in V. Mazda et al. (1997a) related the drag coefficient with a characteristic vegetation length scale L which is defined as:

$$L = (V - V_M)/A. \quad (5.11)$$

The height of control volume V equals the local water depth and L therefore varies with water depth (Mazda et al., 1997a). In addition, L contains information about the spacing between the trunks and roots of the mangrove trees and L decreases (decreasing spacing) with increasing V_M and A. The drag coefficient C_D is thus inversely correlated with L and we here developed the following relationship:

$$C_D = C_{D,no} + \frac{5}{L}, \quad (5.12)$$

where $C_{D,no}$ is the drag coefficient when no mangroves are present and is set to 0.005. For the computation of A and V_M we simplified the shape of the trunk and the pneumatophores to circular cylinders and did not consider the crown of the tree, assuming that the crown of the tree is limited in size or above high tide. This assumption follows Küchler (1972) who described that the crown of *Avicennia marina* is well above high tide when the growth of the tree is not limited by low temperatures. Furthermore, we here used the maximum water depth throughout the tidal cycle for the computation of V. To give an example, Equation (5.12) implies that for a mangrove density of 125 individuals per ha and trees with a stem diameter of 40 cm the drag coefficient C_D amounts to 1.91, 4.76, and 6.35 for water depths of respectively 0.5, 0.2, and 0.1 m. These C_D-values are within the range found by Mazda et al. (1997a). The effect of mangroves on drag can be incorporated in the numerical model as a bottom friction (Mazda et al., 1997b; Quartel et al., 2007). The drag coefficient values computed following Equation (5.12) were thus used as input for the bottom friction formulation within the

hydrodynamic model and, as such, the mangroves directly affect hydrodynamic conditions.

As mentioned earlier, sediment transport rates are calculated with the Engelund and Hansen (1967) formula which is traditionally written as:

$$S_{flow} = \frac{0.05U^5}{\sqrt{g}C^3\Delta^2 D_{50}}, \quad (5.13)$$

where S_{flow} is the sediment transport flux, U is the magnitude of flow velocity, g is the gravitational acceleration, C is the Chézy coefficient (set to 65 $m^{0.5}/s$), Δ is the relative density $(\rho_s-\rho)/\rho$, ρ_s is the sediment density, ρ is the water density, and D_{50} is the median grain size. Equation (5.13) is developed with the assumption that the critical Shields (mobility) parameter θ_{cr} amounts to 0.06. Mangroves increase the resistance of sediments to erosion because the roots of the mangroves play a role in stabilizing the sediments. If we relax the assumption of a constant θ_{cr}, the sediment transport model can be written as:

$$S_{flow} = \frac{0.125CUD_{50}}{\sqrt{g}}\left(0.06 + 0.4\theta^2 - \theta_{cr}\right) \quad \text{for} \quad 0.06 + 0.4\theta^2 > \theta_{cr} \quad \text{and} \quad (5.14)$$

$$S_{flow} = 0 \quad \text{for} \quad 0.06 + 0.4\theta^2 \le \theta_{cr}, \quad (5.15)$$

where θ is the Shields parameter which is given by:

$$\theta = \frac{\rho U^2}{C^2(\rho_s - \rho)D_{50}}. \quad (5.16)$$

Equations (5.14) and (5.15) allow for an erosion threshold which is dependent on the below-ground biomass. Based on the work by Mariotti and Fagherazzi (2010), who linearly correlated the increase in erosion threshold with biomass, we parameterized the influence of mangroves on the erodibility of sediments as:

$$\theta_{cr} = \theta_{cr,no}\left(1 + K_{cr}\frac{B_b}{B_{b,mature}}\right), \quad (5.17)$$

where $\theta_{cr,no}$ is the critical Shields parameter when no mangroves are present and is set to 0.06 such that the sediment transport model reduces to Equation (5.13) when mangroves are not present. B_b is the below-ground biomass and $B_{b,mature}$ is the below-ground biomass of 125 mature (D=$D_{\max}$) mangroves per ha. K_{cr} is a constant and we used a value of 0.1 so that the θ_{cr} is 10% larger in a mature mangrove forest. Following Equations (5.14), (5.15), and (5.16), a 10%-increase (θ_{cr}=0.066) implies that no sediment transport occurs for a flow velocity below 0.31 m/s. Because of the self-thinning process in the mangrove forest it is possible that during the development of the forest, although the below-ground tree weight per tree is lower, the large number of individuals causes B_b to be higher than $B_{b,mature}$. However, in the model we restrict the ratio between B_b and $B_{b,mature}$ in Equation (5.17) so that it cannot exceed 1.

The roots of mangrove trees do not only increase the sediment's resistance to erosion by the tidal flow, they also decrease the magnitude of slope-driven sediment transport fluxes and allow steeper slopes to develop in the morphology. Modelling efforts, which have previously explored the effects of the reduction in gravitationally driven sediment transport by vegetation (Murray and Paola, 2003; Kirwan and Murray, 2007), applied a reduction by approximately two orders of magnitude in the case of fully developed vegetation. Similar to Kirwan and Murray (2007) we calculated the slope-driven sediment transport S_{slope} as:

$$S_{slope} = \left(\alpha - \beta \frac{B_b}{B_{b,mature}} \right) b , \quad (5.18)$$

where b is the slope towards the neighboring grid cell. Slope-driven sediment transport only occurs when b exceeds 0.01. The ratio between B_b and $B_{b,mature}$ is again not allowed to exceed 1. We here took a conservative approach and applied a maximum reduction of S_{slope} by one order of magnitude and the values of the dimensional constants α (1.1574×10^{-5} m^2/s) and β (1.0417×10^{-5} m^2/s) were chosen accordingly.

Mangroves produce organic matter and because decomposition of this material is extremely slow (Middleton and McKee, 2001) the organic matter builds up which raises the soil surface a few millimetres per year over long periods of time. This accumulation of organic material may play an important role in the maintenance of soil surface elevation relative to a rising sea level (McKee et al., 2007). Numerical models to study the dynamics of salt marsh systems usually apply a linear relationship between the production of organic matter and biomass (e.g. D'Alpaos et al., 2006; D'Alpaos et al., 2007a; Mariotti and Fagherazzi, 2010). The main component of organic deposits in mangrove forests is refractory roots with leaf litter playing a secondary role (Middleton and McKee, 2001). We therefore relate the elevation change due to organic production ΔZ_{org} to the below-ground biomass:

$$\Delta Z_{org} = K_{org} \frac{B_b}{B_{b,mature}}, \quad (5.19)$$

where K_{org} is a characteristic accumulation rate. Little information exists on root volumetric input and related surface elevation changes and field measurements which have been performed (although in mangrove forests with different species as considered here) suggest that a wide range of accumulation rates is possible (McKee, 2011). We here set K_{org} to a conservative 1 mm/year.

5.2.5 Extracting the channel network

We here analyze how mangroves influence the evolution of the channel network and focus on the effect of mangroves on channel density. To determine channel density it is necessary to extract the channel network from the simulated morphologies and we here apply a technique based on the work by Passalacqua et al. (2010) to accomplish this. This technique includes nonlinear geometric filtering of the topography to enhance features that are critical to the network extraction. The geometric curvature of the isoheight contours is then calculated. Channelized areas are characterized by positive curvature and channels are defined as areas where a sudden change in the statistical signature of the landscape occurs. We refer the reader to Passalacqua et al. (2010) for further details.

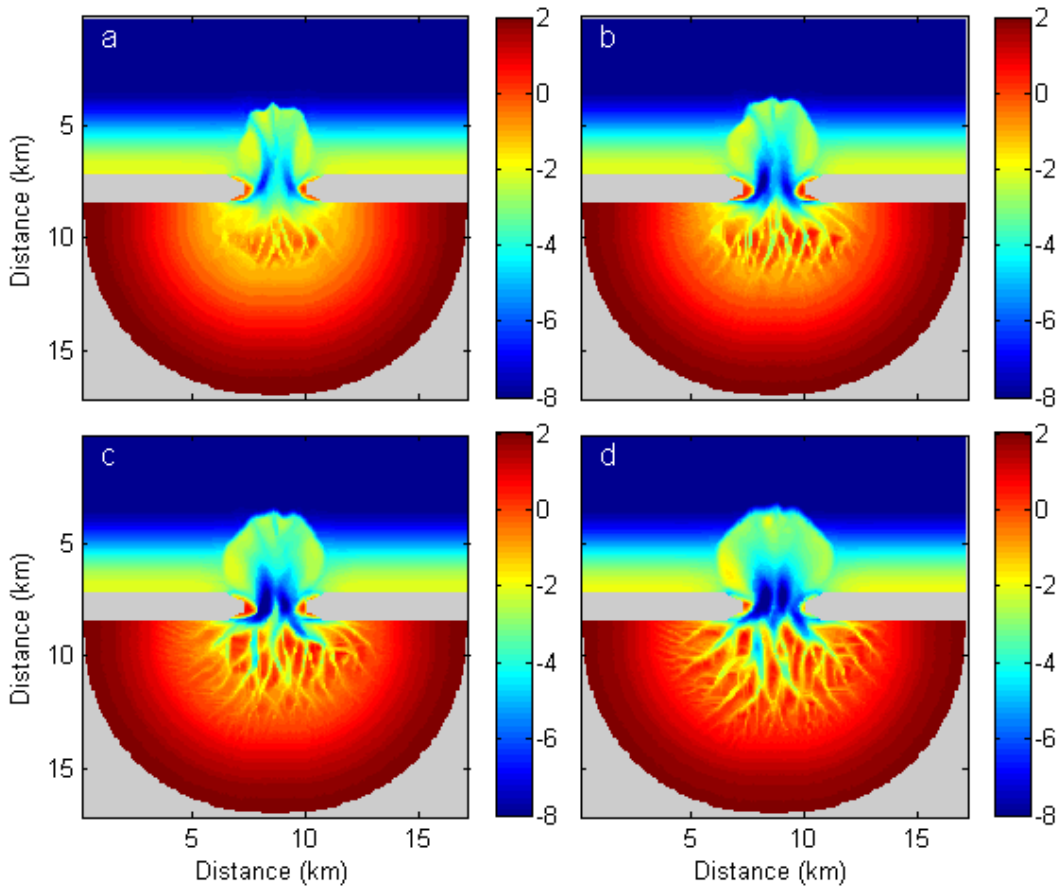

Figure 5.1. Simulation of tidal channel network formation when mangroves are not present. Morphologies after (a) 5, (b) 20, (c) 50, and (d) 140 years. Grey areas represent land regions which form impermeable and non-erodible barriers. Colorbars represent the bed elevation (m).

5.3 Results

5.3.1 Morphological evolution in the absence and presence of mangroves

The numerical model was first used to simulate the formation of a tidal channel network starting from the unchannelized initial bathymetry and without the presence of mangroves (Fig. 5.1). As described in previous chapters, a complex network develops over long time scales, indicating that the interactions between hydrodynamics, sediment transport, and the evolving topography are sufficient to give rise to channel pattern development. Large bathymetric changes occurred within the first few years of morphological evolution (Fig. 5.1a). Two deep channels rapidly developed in the inlet of the tidal system. During ebb-tides, large volumes of sediment were transported towards the offshore area where decelerating flows caused sediment deposition and the formation of an ebb-tidal

delta. The initiation of tidal channels and the development of intertidal areas changed the morphology of the tidal basin. During subsequent morphological evolution the channels through the inlet continued to deepen, the ebb-tidal delta increased in size, and the channels in the basin continued to branch. This process of branching of the channels ultimately resulted in the formation of a complex tidal channel network (Fig. 5.1b-d).

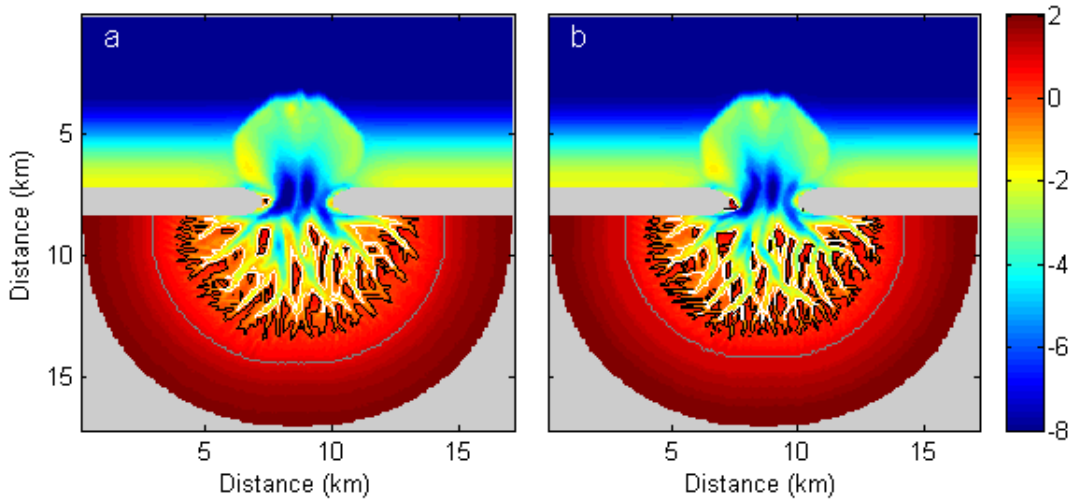

Figure 5.2. Simulated morphology after 140 years (a) without mangroves and (b) with mangroves. In the vegetated scenario mangroves started to grow after 50 years. White, black, and grey lines represent -1 (low tide), 0 (mid tide), and 1 (high tide) m contour lines, respectively.

We used this preliminary model simulation described above as a base case against which to explore the effects of mangroves on morphological evolution. To reduce computational time we took the bathymetry generated after 50 years of morphological evolution without mangroves (Fig. 5.1c) and allowed mangroves to start growing from this point onwards. Mangroves started thus to colonize bare areas and have an effect on hydrodynamics and sediment transport processes as described in Section 5.2.4. Unvegetated and vegetated scenarios were then compared to assess how mangroves affect the evolution of the channel network. Figure 5.2 shows the simulated morphologies after 140 years in the absence (Fig. 5.2a) and presence (Fig. 5.2b) of mangroves and large differences can be detected when the two are compared in detail. Where mangroves are present the accumulation of organic matter causes the bed elevation to increase around 1

mm/year (Eq. 5.19). Vegetated areas in the upper part of the tidal basin could therefore make the transition to upland and the high-tide mark consequentially moved seaward (compare the grey lines in Fig. 5.2a and b). Deposition and erosion of sediment driven by the tidal flow ceased once the soil surface within the mangrove forest reached an elevation such that the surface became permanently dry. Bed level changes in these vegetated areas were then solely determined by organic accretion. The hypsometric curves of the basins with and without mangroves (Fig. 5.3) indicate that, although the differences are small, a larger proportion of bed elevations (increase of around 1%) are below 2 m in the vegetated basin. Also, where mangroves are present a larger area (around 2% of the total basin area) occurs above a bed elevation of 0 m which is approximately the elevation at which mangroves start growing. The transition of vegetated areas to upland, caused by the production of organic matter, is responsible for the increase (around 4%) in surface area above a bed elevation of 1 m. Mangroves enhance the resistance of channel banks to erosion by decreasing the slope-driven sediment transport through Equation (5.18). The strength of the channel banks increases when they are covered with mangroves because of the stabilizing character of the roots. The sediment which is transported down slope from a vegetated grid cell to the adjacent channel cell is thus reduced, causing the channel banks to become steeper. The steeper slope of the channel banks is resembled by the smaller distance between the -1 m and 0 m contour lines (white and black lines in Fig. 5.2, respectively) for the vegetated bathymetry. Finally, when the morphologies with and without mangroves are compared it can be observed that mangroves enhance channel formation. Especially when the 0 m contour lines are followed it becomes clear that the channels have undergone additional branching in the basin where mangroves are present. Differences in channel density between the unvegetated and vegetated scenario will be discussed later.

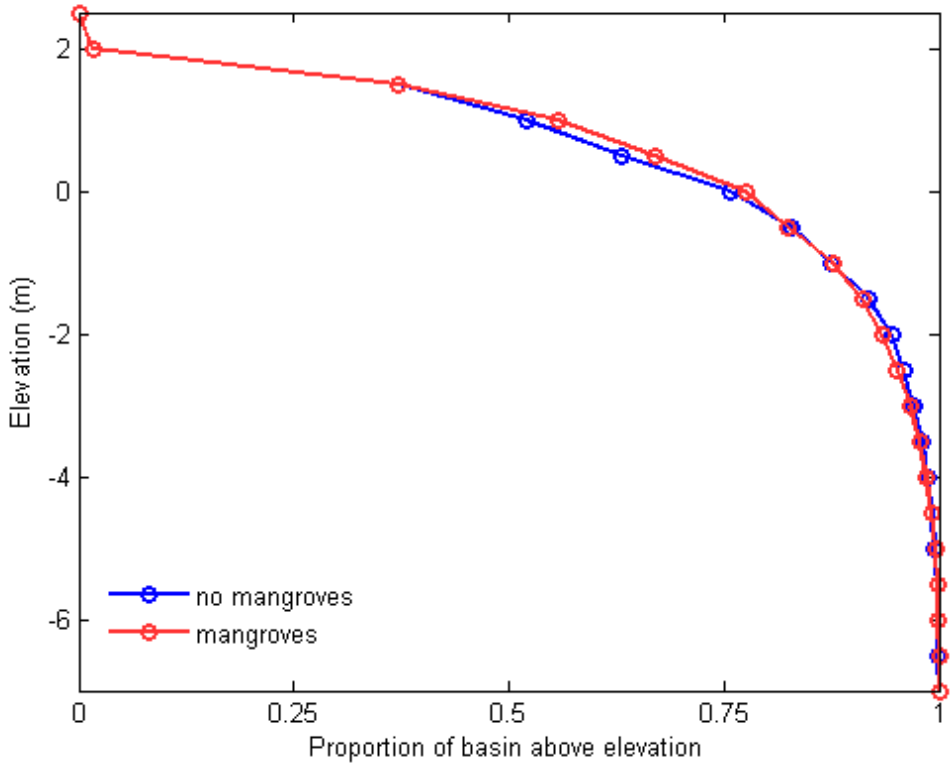

Figure 5.3. Hypsometric curves for the unvegetated and vegetated morphology after 140 years.

Temmerman et al. (2005) analyzed in detail the hydrodynamics in a tidal marsh landscape and concluded that salt marsh plants have a strong control on flow patterns. To study the effects of mangroves on the hydrodynamic conditions in our simulations we extracted the flow field during rising (Fig. 5.4) and falling (Fig. 5.5) tide over both the unvegetated and vegetated morphologies. The direction as well as the magnitude of the flow has changed because of the presence of mangrove trees. During rising tide the flow in the vegetated scenario (Fig. 5.4b) is mainly concentrated within the tidal channels. Similar to the results as described by Temmerman et al. (2005), the flow from the channel onto the vegetated platform sometimes occurs almost perpendicular to the direction of the tidal channel. When vegetated areas become inundated the extra drag caused by the mangrove trees results in a strong reduction in the magnitude of the flow which in turn leads to negative gradients in sediment transport and thus an increase in deposition and bed elevation. On the other hand, the extra flow resistance in mangrove forests results in flow concentration and sediment erosion in between vegetated areas and thus enhances the formation of channels. The flow

is less constricted to the channel network when mangroves are absent (Fig. 5.4a). The flow on the unvegetated intertidal areas also reaches higher velocities in comparison with the vegetated scenario and strong reductions in the magnitude of the flow are then also missing. Similar types of differences in the flow characteristics can be observed between the vegetated and unvegetated scenario during falling tide (Fig. 5.5). In the absence of mangroves (Fig. 5.5a) the water is drained through the channels as well as over the intertidal areas. The magnitude of the flow is relatively homogeneous and the flow is primarily directed towards the main inlet of the tidal basin (the left-top corner in Fig. 5.5a). In contrast, smaller velocities occur within the mangrove forest (Fig. 5.5b) and the flow is mainly directed towards the nearest channel through which the water is then subsequently drained. The flow thus concentrates again within the channels.

Figure 5.2 and the enlargements given by Figures 5.4 and 5.5 already showed that the effects that mangroves have on hydrodynamics and sediment transport result in enhanced channel formation. These tidal channels in turn have a strong control on the hydrodynamics and sediment transport and thus feedback on the overall morphological behaviour of tidal embayments. To further quantify the influence of mangroves on the network, the technique described in Section 5.2.5 was applied to extract the channel networks from the simulated morphologies given in Figure 5.2 and the number of channels as a function of distance from the coastal inlet was then evaluated (Fig. 5.6). In the deeper regions of the inlet, the number of channels increases in the landward direction, because of the naturally branching character of the network. The abrupt decline in channel occurrence at around 5 km from the entrance is the result of the tidal channels expanding landward at different rates. A higher channel density can be observed for the vegetated scenario in the area between the inlet entrance and 5.2 km. Mangroves enhanced the formation of channels especially in between 4 and 5 km from the inlet. From 5.2 km landwards, however, channel density is higher for the unvegetated scenario, indicating that the channels expanded landward further when mangroves were absent.

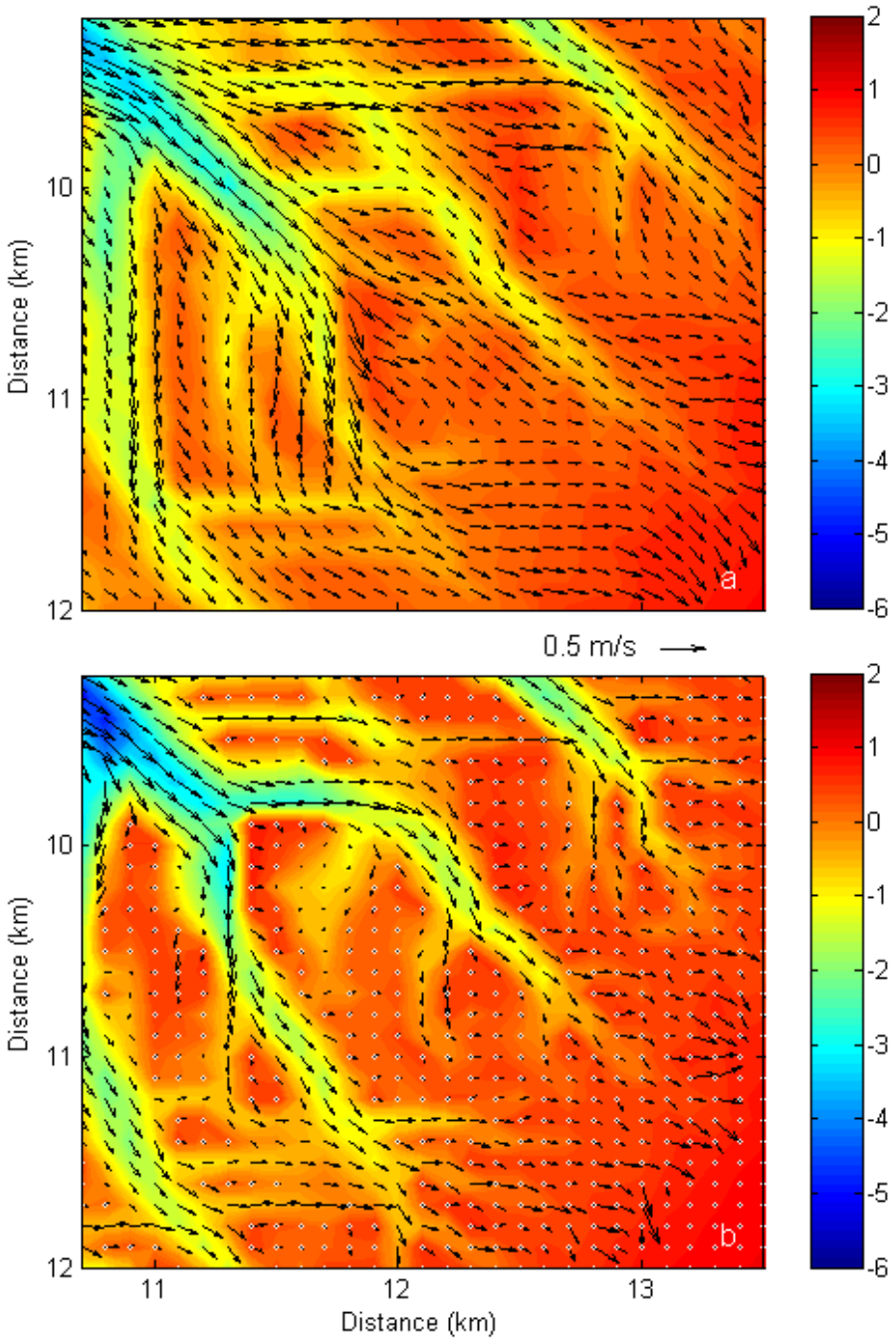

Figure 5.4. Flow field during rising tide over a part of the (a) unvegetated and (b) vegetated morphology after 140 years. Arrows on both panels represent magnitude and direction of the flow. Scale of the arrows is indicated in between the two panels. The white circles on panel (b) indicate the grid cells where mangroves are present. The axis correspond to the axis of Fig. 5.2.

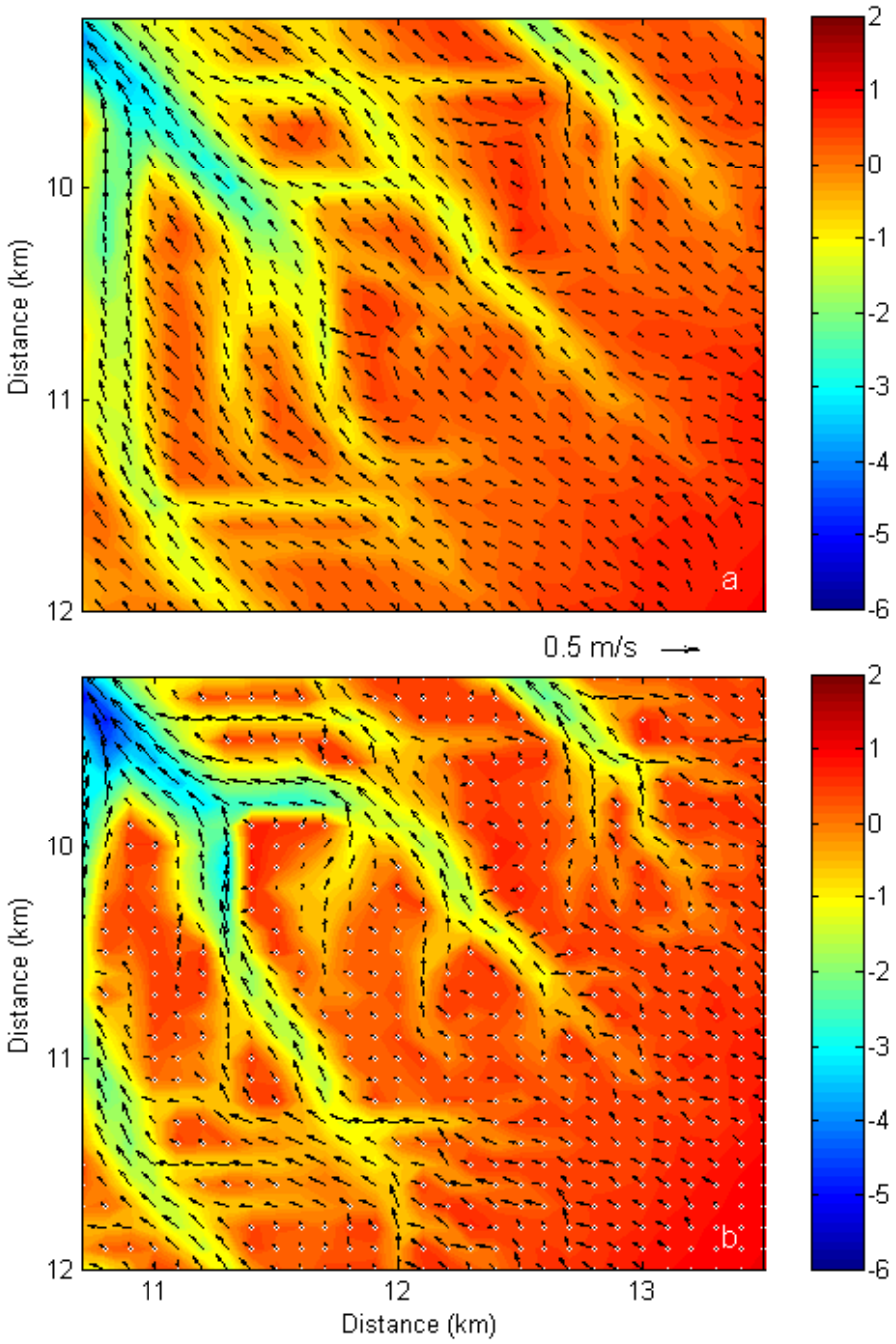

Figure 5.5. Flow field during falling tide over a part of the (a) unvegetated and (b) vegetated morphology after 140 years. Arrows on both panels represent magnitude and direction of the flow. Scale of the arrows is indicated in between the two panels. The white circles on panel (b) indicate the grid cells where mangroves are present. The axis correspond to the axis of Fig. 5.2.

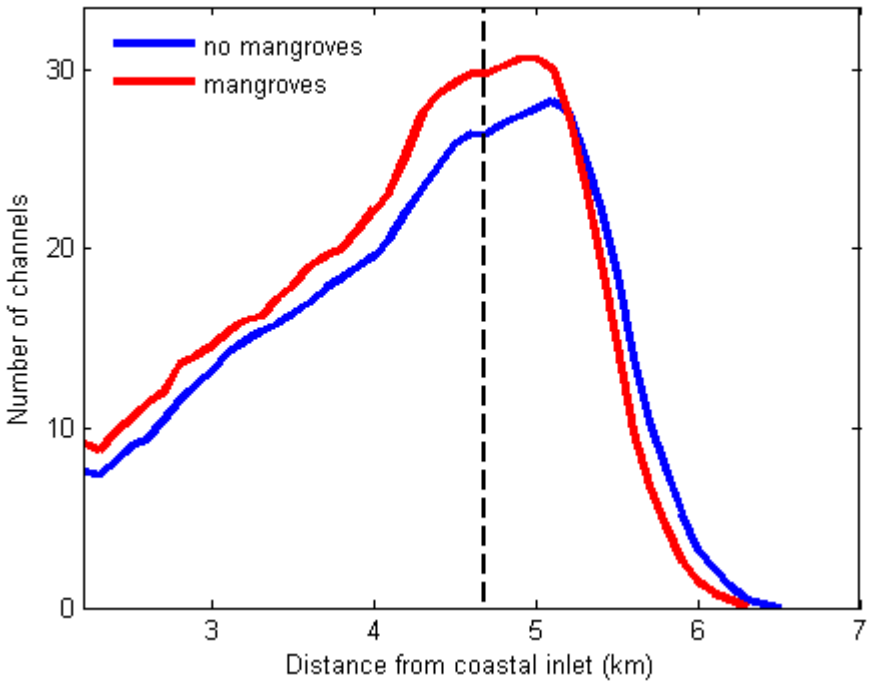

Figure 5.6. Number of channels versus distance from the coastal inlet for the unvegetated and vegetated morphology after 140 years. The number of channels is shown as a moving average over 500 m. The vertical dashed line represents the distance from the coastal inlet (similar for the unvegetated and vegetated scenario) for which the bed elevation averages 0 m (mid tide).

5.3.2 Clarifying the role of each effect in changing channel density

In our model, mangroves affect hydrodynamics and sediment dynamics in four different ways (Eqs. 5.12, 5.17, 5.18, and 5.19) and differences in the channel networks of the unvegetated (Fig. 5.2a) and vegetated (Fig. 5.2b) morphologies are the cumulative result of these four effects. To provide a better understanding of how mangroves affect the formation of channels we performed additional simulations to elucidate how each single effect that mangroves have on physical processes influences channel formation. Results of these simulations are described in this section.

Four additional simulations were performed and each time only one out of the four effects of mangroves on physical processes was included while the remaining three were ignored. Furthermore, we kept the extent to which mangroves influenced either hydrodynamics or sediment dynamics constant and thus

independent of mangrove density and the size of the trees. Figure 5.7c-f shows part of the simulated morphology after 140 years when the effect of mangroves on C_D, θ_{cr}, S_{slope}, and ΔZ_{org} respectively was included. In the simulation used to assess the importance of the extra drag produced by mangroves, we used a constant value of C_D=5.0 for grid cells covered with mangroves. As previously discussed, mangroves obstruct the flow which leads to flow convergence and increased erosion in the areas between vegetated regions. As a result, channel formation is enhanced (compare Fig. 5.7a and c). The work by Temmerman et al. (2007) showed that this mechanism is also responsible for channel formation in between patches of salt marsh plants on a tidal flat. The maximum number of channels at a specific distance from the coastal inlet is higher when only the effect of mangroves on drag is included than when all the four effects are taken into account (compare Figs. 5.6 and 5.8a). Moreover, channel density in the unvegetated and vegetated morphology is equal in the upper part of the basin where the number of channels decreases again (Fig. 5.8a). This suggests that the extra drag force caused by mangroves is not the main factor responsible for the limited ability of tidal channels in vegetated basins to expand landward as was observed in Figure 5.6.

We set θ_{cr} to 0.066 (applying the maximum increase in the critical Shields parameter of 10% compared to 0.06 in the unvegetated areas) where mangroves were present in the simulation to investigate how the decrease in sediment transport induced by the tidal flow in vegetated areas affects morphological evolution. Incorporating a critical Shields parameter in the sediment transport model (Eqs. 5.14 and 5.15) which increases within the mangrove forest results in a strong reduction in sediment transport fluxes once the flow encounters mangroves trees. Net sediment deposition in this area allows the difference in bed elevation between the unvegetated channel and the adjacent vegetated platform to increase. The variations in the sediment's resistance to erosion drive additional branching of the channels (Figs. 5.7d and 5.8b). At the same time, mangroves which cover the area at the headward side of the channels decrease the erodability of the sediment and hinder the possibility of these channels expanding landward. Consequentially, the number of channels starts to decrease relatively close to the coastal inlet (Fig. 5.8b).

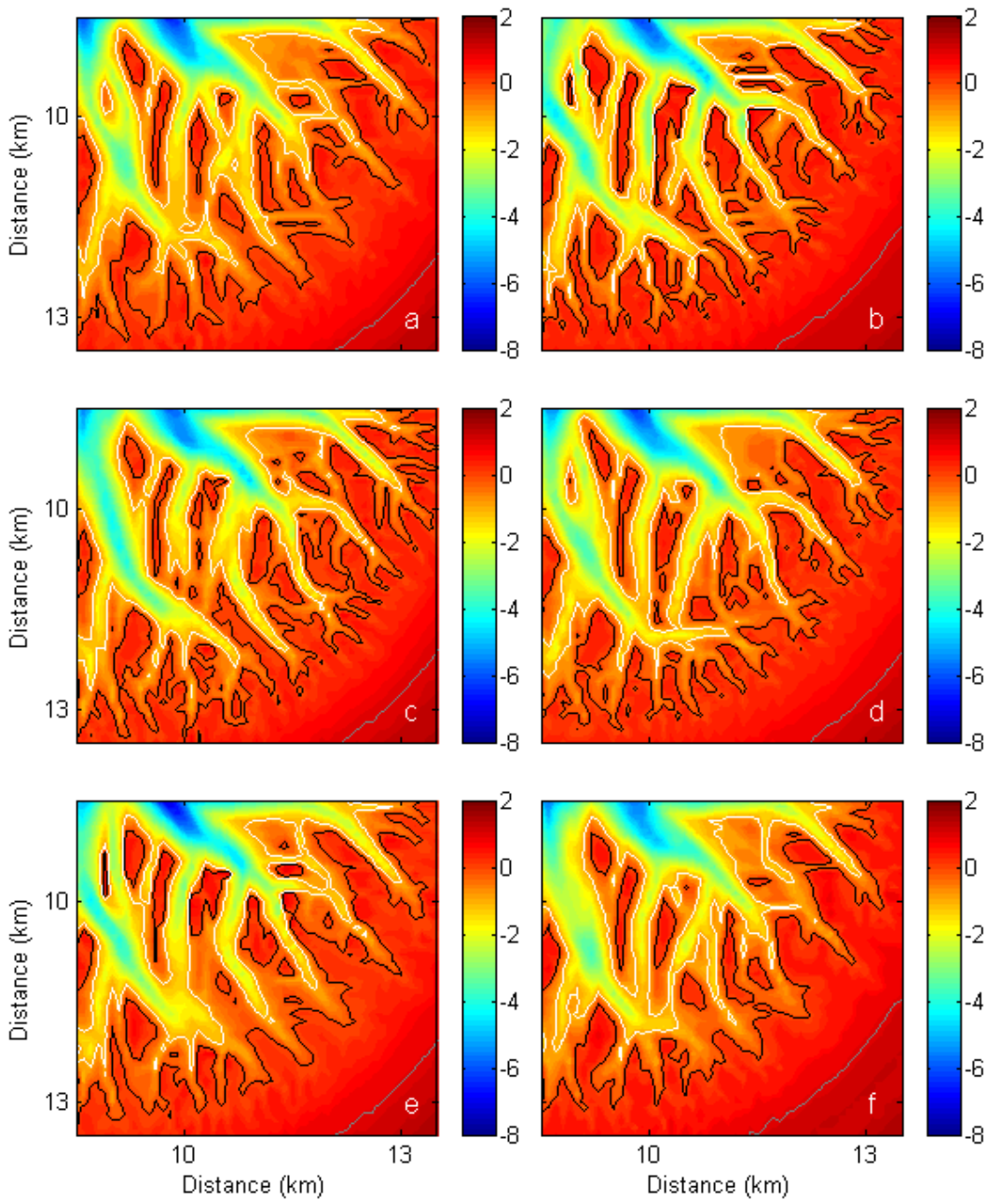

Figure 5.7. Part of the simulated morphology after 140 years (a) without mangroves (similar to Fig. 5.2a), (b) with mangroves (similar to Fig. 5.2b), and when only the effect of mangroves on (c) C_D, (d) θ_{cr}, (e) S_{slope}, and (f) ΔZ_{org} was included. White, black, and grey lines represent -1 (low tide), 0 (mid tide), and 1 (high tide) m contour lines, respectively. The axis correspond to the axis of Fig. 5.2.

The computation of slope-driven sediment transport in vegetated areas was performed according to a reduced version of Equation (5.18): $S_{slope}=(\alpha-\beta)b$. Sediment fluxes were thus reduced by one order of magnitude where mangrove

trees were present, independent on the below-ground biomass. The difference in the number of channels between the unvegetated and vegetated scenarios is below three throughout the entire basin (Fig. 5.8c), indicating that the decrease in slope-driven sediment transport does not have a large effect on channel density. However, mangroves affect the cross-sectional shape of channels because the increase in bank stability allows for a steeper slope between the channels and the adjacent area covered by mangroves (compare Fig. 5.7a and e).

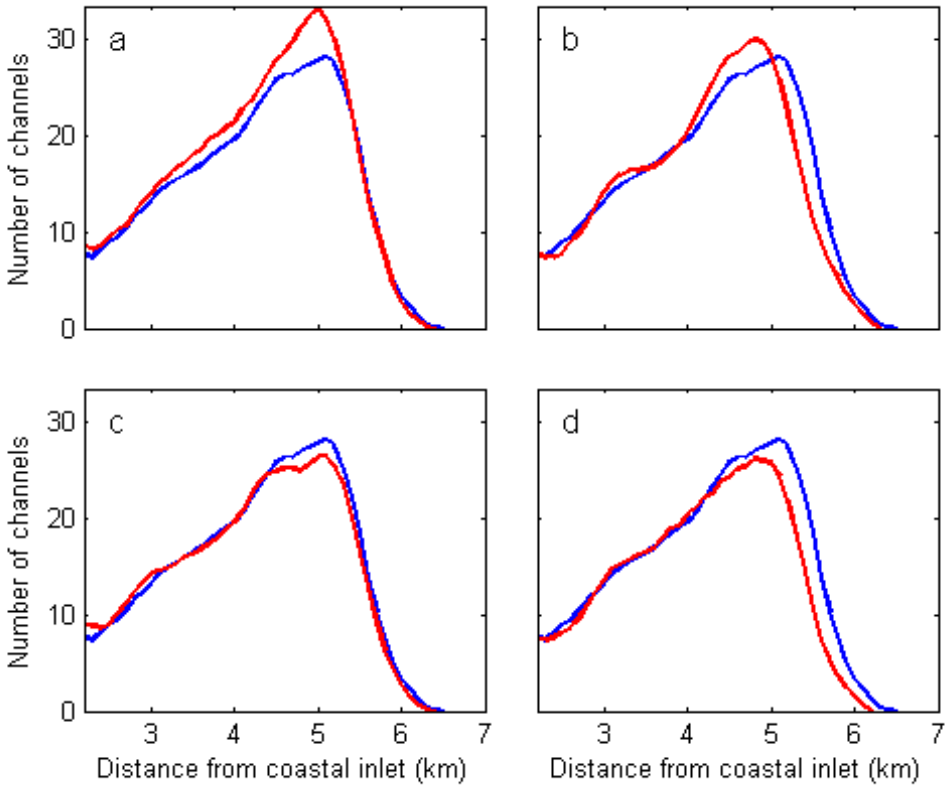

Figure 5.8. Number of channels versus distance from the coastal inlet for the unvegetated (blue) and vegetated (red) morphologies after 140 years. For the vegetated scenarios only the effect of mangroves on (a) C_D, (b) θ_{cr}, (c) S_{slope}, and (d) ΔZ_{org} was included. The number of channels is shown as a moving average over 500 m.

In the simulation for which only the production of organic matter was included we used a constant organic accumulation rate of 3.2 mm/year. The vertical growth of the vegetated areas reduced the volume of water stored on these vegetated platforms and thus reduced the tidal prism flowing through the tidal channels, altering tidal discharges. D'Alpaos et al. (2006) modelled the cross-sectional

evolution of tidal channels and showed that the reduced tidal prism after the emergence of a marsh platform caused infilling of the channel. We also see the importance of a reduction in the tidal prism on channel dynamics in our simulation since the branching of channels was hindered and the extent to which the channels could expand landward was reduced (Fig. 5.8d). The 0 m contour line (see Fig. 5.7f) does not occur as much landward as in the unvegetated scenario (Fig. 5.7a) and, over time, it retreats seaward due to the ongoing production of organic material and the associated reduction in tidal prism.

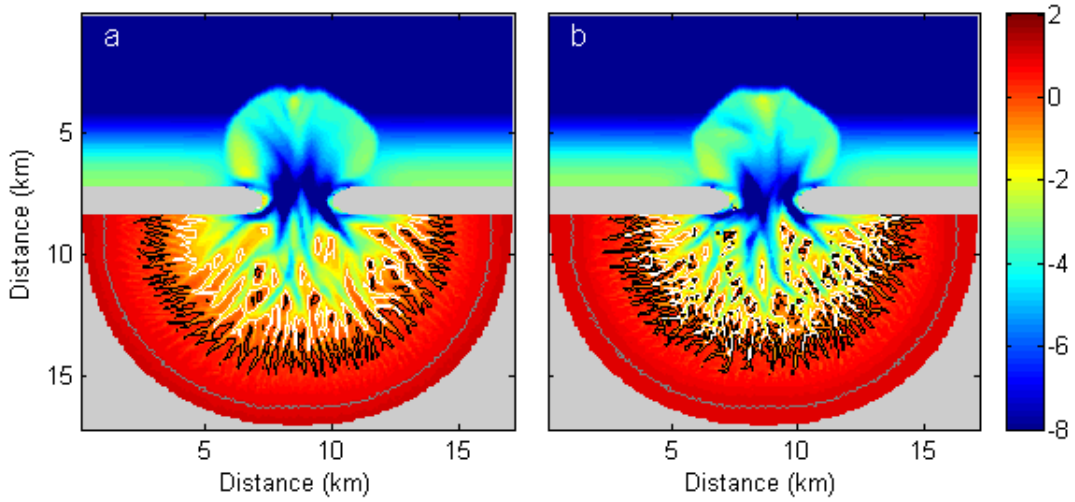

Figure 5.9. Simulated morphology after 160 years of sea level rise at a rate of 5.6 mm/year (a) without mangroves and (b) with mangroves. Sea level started to rise after 140 years of morphological evolution under a stable mean water level (the morphologies shown in Fig. 5.2). White, black, and grey lines represent -1 (low tide), 0 (mid tide), and 1 (high tide) m contour lines, respectively.

5.3.3 Morphological evolution under a rising sea-level

Sea level rise has a strong impact on tidal embayments and the morphological response of these systems to sea level rise may be significant. To explore the effects of mangroves on possible changes in the morphology and in the characteristics of the channel network we subjected the morphologies shown in Figure 5.2 to an increase in sea level at a rate of 5.6 mm/year (within the range of sea level rise estimates (IPCC, 2007)) for 160 years. Sea level rise resulted in enhanced deepening of the channels through the inlet in both the unvegetated and vegetated scenarios (Fig. 5.9). After 160 years of sea level rise the intertidal islands close to the inlet with a bed elevation above 0 m had disappeared in the

basin without mangroves while these areas, although they reduced in size, were still present in the vegetated basin. Mangroves thus enhanced the ability of the soil surface to maintain an elevation above mid tide which is sufficient to support mangrove growth. The hypsometric curves of the basins after sea level rise (Fig. 5.10) indicate that the proportion of bed elevations above 0 m is around 7% larger when mangroves are present. Mangroves also affected channel network evolution during sea level rise (Fig. 5.11). In the absence of mangroves the number of channels reduced between 3.3 and 4.9 km from the inlet, because the increase in water depth drove the channels to become larger and more widely-spaced. In the vegetated scenario, however, channels remained separated by intertidal areas covered with mangroves so that channel density remained more or less equal up to 4.7 km from the inlet. Headward erosion of the channels during sea level rise caused expansion of the channel network, alternating the topography of the area which was previously dry (Figs. 5.9 and 5.11). Where the channels expanded landward the number of channels increased more rapidly in the unvegetated basin than in the basin with mangroves. This indicates that the branching of channels is hindered when the channels expand into an area which is completely covered with mangroves. Furthermore, headward erosion of the channels was slowed down when channels had to carve through vegetated surfaces so that the channels cannot expand landward as much as in the unvegetated basin.

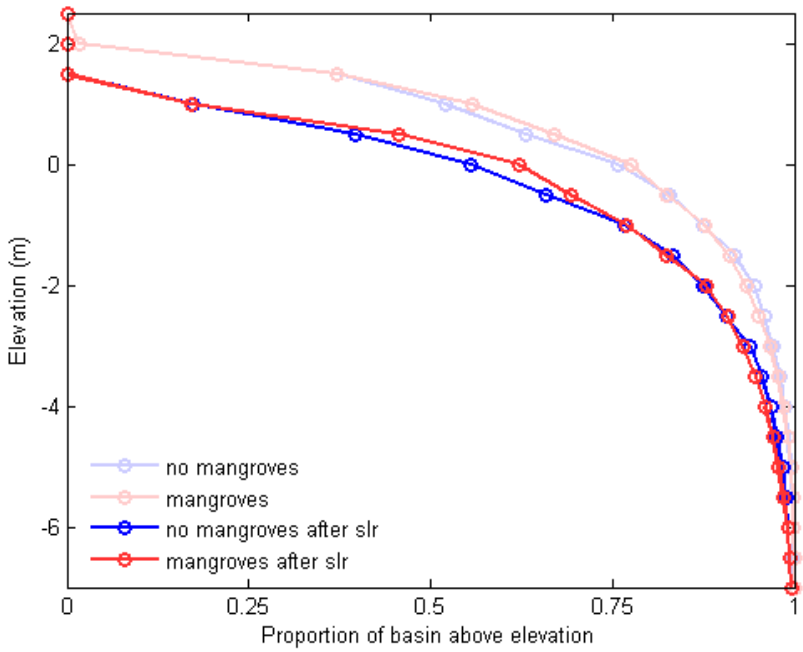

Figure 5.10. Hypsometric curves for the unvegetated and vegetated morphology before (Fig. 5.2) and after (Fig. 5.9) sea level rise.

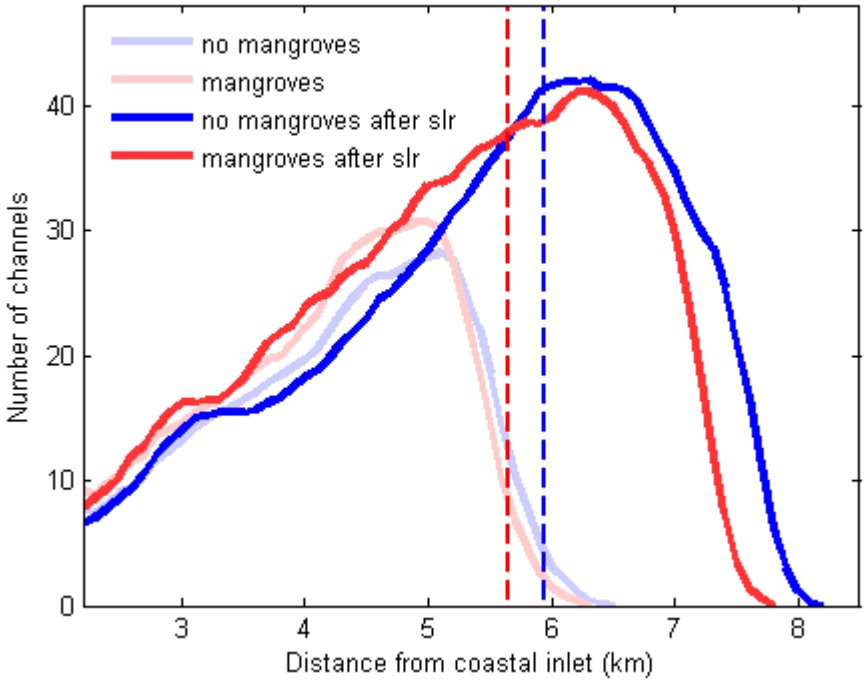

Figure 5.11. Number of channels versus distance from the coastal inlet for the unvegetated and vegetated morphology before (Fig. 5.2) and after (Fig. 5.9) sea level rise. The number of channels is shown as a moving average over 500 m. The vertical dashed blue and red lines represent the distance from the coastal inlet for which the bed elevation averages 0 m (mid tide) in respectively the unvegetated and vegetated scenario.

5.4 Discussion

The role of vegetation in determining channel density has been assessed for different environmental systems. For river systems, for example, both modelling studies (Murray and Paola, 2003) and laboratory experiments (Tal and Paola, 2010) demonstrated that vegetation can stabilize the morphology and lead to the development of a single channel instead of a rapidly changing, multiple channel pattern. Vegetation also affects the drainage density of landscapes experiencing continuous uplift (Istanbulluoglu and Bras, 2005). When the surface is covered with vegetation, the soil is protected against runoff so that landscape relief increases and drainage density decreases. In contrast, numerical modelling of channel formation on an initially bare tidal flat showed that channel drainage density increases with denser vegetation (Temmerman et al., 2007). We here examined how mangroves influence the morphological evolution and channel

density in tidal embayments. Our simulations indicate that vegetation can indeed lead to a larger channel density, because the erosion and therefore channel formation is enhanced in between vegetated areas. Channel development is thus accelerated in areas which are only partly vegetated. On the other hand, when the surface is completely covered with vegetation the feedback mechanism leading to enhanced flow concentration is not operating, the erosive power of the flow decreases and channel formation is slowed down.

The model results presented here provide useful insight into the effects of vegetation on channel network evolution. However, a number of assumptions were made throughout the development of the numerical model and included processes were simplified. General quantitative descriptions of the interactions between physics and biology are often lacking. The parameterizations used here to describe how mangroves affect physical processes and vice versa were based on previous studies performed by other authors combined with common and widely-accepted knowledge of the system. However, while these parameterizations capture the main processes governing the dynamics of mangrove environments in natural systems, some other features of the vegetation dynamics are neglected. The growth of mangroves, for example, is a complex process and tree growth may be constrained by salinity stress, availability of nutrients, and temperature. To keep the numerical model relatively simple and model output as transparent as possible we preferred to include only a minimum number of processes. The effects of these environmental factors on growth conditions were therefore not modelled in the present study. We decided to limit the growth of the mangrove trees only by the stresses caused by flooding and competition. Incorporating just these two stresses allow the numerical model to give rise to important behaviour typical of mangrove forests: the self-thinning process due to the competition among trees and the limited growth of the trees when they are inundated for long periods of time due to unfavourable anaerobic conditions. Mangroves died after continuous periods of limited tree growth. With respect to the dying of mangroves, it is worth mentioning that the assumption is made that the effects of mangroves on hydrodynamics and sediment dynamics completely disappear immediately after mangroves die. Another example of a complex process which is difficult to capture is the organic accretion. Organic accretion is the result of the

balance between the production and decomposition of organic material and field measurements indicated that this balance varies widely across different settings (McKee, 2011) and seasons. The study by McKee et al. (2007) revealed that the organic accumulation of mangroves in the Caribbean region actually closely-tracked sea level rise. This finding was suggested to be the result of flooding effects on the balance between subsurface root production and decomposition. Despite its complexity, we followed a relatively simple approach and linearly related the organic accretion rate with the below-ground biomass. Furthermore, mangroves produce organic matter while we addressed the morphological evolution of a tidal embayment consisting of non-cohesive sediment. Organic accumulation altered thus the sediment composition, but this effect was not included in the model.

Because of the way biophysical interactions were treated, the numerical model cannot be expected to be capable of simulating adequately the morphological evolution of a specific natural system. Although sensible, the parameterizations developed in this study are not necessarily accurate descriptions of the biophysical interactions occurring in nature. However, they do give rise to key differences in the channel network evolution of unvegetated and vegetated tidal basins. Our modelling approach is thus more aimed at exploring possible responses of the channel network to the presence of mangroves. The computational effort to perform these long-term morphological simulations (order of weeks to months) makes it infeasible, from a practical point of view, to conduct a detailed analysis of how model outcome responds to changes in parameter settings and in the way processes were parameterized.

The importance of including physical-biological interactions in morphodynamic models has recently been discussed as well as the need to derive quantitative representations of the interactions (Murray et al., 2008). Our model results show that mangroves play an important role in the morphological evolution of tidal embayments, further emphasizing the need to investigate biophysical feedback mechanisms. When more accurate parameterizations of the dynamics in tidal basins with mangroves become available they can be readily incorporated in the

present modelling approach, ultimately improving the quantitative aspect of these numerical simulations.

5.5 Conclusions

We developed a biomorphodynamic model to explore the effects of mangroves on the long-term evolution of tidal embayments. The model accounts for the effects of mangroves on hydrodynamics and sediment dynamics. In turn, hydrodynamic conditions affect the colonization, growth, and dying of mangroves so that a two-way coupling between physics and biology arises. A comparison between simulated morphologies without and with mangroves indicated that mangroves have a strong control on tidal channel network evolution. The enhanced branching of tidal channels in the presence of mangroves, which results in a higher channel density, is mainly caused by the extra drag produced by the trees and its pneumatophores (above-ground roots). The extra flow resistance in mangrove forests drives flow concentration and sediment erosion in between vegetated areas and thus enhances the formation of channels. The increase in the erosion threshold when the surface is covered with mangroves has contrasting effects. The process of channel branching is again enhanced, although the effect is less strong than with the higher drag. On the other hand, headward erosion of the channels is reduced so that channel density decreases in the upper part of the tidal embayment. The accumulation of organic matter leads to a reduction in the tidal prism which flows through the channels, ultimately reducing the extent to which the channels can expand landward. The decrease in slope-driven sediment transport in areas with mangroves allows the channel banks to become steeper, but does not have a large effect on channel density. Simulated morphological evolution under a rising mean water level indicated that channel networks expand landward during sea level rise. However, when channels have to expand into an area covered with mangroves, channel formation is hindered which decreases both the branching and headward erosion of channels. Moreover, when mangroves are present a larger area of the basin remains present above mid tide so that existing channels can not easily become larger and more widely-spaced. Overall, the model simulations presented here highlight the role of mangroves in the morphological evolution of tidal embayments and further emphasize the need to include biophysical interactions in morphodynamic models.

Chapter 6

Conclusions and directions for future research

6.1 Conclusions

The four working chapters of this thesis contribute in different ways to the central theme of this research which was to improve our understanding of tidal embayment evolution. In the introduction of this thesis three research questions were defined and the answers to these questions are summarized here:

1. How do tidal range and initial bathymetry affect the morphological evolution of tidal embayments?

Variations in the tidal range and the depth of the initially unchannelized tidal basin led to a large variability in the way in which the morphology evolved. Tidal range and the depth of the basin controlled the time scale over which channels and intertidal areas developed. A morphodynamically-active situation occurs particularly in the case of a large tidal range and a shallow basin, leading to the rapid (order of 10^1-10^2 years) formation of a complex tidal channel network. Channel network formation slowed down when the tidal range decreased and/or when the basin depth increased. For a deep tidal basin and a large tidal range, large volumes of sediment were transported into the basin associated with strong flow accelerations through the inlet of the system. In this case, channels did not immediately develop because of the large water depths. A flood-tidal delta formed instead which eventually became incised by channels and, ultimately (after 10^3-10^4 years), a complete channel network developed. However, the combination of a deep tidal basin and a small tidal range caused the morphology of the tidal basin to evolve slowly and an underdeveloped channel network remained present over long time scales (>10^4 years).

2. How do tidal embayments respond to sea level rise?

Sea level rise had a strong impact on tidal embayments and the morphology responded to the change in environmental forcing conditions. Currents redistributed the sediment during sea level rise such that intertidal geometry adjusted to the new hydrodynamic conditions. The channel network expanded landward because of headward erosion of the channels. Increasing water depths caused the existing channels to become larger and more widely-spaced. Sea level rise thus drove a landward shift of the channel network. Furthermore, rising water levels can induce a change in the asymmetry between the flood and ebb tidal currents and potentially lead to a transition from exporting to importing sediment. Even when the sea level stopped rising, the channel network continued to shift landward and the size, shape, and location of intertidal areas kept on changing.

3. How do mangroves affect the morphological evolution of tidal embayments?

Mangroves had a strong control on tidal channel network evolution and affected channel density. The branching of channels was enhanced when mangroves were present which was mainly caused by the additional resistance offered to the tidal flow by the mangroves and their roots. The extra drag drives flow concentration and sediment erosion in between vegetated areas so that channels form more rapidly. The extent to which channels expanded landward, which determines channel density in the upper part of the basin, was reduced by both the increase in erosion threshold and the accumulation of organic matter. Mangroves increased the ability of areas to maintain an elevation above mid tide under a rising sea level. In addition, the presence of mangroves affected how the channel network expanded landward during sea level rise because the branching as well as the headward erosion of the expanding channels was reduced.

Overall, the model simulations conducted as part of this study indicate that morphodynamic interactions play a crucial role in shaping the morphology of tidal embayments. When mangroves are present, another level of complexity is added

to the system and these mangroves, as shown by the modelling, control essential details of the evolving morphology.

6.2 Directions for future research

The results presented here highlight the potential of these numerical models, which are capable of simulating morphological behaviour over large spatial and temporal scales, to improve our knowledge of tidal systems. It is likely that this type of modelling approach will become widely-used in coming years. One should bear in mind though that these models are sensitive to many aspects of model development. Extreme care must be taken that subjective choices do not feedback and control the ultimate pattern development. Because of the large scales involved, and potential simplifications adopted throughout the development of the model, it is difficult to test model results directly against field observations. Misleading predictions of the future morphology of tidal systems will lead to false management and policy decisions and, ultimately, negatively impact the public perception of scientific predictions. New measures and methods must be continuously devised to facilitate model validation which, in the end, will increase our faith in model predictions.

The numerical model developed here is, as emphasized throughout this thesis, not intended to produce quantitatively accurate predictions of real tidal systems. Only a limited number of processes and interactions were included and they were treated in simplified ways. The model can therefore be considered as an "exploratory model" (Murray, 2003) which aims at determining the mechanisms and associated timescales that are essential in producing typical behaviour of, in this case, tidal embayments. Along the same philosophical pathway, the model could potentially be expanded to explore how the long-term morphological behaviour of tidal embayments is influenced by waves, river input, sediment mixtures, benthic organisms, human activities, or the overall geometry of the tidal basin, to just name a few. The 3 dimensional capability of the model is present, but was never used in the applications covered in this thesis. A different direction for future research involves implementing more accurate descriptions and parameterizations, attained by for example laboratory or field experiments, of the processes and interactions already included in the model. When the goal is to

build a “simulation model” (Murray, 2003), so that the behaviour of a specific natural system can be reproduced in a quantitatively precise way, it is necessary to include the full range of governing processes as well as to represent them as accurately as possible. Overall, it seems like mathematical modelling provides excellent ways to deepen our understanding of the evolution of tidal embayments.

References

Baas, A.C.W., 2002. Chaos, fractals and self-organization in coastal geomorphology: simulating dune landscapes in vegetated environments. *Geomorphology* 48, 309-328.

Berger, U., and Hildenbrandt, H., 2000. A new approach to spatially explicit modelling of forest dynamics: spacing, ageing and neighbourhood competition of mangrove trees. *Ecological Modelling* 132, 287-302.

Blum, M.D., and Roberts, H.H., 2009. Drowning of the Mississippi Delta due to insufficient sediment supply and global sea-level rise. *Nature Geoscience* 2, 488-491.

Cayocca, F., 2001. Long-term morphological modeling of a tidal inlet: the Arcachon Basin, France. *Coastal Engineering* 42, 115-142.

Chen, R., and Twilley, R.R., 1998. A gap dynamic model of mangrove forest development along gradients of soil salinity and nutrient resources. *Journal of Ecology* 86, 37-51.

Clarke, P.J., 1993. Dispersal of grey mangrove (*Avicennia marina*) propagules in southeastern Australia. *Aquatic Botany* 45, 195-204.

Clarke, P.J., and Myerscough, P.J., 1993. The intertidal distribution of the grey mangrove (Avicennia marina) in southeastern Australia: The effects of physical conditions, interspecific competition, and predation on propagule establishment and survival. *Australian Journal of Ecology* 18, 307-315.

Coco, G., and Murray, A.B., 2007. Patterns in the sand: from forcing templates to self-organization. *Geomorphology* 91, 271-290.

Cohen, J.E., Small, C., Mellinger, A., Gallup, J., and Sachs, J., 1997. Estimates of coastal populations. *Science* 278, 1209-1213.

Comley, B.W.T., and McGuinness, K.A., 2005. Above- and below-ground biomass, and allometry, of four common northern Australian mangroves. *Australian Journal of Botany* 53, 431-436.

Craft, C., Clough, J., Ehman, J., Joye, S., Park, R., Pennings, S., Guo, H., and Machmuller, M., 2009. Forecasting the effects of accelerated sea-level rise on tidal marsh ecosystem services. *Frontiers in Ecology and the Environment* 7, 73-78.

Daanen, R.P., Misra, D., Epstein, H., Walker, D., and Romanovsky, V., 2008. Simulating nonsorted circle development in arctic tundra ecosystems. *Journal of Geophysical Research* 113, G03S06.

D'Alpaos, A., Lanzoni, S., Marani, M., Fagherazzi, S., and Rinaldo, A., 2005. Tidal network ontogeny: Channel initiation and early development. *Journal of Geophysical Research* 110, F02001.

D'Alpaos, A., Lanzoni, S., Mudd, S.M., and Fagherazzi, S., 2006. Modeling the influence of hydroperiod and vegetation on the cross-sectional formation of tidal channels. *Estuarine, Coastal and Shelf Science* 69, 311-324.

D'Alpaos, A., Lanzoni, S., Marani, M., and Rinaldo, A., 2007a. Landscape evolution in tidal embayments: Modeling the interplay of erosion, sedimentation, and vegetation dynamics. *Journal of Geophysical Research* 112, F01008.

D'Alpaos, A., Lanzoni, S., Marani, M., Bonometto, A., Cecconi, G., and Rinaldo, A., 2007b. Spontaneous tidal network formation within a constructed salt marsh: Observations and morphodynamic modelling. *Geomorphology* 91, 186-197.

Daniels, R.C., White, T.W., and Chapman, K.K., 1993. Sea-level rise: destruction of threatened and endangered species habitat in South Carolina. *Environmental Management* 17, 373-385.

Deltacommissie, 2008. *Working Together with Water. A Living Land Builds for its Future. Findings of the Deltacommissie 2008*, 138 pp.

De Swart, H.E., and Zimmerman, J.T.F., 2009. Morphodynamics of tidal inlet systems. *Annual Review of Fluid Mechanics* 41, 203-229.

Di Silvio, G., Dall'Angelo, C., Bonaldo, D., and Fasolato, G., 2010. Long-term model of planimetric and bathymetric evolution of a tidal lagoon. *Continental Shelf Research* 30, 894-903.

Dissanayake, D.M.P.K., Roelvink, J.A., and van der Wegen, M., 2009. Modelled channel patterns in a schematized tidal inlet. *Coastal Engineering* 56, 1069-1083.

Dronkers, J., 2005. *Dynamics of Coastal Systems*. World Scientific, Singapore, 519 pp.

Duke, N.C., 1990. Phenological trends with latitude in the mangrove tree *Avicennia marina*. *Journal of Ecology* 78, 113-133.

Duke, N.C., Meynecke, J.-O., Dittmann, S., Ellison, A.M., Anger, K., Berger, U., Cannicci, S., Diele, K., Ewel, K.C., Field, C.D., Koedam, N., Lee, S.Y., Marchand, C., Nordhaus, I., Dahdouh-Guebas, F., 2007. A world without mangroves? *Science* 317, 41-42.

Engelund, F., and Hansen, E., 1967. *A Monograph on Sediment Transport in Alluvial Streams*. Teknisk Forlag, Copenhagen, 62 pp.

French, J.R., 2008. Hydrodynamic modelling of estuarine flood defence realignment as and adaptive management response to sea-level rise. *Journal of Coastal Research* 24, 1-12.

Friedrichs, C.T., and Aubrey, D.G., 1988. Non-linear tidal distortion in shallow well-mixed estuaries: a synthesis. *Estuarine, Coastal and Shelf Science* 27, 521-545.

Galbraith, H., Jones, R., Park, R., Clough, J., Herrod-Julius, S., Harrington, B., and Page, G., 2002. Global climate change and sea level rise: potential losses of intertidal habitat for shorebirds. *Waterbirds* 25, 173-183.

Gesch, D.B., 2009. Analysis of lidar elevation data for improved identification and delineation of lands vulnerable to sea-level rise. *Journal of Coastal Research* 53, 49-58.

Ginsberg, S.S., and Perillo, G.M.E., 2004. Characteristics of tidal channels in a mesotidal estuary of Argentina. *Journal of Coastal Research* 20, 489-497.

Hibma, A., De Vriend, H.J., and Stive, M.J.F., 2003. Numerical modelling of shoal pattern formation in well-mixed elongated estuaries. *Estuarine, Coastal and Shelf Science* 57, 981-991.

Hodges, B.R., 2000. *Numerical Techniques in CWR-ELCOM (code release v.1).* Centre for Water Research, The University of Western Australia.

Hodges, B.R., Imberger, J., Saggio, A., and Winters, K.B., 2000. Modeling basin-scale internal waves in a stratified lake. *Limnology and Oceanography* 45, 1603-1620.

Hogarth, P.J., 2007. *The biology of mangroves and seagrasses*. Oxford University Press, Oxford, 273 pp.

Hughes, Z.J., FitzGerald, D.M., Wilson, C.A., Pennings, S.C., Wieski, K., and Mahadevan, A., 2009. Rapid headward erosion of marsh creeks in response to relative sea level rise. *Geophysical Research Letters* 36, L03602.

IPCC, 2002. *Climate Change and Biodiversity. IPCC Technical Paper V*. IPCC, Geneva, 86 pp.

IPCC, 2007. *Climate Change 2007: The Physical Science Basis. Contribution of Working Group I to the Fourth Assessment Report of the Intergovernmental Panel on Climate Change*. Cambridge University Press, Cambridge, 996 pp.

Istanbulluoglu, E., and Bras, R.L., 2005. Vegetation-modulated landscape evolution: Effects of vegetation on landscape processes, drainage density, and topography. *Journal of Geophysical Research* 110, F02012.

Jelgersma, S., 1994. Examples of the geological past: evolution of coastal sedimentation sequences during Holocene sea level rise, *in* Pernetta, J.C., Leemans, R., Elder, D., and Humphrey, S., eds., *Impacts of Climate Change on Ecosystems and Species: Marine and Coastal Ecosystems*. IUCN, Gland, 45-57 pp.

Kirwan, M.L., and Murray, A.B., 2007. A coupled geomorphic and ecological model of tidal marsh evolution. *Proceedings of the National Academy of Sciences of the USA* 104, 6118-6122.

Koch, E.W., Barbier, E.B., Silliman, B.R., Reed, D.J., Perillo, G.M.E., Hacker, S.D., Granek, E.F., Primavera, J.H., Muthiga, N., Polasky, S., Halpern, B.S., Kennedy, C.J., Kappel, C.V., and Wolanski, E., 2009. Non-linearity in ecosystem services: temporal and spatial variability in coastal protection. *Frontiers in Ecology and the Environment* 7, 29-37.

Krauss, K.W., Lovelock, C.E., McKee, K.L., López-Hoffman, L., Ewe, S.M.L., and Sousa, W.P., 2008. Environmental drivers in mangrove establishment and early development: A review. *Aquatic Botany* 89, 105-127.

Küchler, A.W., 1972. The mangrove in New Zealand. *New Zealand Geographer* 28, 113-129.

Levin, L.A., Boesch, D.F., Covich, A., Dahm, C., Erséus, C., Ewel, K.C., Kneib, R.T., Moldenke, A., Palmer, M.A., Snelgrove, P., Strayer, D., and Weslawski, J.M., 2001. The function of marine critical transition zones and the importance of sediment biodiversity. *Ecosystems* 4, 430-451.

Long, W., Kirby, J.T., and Shao, Z., 2008. A numerical scheme for morphological bed level calculations. *Coastal Engineering* 55, 167-180.

Marani, M., D'Alpaos, A., Lanzoni, S., Carniello, L., and Rinaldo, A., 2010. The importance of being coupled: Stable states and catastrophic shifts in tidal biomorphodynamics. *Journal of Geophysical Research* 115, F04004.

Marciano, R., Wang, Z.B., Hibma, A., de Vriend, H.J., and Defina, A., 2005. Modeling of channel patterns in short tidal basins. *Journal of Geophysical Research* 110, F01001.

Mariotti, G., and Fagherazzi, S., 2010. A numerical model for the coupled long-term evolution of salt marshes and tidal flats. *Journal of Geophysical Research* 115, F01004.

Mazda, Y., Wolanski, E., King, B., Sase, A., Ohtsuka, D., and Magi, M., 1997a. Drag force due to vegetation in mangrove swamps. *Mangroves and Salt Marshes* 1, 193-199.

Mazda, Y., Magi, M., Kogo, M., and Hong, P.N., 1997b. Mangroves as a coastal protection from waves in the Tong King delta, Vietnam. *Mangroves and Salt Marshes* 1, 127-135.

Mazda, Y., Kobashi, D., and Okada, S., 2005. Tidal-scale hydrodynamics within mangrove swamps. *Wetlands Ecology and Management* 13, 647-655.

Mazda, Y., Magi, M., Ikeda, Y., Kurokawa, T., and Asano, T., 2006. Wave reduction in a mangrove forest dominated by *Sonneratia* sp. *Wetlands Ecology and Management* 14, 365-378.

McKee, K.L., 2011. Biophysical controls on accretion and elevation change in Caribbean mangrove ecosystems. *Estuarine, Coastal and Shelf Science* 91, 475-483.

McKee, K.L., Cahoon, D.R., and Feller, I.C., 2007. Caribbean mangroves adjust to rising sea level through biotic controls on change in soil elevation. *Global Ecology and Biogeography* 16, 545-556.

Middleton, B.A., and McKee, K.L., 2001. Degradation of mangrove tissues and implications for peat formation in Belizean island forests. *Journal of Ecology* 89, 818-828.

Milliman, J.D., Broadus, J.M., and Gable, F., 1989. Environmental and economic implications of rising sea level and subsiding deltas: the Nile and Bengal examples. *Ambio* 18, 340-345.

Mitsch, W.J. and Gosselink, J.G., 2007. *Wetlands*. John Wiley & Sons, New York, 582 pp.

Morris, J.T., Sundareshwar, P.V., Nietch, C.T., Kjerfve, B., and Cahoon, D.R., 2002. Responses of coastal wetlands to rising sea level. *Ecology* 83, 2869-2877.

Murray, A.B., 2003. Contrasting the goals, strategies, and predictions associated with simplified numerical models and detailed simulations, *in* Wilcock, P.R., and Iverson, R.M., eds., *Prediction in Geomorphology, Geophysical Monograph* 135, AGU, Washington, D.C., 151-165 pp.

Murray, A.B., and Paola, C., 2003. Modelling the effect of vegetation on channel pattern in bedload rivers. *Earth Surface Processes and Landforms* 28, 131-143.

Murray, A.B., Knaapen, M.A.F., Tal, M., and Kirwan, M.L., 2008. Biomorphodynamics: physical-biological feedbacks that shape landscapes. *Water Resourches Research* 44, W11301.

Najjar, R.G., Walker, H.A., Anderson, P.J., Barron, E.J., Bord, R.J., Gibson, J.R., Kennedy, V.S., Knight, C.G., Megonigal, J.P., O'Connor, R.E., Polsky, C.D., Psuty, N.P., Richards, B.A., Sorenson, L.G., Steele, E.M., and Swanson, R.S., 2000. The potential impacts of climate change on the mid-Atlantic coastal region. *Climate Research* 14**,** 219-233.

Nepf, H.M., 1999. Drag, turbulence, and diffusion in flow through emergent vegetation. *Water Resources Research* 35, 479-489.

Nicholls, R.J., Hoozemans, F.M.J., and Marchand, M., 1999. Increasing flood risk and wetland losses due to global sea-level-rise: regional and global analyses. *Global Environmental Change* 9, S69-S87.

Passalacqua, P., Do Trung, T., Foufoula-Georgiou, E., Sapiro, G., and Dietrich, W. E., 2010. A geometric framework for channel network extraction from lidar: nonlinear diffusion and geodesic paths. *Journal of Geophysical Research* 115, F01002.

Pfeffer, W.T., Harper, J.T., and O'Neel, S., 2008, Kinematic constraints on glacier contributions to 21st-century sea-level rise. *Science* 321, 1340-1343.

Pilkey, O.H., and Cooper, J.A.G., 2004. Society and sea level rise: *Science* 303**,** 1781-1782.

Quartel, S., Kroon, A., Augustinus, P.G.E.F., van Santen, P., and Tri, N.H., 2007. Wave attenuation in coastal mangroves in the Red River Delta, Vietnam. *Journal of Asian Earth Sciences* 29, 576-584.

Rahmstorf, S., 2007. A semi-empirical approach to projecting future sea-level rise. *Science* 315, 368-370.

Reinhardt, L., Jerolmack, D., Cardinale, B.J., Vanacker, V., and Wright, J., 2010. Dynamic interactions of life and its landscape: feedbacks at the interface of geomorphology and ecology. *Earth Surface Processes and Landforms* 35, 78-101.

Roelvink, J.A., 2006. Coastal morphodynamic evolution techniques. *Coastal Engineering* 53, 277-287.

Schuttelaars, H.M., and de Swart, H.E., 1999. Initial formation of channels and shoals in a short tidal embayment. *Journal of Fluid Mechanics* 386, 15-42.

Stefanon, L., Carniello, L., D'Alpaos, A., and Lanzoni, S., 2010. Experimental analysis of tidal network growth and development. *Continental Shelf Research* 30, 950-962.

Swales, A., Bentley, S.J., Lovelock, C., and Bell, R.G., 2007. Sediment processes and mangrove-habitat expansion on a rapidly-prograding muddy coast, New Zealand. *Proceedings of Coastal Sediments*, ASCE, New York, pp. 1441-1454.

Tal, M., and Paola, C., 2010. Effects of vegetation on channel morphodynamics: results and insights from laboratory experiments. *Earth Surface Processes and Landforms* 35, 1014-1028.

Tambroni, N., Bolla Pittaluga, M., and Seminara, G., 2005. Laboratory observations of the morphodynamic evolution of tidal channels and tidal inlets. *Journal of Geophysical Research* 110, F04009.

Temmerman, S., Bouma, T.J., Govers, G., Wang, Z.B., de Vries, M.B., and Herman, P.M.J., 2005. Impact of vegetation on flow routing and sedimentation patterns: Three-dimensional modeling for a tidal marsh. *Journal of Geophysical Research* 110, F04019.

Temmerman, S., Bouma, T.J., Van de Koppel, J., Van der Wal, D., De Vries, M.B., and Herman, P.M.J., 2007. Vegetation causes channel erosion in a tidal landscape. *Geology* 35, 631-634.

Titus, J.G., and Richman, C., 2001. Maps of lands vulnerable to sea level rise: modeled elevations along the US Atlantic and Gulf coast. *Climate Research* 18, 205-228.

Tomlinson, P.B., 1986. *The botany of mangroves*. Cambridge University Press, Cambridge, 413 pp.

Van de Koppel, J., van der Wal, D., Bakker, J.P., and Herman, P.M.J., 2005. Self-organization and vegetation collapse in salt marsh ecosystems. *The American Naturalist* 165, E1-E12.

Van der Wegen, M., and Roelvink, J.A., 2008. Long-term morphodynamic evolution of a tidal embayment using a two-dimensional, process-based model. *Journal of Geophysical Research* 113, C03016.

Van der Wegen, M., Wang, Z.B., Savenije, H.H.G., and Roelvink, J.A., 2008. Long-term morphodynamic evolution and energy dissipation in a coastal plain, tidal embayment. *Journal of Geophysical Research* 113, F03001.

Van Rijn, L.C., 1984. Sediment transport, part II: suspended load transport. *Journal of Hydraulic Engineering* 110, 1613-1641.

Van Santen, P., Augustinus, P.G.E.F., Janssen-Stelder, B.M., Quartel, S., and Tri, N.H., 2007. Sedimentation in an estuarine mangrove system. *Journal of Asian Earth Sciences* 29, 566-575.

Vitousek, P.M., Mooney, H.A., Lubchenco, J., and Melillo, J.M., 1997. Human domination of earth's ecosystems. *Science* 277, 494-499.

Appendix A

The use of artificial neural networks to analyze and predict alongshore sediment transport

Abstract

An artificial neural network (ANN) was developed to predict the depth-integrated alongshore suspended sediment transport rate using 4 input variables (water depth, wave height and period, and alongshore velocity). The ANN was trained and validated using a dataset obtained on the intertidal beach of Egmond aan Zee, the Netherlands. Root-mean-square deviation between observations and predictions was calculated to show that, for this specific dataset, the ANN (ε_{rms}=0.43) outperforms the commonly used Bailard (1981) formula (ε_{rms}=1.63), even when this formula is calibrated (ε_{rms}=0.66). Because of correlations between input variables, the predictive quality of the ANN can be improved further by considering only 3 out of the 4 available input variables (ε_{rms}=0.39). Finally, we use the partial derivatives method to "open and lighten" the generated ANNs with the purpose of showing that, although specific to the dataset in question, they are not "black-box" type models and can be used to analyze the physical processes associated with alongshore sediment transport. In this case, the alongshore component of the velocity, by itself or in combination with other input variables, has the largest explanatory power. Moreover, the behaviour of the ANN indicates that predictions can be unphysical and therefore unreliable when the input lies outside the parameter space over which the ANN has been developed. Our approach of combining the strong predictive power of ANNs with "lightening" the black box and testing its sensitivity, demonstrates that the use of an ANN approach can result in the development of generalized models of suspended sediment transport.

Publication:

Van Maanen, B., Coco, G., Bryan, K.R., and Ruessink, B.G., 2010. The use of artificial neural networks to analyze and predict alongshore sediment transport. Nonlinear Processes in Geophysics 17, 395-404.

A.1 Introduction

Alongshore sediment transport can have large-scale and long-term effects on coastal evolution and plays therefore a key role in nearshore studies and is of interest to scientists, managers, and engineers. Understanding and predicting sediment transport in the surfzone has proven to be extremely difficult because of the energetic environment and the complexity of nearshore systems and sediment transport itself. Both observational and theoretical approaches have been used to study sediment transport. From an observational point of view, obtaining accurate measurements of suspended sediment concentrations remains a challenge primarily because of its sensitivity to air bubbles (Puleo et al., 2006) and mixtures of sediments (Green and Boon, 1993), or the uncertain vertical position of the sensors with respect to the seabed. Semi-empirical (or semi-theoretical) models (e.g. Bailard, 1981) that account for the effect of waves and currents have also been developed but their application to natural conditions has shown only limited success (e.g. van Maanen et al., 2009). Practically, all of the theoretical approaches need a specific field calibration to tune the many parameters present in the models so that essentially, despite decades of research, making reliable predictions of sediment transport remains a difficult task.

A commonly adopted alongshore transport equation has been developed by Bailard (1981) who suggested that the work done in transporting the sediment is a fixed portion of the total energy dissipated by the flow. Depth-integrated alongshore suspended sediment (kg/m/s) is given by:

$$\left\langle q_{ysB}(t)\right\rangle = \rho_s k_s \left(< \left|\vec{U}(t)\right|^3 v > + < \left|\vec{U}(t)\right|^3 v^* > \right) \quad \text{(A.1)}$$

where the angle brackets indicate time-averaging over many waves, $\vec{U}$ (t) represents the instantaneous velocity vector, v is the time-averaged alongshore velocity, v^* is the alongshore orbital velocity, and

$$k_s = \frac{\rho}{(\rho_s - \rho)g} c_f \frac{\varepsilon_s}{w_s} \quad \text{(A.2)}$$

where c_f is the bed drag coefficient, ε_s is an efficiency factor, and w_s is the settling speed of the characteristic grain size. Similar predictors have been proposed by other authors (see Bayram et al., 2001 for a thorough review) but their success is limited, especially during storms, and a specific calibration is often required (Bayram et al., 2001).

A different approach is provided by data-driven models. The simplest example of a data-driven model is provided by a linear regression where a single input variable (e.g. wave height) is used to provide an estimate of the predicted variable (e.g. sediment transport rate). Many different (and more complicated) data-driven algorithms have been developed and Artificial Neural Networks (ANNs) are an excellent example of such algorithms. ANNs have been applied to several fields of science (see for example Gardner and Dorling, 1998; Dayhoff and DeLeo, 2001) and several applications exist also in the field of ocean and coastal engineering. For example, ANNs have been applied to develop forecasts of hydrodynamics at different scales ranging from nearshore waves (Browne et al., 2007) to tides (Tsai and Lee, 1999) and storms (Sztobryn, 2003). Furthermore, for the case of unidirectional flow, ANNs have also been successfully used to predict sediment concentrations in laboratory (Lin and Namin, 2005) and field (Nagy et al., 2002) studies. ANNs are also beginning to be applied to the study of sandbar dynamics (Kingston et al., 2000) and beach profile evolution (Tsai et al., 2000). These studies have all treated ANNs as a black-box focusing primarily on its predictive capability with little emphasis on increasing understanding of the driving physical processes. In few cases, ANNs have also been successfully used to explore the role of nonlinearities of a system including time-lag and scale effects (Pape et al., 2007). Finally, ANNs have also been applied in the field of geophysics and oceanography (Krasnopolsky, 2007) to develop hybrid models that combine ANNs and partial differential equations based on first principles (e.g. mass and momentum conservation). Overall, it appears that ANNs are becoming more and more common tools in geophysical and oceanographic studies but clearly they are still not used to fulfill their whole potential.

In this contribution we use field observations to train ANNs and show that, for the present dataset, ANNs can provide better predictions of alongshore suspended

sediment transport rate than the commonly used Bailard (1981) formula. We also "open and lighten" the black-box to show that ANNs can be used to analyze the physical processes associated with suspended sediment transport. This approach is valuable because the usefulness of ANNs beyond their predictive power has often been the subject of discussion (McCann, 1992; Gardner and Dorling, 1998) and also because it demonstrates that using an ANN approach can result in the development of generalized models of suspended sediment transport.

A.2 Methods

A.2.1 Field Measurements

A field experiment was conducted at Egmond aan Zee (the Netherlands), a sandy (median size equal to 0.3 mm) beach characterized during the field experiment by one intertidal and two subtidal sandbars. Four tripods were deployed shoreward of the intertidal sandbar and each tripod included an electromagnetic flow velocity meter (EMF), a pressure sensor, and three optical backscatter (OBS) sensors. While tripods were submerged, timeseries were recorded continuously and subsequently split in 15 minutes bursts. Sampling frequency for all instruments was 2Hz. A detailed description of the field experiment including collection and analysis techniques of hydrodynamic and suspended sediment data has been presented previously (van Maanen et al., 2009).

Data from the pressure sensors were used to obtain spectral wave height H_{m0}, peak period T_p, and water depth h. Timeseries collected using the EMF were used to derive the burst- and depth-averaged alongshore velocity V (for details see van Maanen et al., 2009). With respect to the suspended sediment concentrations, OBSs were calibrated using sand collected at the field site and data were used to construct the vertical profiles of suspended sediment concentration (for details see van Maanen et al., 2009). Finally, the depth-integrated suspended load was derived by integrating over the water depth, for each burst, the product between velocity and suspended sediment concentration profiles. The data used throughout this study are shown in Fig. A.1.

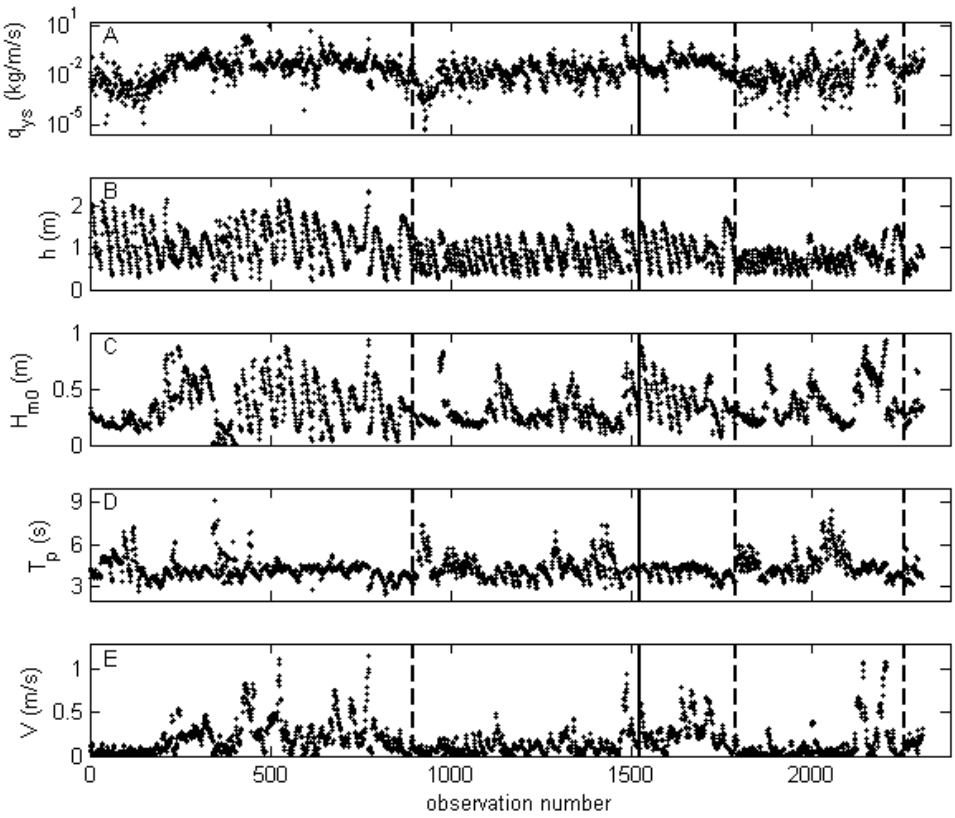

Figure A.1. Tripod observations: (A) Depth-integrated suspended sediment transport (a log-scale is employed), (B) water depth, (C) significant wave height, (D) peak wave period, (E) alongshore velocity. The vertical dashed lines separate data obtained from different tripods (tripods were measuring simultaneously, but each dataset is characterized by a different length because of the different time that each tripod was submerged). The vertical solid lines at observation 1522 indicate the difference between the "training" (first 66% of the data) and the "testing" (last 33% of the data) datasets.

A.2.2 Artificial Neural Network Background and Architecture

Over the last few decades, development and continuous improvement of ANNs have resulted in a powerful predictive tool. A major advancement was achieved by Werbos (1974) who expanded the applicability of ANNs to nonlinear systems and this development formed the basis of many ANNs used today. An ANN consists of input, hidden, and output nodes arranged in layers (Fig. A.2). The input layer is usually "non-neural" in the sense that it only serves to feed the input data to the network. Each input is connected to a number of neurons, which

altogether constitute the hidden layer. Here, information from input variables is condensed after performing operations of the type

$$h_j = f \cdot \left(a_j + \sum_{i=1}^{n} w_i x_i \right) \quad \text{(A.3)}$$

where x_i is the i^{th} input variable, h_j represents the response of the j^{th} neuron in the hidden layer, f is the activation function (a sigmoid has been used throughout this study similar for example to Rumelhart et al., 1986), w_i is the connection weight between x_i and h_j, a_j is the bias for the j^{th} hidden neuron, and there are n input variables. A further combination of hidden nodes, which is achieved by means of a new activation function (again a sigmoid) and new connection weights and biases, results in the output layer (in this study the output layer corresponds to one single value, the depth-integrated suspended sediment load).

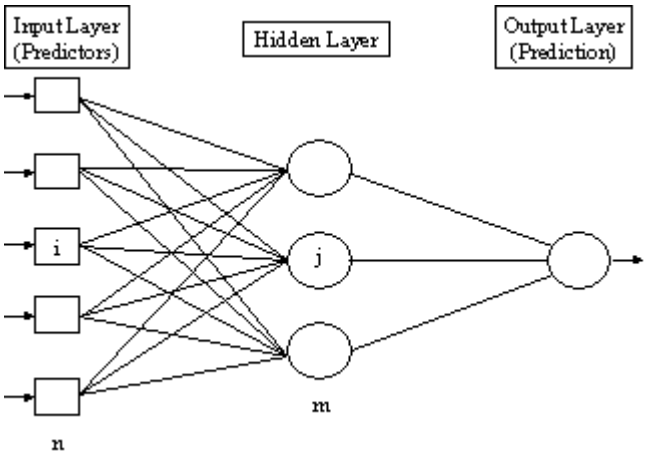

Figure A.2. An idealized feed-forward ANN characterized by n input nodes (the predictors or independent variables), m hidden nodes and one output node (the prediction or dependent variable).

The biases and connection weights of the ANN are evaluated through an optimization process that starts by splitting the dataset into two parts: the training dataset and the validation dataset. Training data are used by the ANN to learn how the system behaves, a process which ultimately results in the specification of biases and weights. Validation data are used to assess the performance of the ANN in making predictions. We used 66% (corresponding to 1522 observations)

of the dataset to train the ANN, and the remaining part (784 observations) for validation. For this study, we used the most common type of feed-forward ANN that consists of one hidden layer with training performed using the Levenberg-Marquardt backpropagation algorithm (other backpropagation algorithms have been tried but none of them resulted in a statistically significant improvement). Training algorithms, especially for the backpropagation case (Kolen and Pollack, 1990), can be extremely sensitive to the initial values assigned to biases and weights. In trying to determine the biases and weights resulting in the global minimum of the difference between observations and ANN predictions, local minima may be encountered (whose presence depends on the initial values assigned to biases and weights) which halt the optimization process. There is no clear solution to this problem, which is why most authors prefer to train ANNs using different random seeds to generate initial weights and then analyze the best ANN (Faraway and Chatfield, 1998). For this study we adopted this approach and generated 10,000 ANNs with different initial random seeds. Results presented in this contribution refer to the ANN that displayed the lowest error herein defined as the root-mean-square deviation (Bayram et al., 2001; van Maanen et al., 2009):

$$\varepsilon_{rms} = \left[\frac{\sum_1^N \left(\log(q_{ysP}) - \log(q_{ysF}) \right)^2}{N-1} \right]^{0.5} \qquad \text{(A.4)}$$

where the subscripts *P* and *F* respectively refer to the values predicted by the ANN (the same parameter is used to evaluate the goodness of fit of the Bailard (1981) formula) and the values measured in the field. Also, to avoid overfitting of the training dataset, we have used a typical early-stopping technique such that if the performance of the training parameters (weights and biases) on the validation dataset does not improve, the optimization process is stopped and no new weights and biases are generated.

In this study, we have considered ANNs with the simplest structure: a number of hidden nodes ranging from 2 to 8 and only one hidden layer. Faraway and Chatfield (1998) showed that increasing the number of nodes can sometimes cause ANN performance to decay (overtraining). The likelihood of overtraining is

obviously related to the ratio between the number of free parameters in the model (biases and weights) and the number of training samples. As each dataset has different characteristics, no clear guideline exists on how many samples are needed to avoid overtraining. The general rule (valid also for multiple linear regression) is that the number of training samples (1522 in the present study) should be at least 10 times the number of free parameters (Burnham and Anderson, 2002), so that the present training dataset should not be prone to overtraining issues.

The sigmoid activation function, defined as:

$$f(x) = \frac{1}{1+e^{-x}} \qquad \text{(A.5)}$$

requires transforming the dependent variable (the prediction target or output) in both the training and validation datasets into a value inside the range [0 1] (the sigmoid function contracts any input inside this range). Variable transformation has been achieved by:

$$y_k^* = \frac{y_k - \min(y)}{\max(y) - \min(y)} \qquad \text{(A.6)}$$

where y_k* is the transform of y_k which, in turn, is the k^{th} observation of the dependent variable y. min(y) and max(y) are the minimum and maximum values of y, respectively. When evaluating the error associated with the ANN predictions, the dependent variable is transformed back into original values. Input variables vary over different ranges and need to be standardized to facilitate post-processing of the ANN and analysis of variable importance. Following Dimopoulos et al. (1999), this is achieved by:

$$x_k^* = (x_k - x_{mean}) / \sigma_x \qquad \text{(A.7)}$$

where x_k* is the standardized value of independent variable x_k, which, in turn, is the k^{th} observation of independent variable x. x_{mean} and σ_x are the mean and

standard deviation of x, respectively. Subsequently, the standardized values of the input variables are also normalized according to Eq. (A.6).

A.2.3 Opening and Lightening the "black box"

Despite the presence of studies showing how ANNs can be used to increase understanding of physical processes (e.g. Pape et al., 2007), ANNs are often considered to be "black boxes" with little, if any, capacity to provide insight on the dataset from which they have been constructed. However, for more than a decade techniques have been suggested that allow detailed analysis of connection weights and estimation of the role of each input variable (Vaughn, 1996; Benítez, 1997; Dimopoulos et al., 1999; Olden, 2000; Olden and Jackson, 2002). Recently, some of the techniques available have also been reviewed (Gevrey et al., 2003; Olden et al., 2004) and the partial derivatives (PaD) method has been shown to have the best explanatory power. The PaD approach was originally proposed by Dimopoulos et al. (1995) and recently extended by Gevrey et al. (2006). Assuming the use of a sigmoid activation function for all connections between nodes (as in the present study) and considering a network constituted by n input variables, one single hidden layer with m nodes and one output, the sensitivity of the ANN output to the input variable x_i is evaluated through the sum of the squared partial derivatives *SSD* (Dimopoulos et al., 1995):

$$SSD_i = \sum_{k=1}^{N} d_{ki}^2 \qquad \text{(A.8)}$$

where the index i refers to the input variable, the index k refers to the N available observations of the testing dataset. Assuming m hidden nodes, the derivative of output node k with respect to input variable i is evaluated as:

$$d_{ki} = S_k \sum_{j=1}^{m} w_{jo} I_{jk} \left(1 - I_{jk}\right) w_{ij} \qquad \text{(A.9)}$$

where w_{ij} is the weight connecting the i^{th} input node and the j^{th} hidden node, w_{jo} is the weight connecting the output and the j^{th} hidden node, S_k is the derivative of the output node with respect to its input, and I_{jk} is the response of the j^{th} hidden node

for the k^{th} input (for more details see Dimopoulos et al., 1995). Once SSD_i has been calculated for each input variable, one can compare values and establish which variable is relatively the most important. The larger the value of SSD_i, the more influence input variable x_i has on the output.

Using a similar approach, the importance of pair-wise combinations of input variables has also been evaluated (Gevrey et al., 2006):

$$d_{k12} = S_k \left[s_k \sum_{j=1}^{m} w_{1j} w_{jo} I_{jk} \left(1 - I_{jk}\right) \sum_{j=1}^{m} w_{2j} w_{jo} I_{jk} \left(1 - I_{jk}\right) + \sum_{j=1}^{m} w_{1j} w_{2j} w_{jo} I_{jk} \left(1 - I_{jk}\right)\left(1 - 2I_{jk}\right) \right] \quad \text{(A.10)}$$

where all symbols have been previously indicated apart from s_k which is the second derivative of the output node with respect to its input. As for the case of individual variables, the relative contribution of pairs of variables to the ANN explicatory power can be evaluated as:

$$SSD_{12} = \sum_{k=1}^{N} d_{k12}^2 \quad \text{(A.11)}$$

A.3 Results

For the present study we decided to compare the predictive capability of ANNs and the Bailard model since van Maanen et al. (2009) found that the Bailard model outperformed another commonly used alongshore transport model (van Rijn, 1984) when the entire dataset was being evaluated. Also, the Bailard formula allows for an easy calibration procedure. We initially evaluated the performance of the Bailard model on the testing dataset (Fig. A.3) which was not satisfactory given the large scatter of the data and the overall underprediction of depth-integrated suspended sediment transport (ε_{rms}=1.63). The Bailard formula (Eqs. A.1 and A.2) involves two coefficients, the drag coefficient and the efficiency factor, whose values are difficult to establish unequivocally. In this study we used 0.003 and 0.02, respectively, following van Maanen et al. (2009). We then decided, consistently with the ANN approach, to calibrate the Bailard

formula on the training dataset and then apply the calibration coefficient to the testing dataset. Best agreement between measurements and predictions was obtained after multiplying the uncalibrated Bailard predictions by a factor of 35.47. This factor is extremely large especially because it can only be attributed to the drag coefficient or the efficiency factor. Obviously, measurement errors and the assumptions made during the computation of the measured sediment transport could also have contributed to the large difference between observations and predictions (see van Maanen et al., 2009 for more details). Nevertheless, the calibrated predictions are shown in Figure A.4 and the associated root-mean-square deviation, ε_{rms}, using the testing dataset is equal to 0.66.

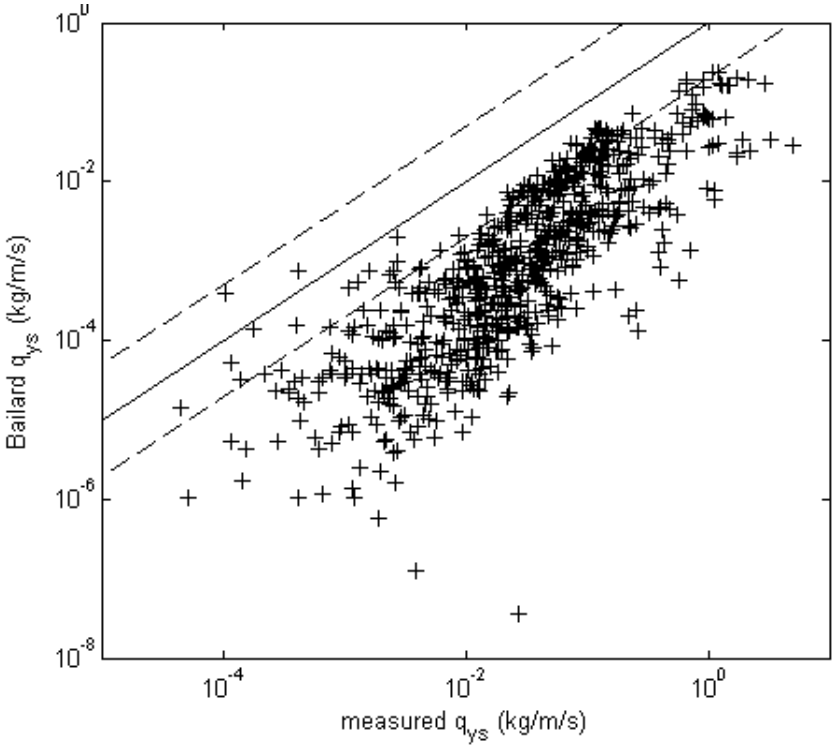

Figure A.3. Comparison of measured and predicted (using the Bailard formula) values of depth-integrated suspended sediment transport. The solid line indicates equality and the dashed lines indicate a factor 5 difference between the predicted and observed values.

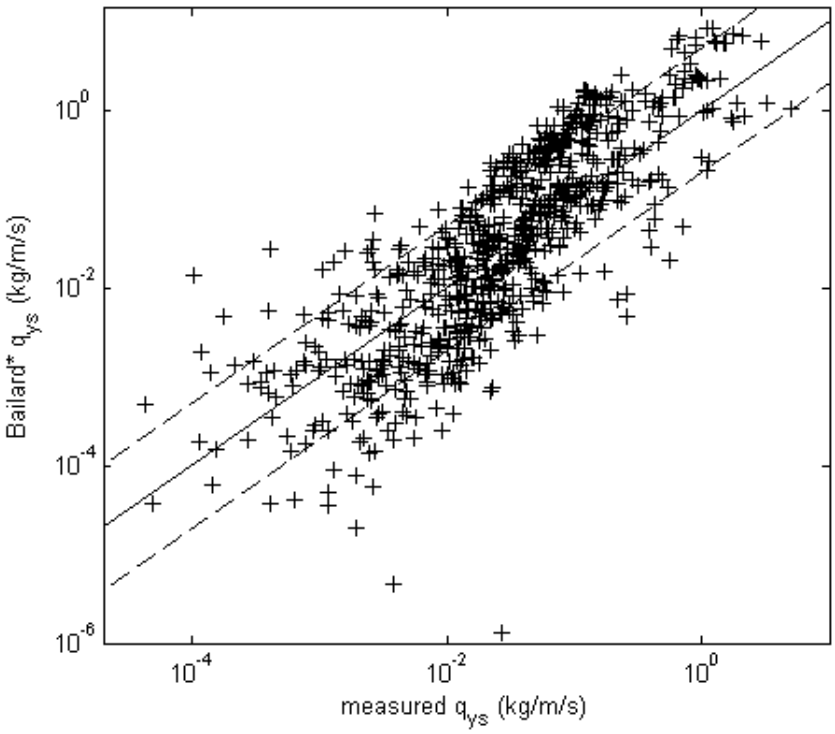

Figure A.4. Comparison of measured and predicted (using a calibrated version of the Bailard formula) values of depth-integrated suspended sediment transport. The solid line indicates equality and the dashed lines indicate a factor 5 difference between the predicted and observed values.

Figure A.5 shows typical ANN predictions when using the 4 available input variables (water depth, wave height and period, alongshore velocity) and 4 nodes in the hidden layer. There is a clear improvement (ε_{rms} has decreased to 0.43) compared to the calibrated Bailard predictions. Despite the improvement, the ANN struggles to predict the highest and lowest measured values. This problem is likely to arise from different effects. The low values of depth-integrated suspended sediment flux are so low that measurements might be close to the limits resulting from intrinsic instrument accuracy. In fact, although the performance of the Bailard model also decreases for low values of measured suspended sediment transport, the real problem might simply be the relatively small number of measurements available below 10^{-3} kg/m/s. Had the dataset included many more of these low measured values (with an instrument-accuracy problem), the ANN could have learnt about the instrument-accuracy problem and resulted in good (in the sense that they are close to the measured values) predictions. Overall, it is worth noticing that the low asymptotic limit for the

ANN (10^{-3}) is at least one order of magnitude higher than the lowest sediment flux measured and predicted according to Bailard (see Fig. A.4). The highest values are not particularly well-predicted by the ANN and we suspect this effect is again related to predicting the tails of the distribution of the available measurements. Only a small number of large values of suspended sediment flux are present in the overall dataset with no more than 53 values out of 2306 measurements that exceed 1 kg/m/s. This affects the training of the ANN and the ε_{rms} evaluated over these high values of measured sediment transport amounts to 0.51. This reflects a problem of ANNs (and data-driven models in general) which are difficult to train for extreme conditions while producing an accurate prediction of extreme values is of specific interest to coastal engineers and scientists. In general, similar predictive results have been obtained when changing the number of nodes in the hidden layer (changing the number of hidden nodes from 2 to 6 corresponded to changes in ε_{rms} from 0.49 to 0.51, the minimum value being 0.43 for 4 nodes).

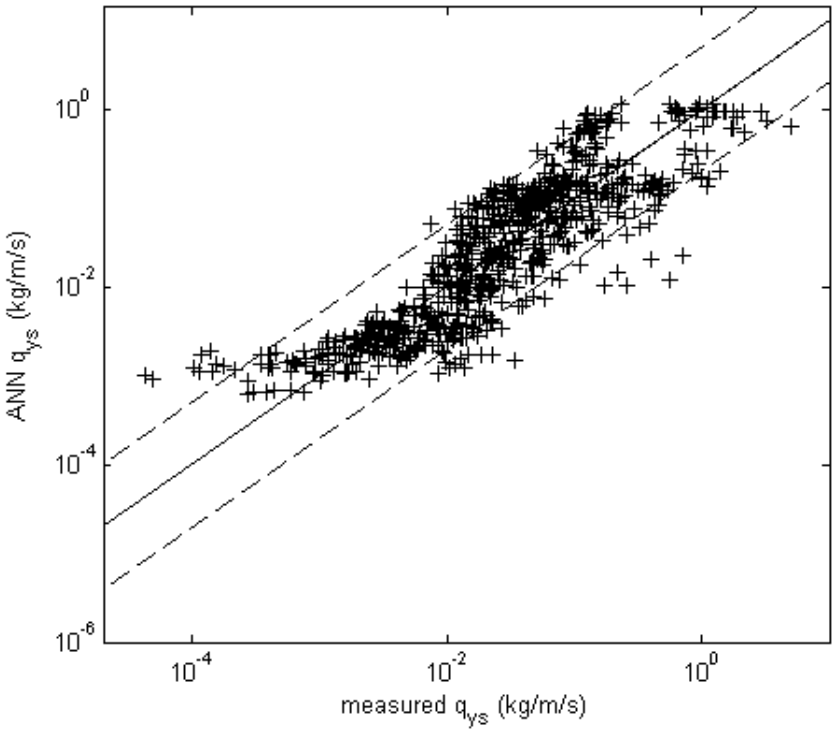

Figure A.5. Comparison of measured and predicted values of depth-integrated suspended sediment transport. Predictions have been made using an ANN with 4 inputs (*H*, *h*, *Tp*, *V*) and 4 nodes in 1 hidden layer. The solid line indicates equality and the dashed lines indicate a factor 5 difference between the predicted and observed values.

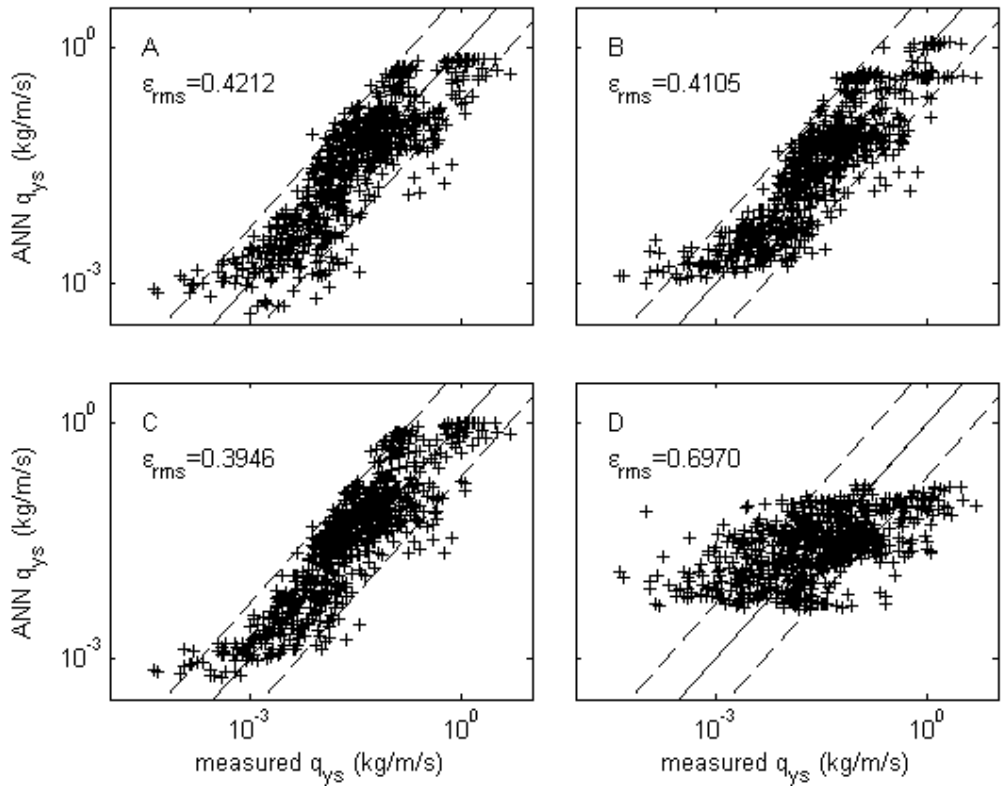

Figure A.6. Comparison of measured and predicted values of depth-integrated suspended sediment transport. Predictions have been made using an ANN with 3 inputs and 3 nodes in 1 hidden layer. Inputs are: A) h, H_{m0}, V; B) T_p, H_{m0}, V; C) T_p, h, V; D) h, H_{m0}, T_p. The solid line indicates equality and the dashed lines indicate a factor 5 difference between the predicted and observed values.

ANN results tend to be sensitive to correlations in the input variables. Some of the four variables are certainly characterized by some level of correlation. Correlation effects are likely to become particularly evident as a result of specific conditions encountered in the field (e.g. for saturated wave-breaking conditions, wave height and water depth become strongly correlated). To test the sensitivity to the choice of available input variables, we have built (following the same methodology described for the case with 4 input variables) ANNs characterized by only 3 inputs and 3 hidden nodes (Fig. A.6). When one variable between H_{m0}, h, and T_p is dropped out of the ANN, there is an improvement in the overall prediction skill of the ANN. Although results do not allow to distinguish which input variable (between H_{m0}, h, and T_p) is the most relevant, it is evident (see Fig. A.6d) that the alongshore component of the velocity plays a major role in the prediction of suspended sediment fluxes. Removing the alongshore component of the velocity

from the input variables causes a strong decay in the prediction power of the ANN. The lowest error (defined using Eq. A.4) was obtained using V, h and T_p as input variables. For the 3 best-performing models presented in Fig. A.6 we have analyzed the importance of individual variables and of their interactions using the PaD approach (see previous section). Analysis of the contribution of single variables (Table A.1) shows that, for all models considered, the alongshore component of the velocity is the input variable with the largest explanatory power. For each of the models presented in Table A.1 we have run 10,000 additional ANNs with different initial weights. We have then analyzed the weights of the ANNs with a predictive skill similar to the one of the best performing ANN (difference from the ε_{rms} shown in Fig. A.6 was below 10%) and, apart from negligible differences in the contribution of each variable, results confirm the findings reported in Table A.1. Analysis of the contribution of combinations of variables (Table A.2) is less straightforward but still provides evidence that, for all models, the mechanism(s) leading to improved predictions of depth-integrated sediment fluxes are related to the presence of an alongshore current and its interaction with the other variables. Probably because of cross-correlation between some of the input variables, other ANNs with similar predictive skill can result in contributions that differ from those presented in Table A.2. For example, with respect to Model 2 the explanatory power can shift between T_p-V and H_{m0}-V without any significant effect on the prediction skill.

Table A.1. Percentage of the contribution of single variables for the 3 best-performing models presented in Fig. A.6

	V	H_{m0}	h	T_p
Model 1: V-h-T_p	97.3		0.4	2.3
Model 2: V-H_{m0}-T_p	89.4	7.2		3.4
Model 3: V-H_{m0}-h	90.1	8.8	1.1	

Table A.2. Percentage of the contribution of combinations of variables for the 3 best-performing models presented in Fig. A.6

	h-T_p	h-V	T_p-V	H_{m0}-T_p	H_{m0}-V	h- H_{m0}
Model 1: V-h-T_p	0.4	13.3	86.3			
Model 2: V-H_{m0}-T_p			31.9	1.4	66.7	
Model 3: V-H_{m0}-h		18.5			80.2	1.3

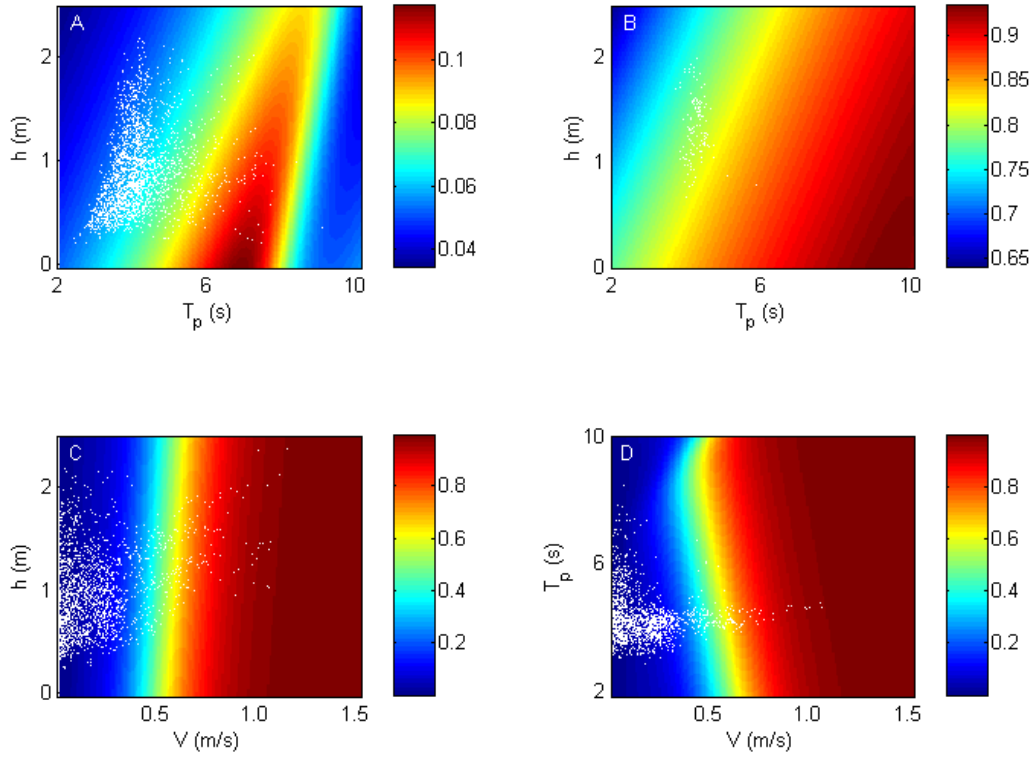

Figure A.7. Sensitivity of the best-performing ANN (Fig. A.6c. Input variables are V, h and T_p) to changes in the input variables. Colour-bar represents depth-integrated suspended sediment transport (kg/m/s). Notice the top subplots have a different colour-scale. In (A) and (B), V is equal to 0.17 (the mean value in the observations) and 0.7 m/s respectively. In (C) T_p is equal to 4.3 s (mean value) and in (D) h is 0.94 m (mean value). White dots represent observations whose value of the fixed variable is within ± 1 standard deviation from the fixed value.

A.4 Discussion and Conclusions

A typical criticism of an ANN predictor (or any other data-driven predictor) is that its validity is limited and intrinsically linked to the distribution of the input variables in the training dataset. To analyze this sensitivity and the "universality" of the ANN, we reconstructed the predictor using the biases and weights of the best performing ANN (Model 1 in Table A.1, see also Fig. A.6c) and then examined the response to changes in the input conditions. Figure A.7 shows that the response of the reconstructed ANN is extremely nonlinear and that extending the predictions far beyond the values considered in the training dataset can lead to unphysical results. For example, looking at Fig. A.7a where V is kept constant at 0.17 m/s (the observed mean value), it is easy to notice that an increase in depth-

integrated suspended sediment transport occurs for increasing values of T_p up to 6 seconds. The increase is smaller for larger depths. While these aspects of the predictor are physically sound, larger increases in T_p lead to a sharp decrease in sediment transport. This behaviour is clearly unphysical and, as shown by the white dots in Fig. A.7a, is driven by the extremely limited number of observations available for these combinations of V, h and T_p. It is also worth noticing that for these combinations of V, h and T_p only small values of sediment transport are observed (see colour-bar of Fig. A.7a and compare to the other subplots). If the fixed value of V is set to 0.7 m/s (Fig. A.7b), the response of the ANN to changes in h and T_p is physically sound as no reduction in sediment transport is predicted for large values of T_p. Figure A.7c and A.7d show a physically correct response of the ANN when respectively T_p and h are kept constant at their mean values (similar results are obtained for larger or smaller values of the fixed input variable). An increase in h corresponds to a small decrease in sediment transport (Fig. A.7c) and the opposite occurs for an increase in T_p (Fig. A.7d). The large gradient in sediment transport with respect to V indicates again the dominance of the alongshore velocity on ANN outcome.

A key requirement for any data-driven model, be it as simple as a linear regression or as complicated as an artificial neural network, is that it is capable of providing predictions that can explain the observed variability and that are physically meaningful. Because of the large number of free parameters, ANNs can create highly nonlinear functions which relate independent and dependent variables. This capability explains why ANNs can outperform both theoretical approaches (e.g. the Bailard model) and simple data-driven predictors (e.g. linear or multiple regressions). However, because of the complex structure of an ANN, it is difficult to disentangle the interactions between the input variables. As a result, despite their undeniable predictive power, ANNs have failed to provide insight with respect to the physical processes driving the predictions. In this contribution we use an already established technique to open up and lighten the ANN black box. This allows dissecting the interactions leading to predictions of sediment transport that are a large improvement (Fig. A.6) compared to a physically based predictor (Figs. A.3 and A.4). The use of the PaD technique allows ranking the role of each individual variable (Table A.1) and also of

combinations of variables (Table A.2). Physically, our results are not unexpected, in the sense that, because of cross-correlation effects, one variable between H_{m0}, T_p and h can be dropped without losing predictive skills. Also, as shown by the analysis of the relative importance of variables, the dominant input variable is the alongshore component of the velocity with a minor role played by resuspension mechanisms related to wave processes. The small contribution to the explanatory power of wave related input variables is likely to be related to the conditions encountered in the field during the collection of this dataset. A limitation of the present study is that it utilizes data collected at one beach site. For example, the ANN predictor does not include a grain size dependency which is clearly not physically correct. Moreover, the dataset used here encompasses only a small range of wave conditions. Adding datasets of measured sediment transport that cover a wide range of wave, sediment, and beach conditions during the development of the ANN and extensive validation could, ultimately, result in a more universal predictor.

Overall, the results presented in this paper suggest that using an ANN approach can result in the development of a powerful predictor and show that ANNs can be analyzed. However, users of ANNs should always bear in mind that when the input variables, or their combination, are different from the parameter space over which the ANN has been developed, predictions can be unphysical and so meaningless. On the other hand, the same ANN data-driven approach used in this study could be extended and applied to other datasets increasing the parameter space over which predictions are valid and so the generality of the predictor.

Acknowledgements

BvM and GC funded by the (New Zealand) Foundation for Research, Science and Technology (contracts CF102203 and WRHC102). BGR acknowledges funding by the Netherlands Organisation for Scientific Research (NWO) under contract 864.04.007.

References

Bailard, J.A.: An energetics total load sediment transport model for a plane sloping beach, J. Geophys. Res., 86, 10938-10954, 1981.

Bayram, A., Larson, M., Miller, H.C., and Kraus, N.C.: Cross-shore distribution of longshore sediment transport: comparison between predictive formulas and field measurements, Coast. Eng., 44, 79-99, 2001.

Benítez, J.M., Castro, J.L., and Requena, I.: Are artifical neural networks black boxes? IEEE Transactions on Neural Networks, 8, 1156-1164, 1997.

Browne, M., Castelle, B., Strauss, D., Tomlinson, R., Blumenstein, M., and Lane, C.: Near-shore swell estimation from a global wind-wave model: Spectral process, linear and artificial neural network models, Coast. Eng., 54, 445-460, 2007.

Burnham, K.P., and Anderson, D.R.: Model Selection and Multimodel Inference: A Practical Information-Theoretic Approach, Springer, New York, NY, 488 pp, 2002.

Dayhoff, J.E., and DeLeo, J.M.: Artificial neural networks: Opening the black box, Cancer, 91, 1615-1635, 2001.

Dimopoulos, I., Bourret, P., and Lek, S.: Use of some sensitivity criteria for choosing networks with good generalization ability, Neural Process. Lett., 2, 1-4, 1995.

Dimopoulos, I., Chronopoulos, J., Chronopoulos-Sereli, A., and Lek, S.: Neural network models to study relationships between lead concentration in grasses and permanent urban descriptors in Athens city (Greece), Ecol. Model., 120, 157-165, 1999.

Faraway, J., and Chatfield, C.: Time series forecasting with neural networks: a comparative study using the airline data, Applied Statistics, 47, 231-250, 1998.

Gardner, M.W., and Dorling, S.R.: Artificial neural networks (the multilayer perceptron) – a review of applications in the atmospheric sciences, Atmos. Environ., 32, 2627-2636, 1998.

Gevrey, M., Dimopoulos, I., and Lek, S.: Review and comparison of methods to study the contribution of variables in artificial neural network models, Ecol. Model., 160, 249-264, 2003.

Gevrey, M., Dimopoulos, I., and Lek, S.: Two-way interaction of input variables in the sensitivity analysis of neural network models, Ecol. Model., 195, 43-50, 2006.

Green, M.O., and Boon, J.D.: The measurement of constituent concentration in nonhomogeneous sediment suspensions using optical backscatter sensors, Mar. Geol., 110, 73-81, 1993.

Kingston, K.S., Ruessink, B.G., van Enckevort, I.M.J., and Davidson, M.A.: Artificial neural network correction of remotely sensed sandbar location, Mar. Geol., 169, 137-160, 2000.

Kolen, J.F., and Pollack, J.B.: Back propagation is sensitive to initial conditions, Complex Systems, 4, 269-280, 1990.

Krasnopolsky, V.M.: Neural network emulations for complex multidimensional geophysical mappings: Applications of neural network techniques to atmospheric and oceanic satellite retrievals and numerical modeling, Reviews of Geophysics, 45, RG3009, doi:10.1029/2006RG000200, 2007.

Lin, B., and Namin, M.M.: Modelling suspended sediment transport using an integrated numerical and ANNs model, J. Hydraul. Res., 43, 302-310, 2005.

McCann, D.W.: A neural network short-term forecast of significant thunderstorms, Forecasting Techniques, 7, 525-534, 1992.

Nagy, H.M., Watanabe, K., and Hirano, M.: Prediction of sediment load concentration in rivers using artificial neural network model, Journal of Hydraulic Engineering, 128, 588-595, 2002.

Olden, J.D.: An artificial neural network approach for studying phytoplankton succession, Hydrobiologia, 436, 131-143, 2000.

Olden, J.D., and Jackson, D.A.: Illuminating the "black box": a randomization approach for understanding contributions in artificial neural networks, Ecol. Model., 154, 135-150 2002.

Olden, J.D., Joy, M.K., and Death, R.G.: An accurate comparison of methods for quantifying variable importance in artificial neural networks using simulated data, Ecol. Model., 178, 389-397, 2004.

Pape, L., Ruessink, B.G., Wiering, M.A., and Turner, I.L.: Recurrent neural network modeling of nearshore sandbar behavior, Neural Networks, 20, 509-518, 2007.

Puleo, J.A., Johnson, R.V., Butt, T., Kooney, T.N., and Holland, K.T.: The effect of air bubbles on optical backscatter sensors, Mar. Geol., 230, 86-96, 2006.

Rumelhart, D.E., Hinton, G.E., and Williams, R.J.: Learning representations by back-propagating errors, Nature, 323, 533-536, 1986.

Sztobryn, M.: Forecast of storm surge by means of artificial neural network, J. Sea Res., 49, 317-322, 2003.

Tsai, C.P., and Lee, T.: Back-propagation neural network in tidal-level forecasting, Journal of Waterway, Port, Coastal and Ocean Engineering, 125, 195-202, 1999.

Tsai, C.P., Hsu, J.R.C., and Pan, K.L.: Prediction of storm-built beach profile parameters using neural networks, in Proceedings of the 27th International Conference on Coastal Engineering, ASCE, 3048-3061, 2000.

Van Maanen, B., de Ruiter, P.J., and Ruessink, B.G.: An evaluation of two alongshore transport equations with field measurements, Coast. Eng., 56, 313-319, 2009.

Van Rijn, L.C.: Sediment transport, part II: suspended load transport, Journal of Hydraulic Engineering, 110, 1613-1641, 1984.

Vaughn, M.L.: Interpretation and knowledge discovery from the multilayer perceptron network: opening the black box, Neural Comput. Appl., 4, 72-82, 1996.

Werbos, P.J.: Beyond regression: new tools for prediction and analysis in the behavioral sciences, [Ph.D. thesis], Cambridge, (MA): Harvard Univ., 1974.